STRUCTURAL, DYNAMICAL PROPERTIES OF POLYMERS AND POLYMER COMPOSITES FROM MULTISCALE SIMULATIONS

Thesis submitted to AcSIR For the award of
the Degree of
DOCTOR OF PHILOSOPHY
In Chemical Sciences

By

Souvik Chakraborty
Registration Number: 10CC12A26036

Under the guidance of

Dr. Sudip Roy
(Research Supervisor)

&

Dr. Suman Chakrabarty
(Research Co-Supervisor)

Physical Chemistry Division
CSIR-National Chemical Laboratory
Pune 411 008

February 2016

राष्ट्रीय रासायनिक प्रयोगशाला
(वैज्ञानिक तथा औद्योगिक अनुसंधान परिषद)
डॉ. होमी भाभा रोड, पुणे - 411 008. भारत
NATIONAL CHEMICAL LABORATORY
(Council of Scientific & Industrial Research)
Dr. Homi Bhabha Road, Pune - 411008. India

Certificate

This is to certify that the work incorporated in this Ph.D. thesis entitled **"*Structural, dynamical properties of polymers and polymer composites from multiscale simulations*"** submitted by **Souvik Chakraborty** to Academy of Scientific and Innovative Research (AcSIR) in fulfillment of the requirements for the award of the Degree of **Doctor of Philosophy In Chemical Sciences,** embodies original research work under my supervision. I further certify that this work has not been submitted to any other University or Institution in part or full for the award of any degree or diploma. Research material obtained from other sources has been duly acknowledged in the thesis. Any text, illustration, table etc., used in the thesis from other sources, have been duly cited and acknowledged.

Souvik Chakraborty

Souvik Chakraborty
(Student)

Dr. Sudip Roy
(Supervisor)

Dr. Suman Chakrabarty
(Co-supervisor)

Date: 01.02.2016

Place: Pune

Communications Channels ☎ +91 20 25902000 +91 20 25893300 +91 20 25893400 Fax +91 20 25902601 (Director) +91 20 25902660 (Admin.) +91 20 25902639 (Business Development) URL : www.ncl-india.org

DECLARATION

I hereby declare that the thesis entitled **"Structural, dynamical properties of polymers and polymer composites from multiscale simulations"** submitted for the degree of Doctor of Philosophy in Chemical Sciences to the Academy of Scientific & Innovative Research (AcSIR), has been carried out by me at the Physical Chemistry Division of CSIR-National Chemical Laboratory, Pune under the supervision of Dr. Sudip Roy and Dr. Suman Chakrabarty. Such material as has been obtained by other sources has been duly acknowledged in the thesis. The work is original and has not been submitted in part or full by me for any other degree or diploma to any other Institution or University.

Date: 01.02.2016
Place: CSIR-NCL, Pune

Souvik Chakraborty

Souvik Chakraborty
Ph. D candidate

"Science is a way of thinking much more than it is a body of knowledge"

Carl Sagan

(1934-1996)

Acknowledgements

The work presented in the thesis would not have been possible without the encouragement, and guidance of my thesis advisor Dr. Sudip Roy. I would like to thank him for providing me the opportunity and support me throughout the project. I thank my co-advisor Dr. Suman Chakrabarty for his helpful suggestions and insightful discussions. I am thankful to Dr. Rajnish Kumar for providing me fellowship for some time. In this *stumbled and fumbled* journey of mine, there were innumerable people, both within and outside of the institute, who have accompanied me, whom I owe so much because without them, the jouney could not have been accomplished. I express my heart-felt gratitude to all my labmates, my teachers, the members of my thesis advisory board, my collaborators, institute office staffs, NCL book & movie club members, my roommates, my friends and besiegers, and the last but not the least, my ever-supportive family. *muchas gracias.*

Souvik

Contents

List of Tables

Abstract

In this thesis we have carried out investigation of structural and dynamical properties of polymer nanocomposite systems by molecular dynamics (MD) simulations with multiscale (all atomistic and mesosale) approach. The aim is to explore and understand the structural, dynamical, and energetics at local level by atomistic simulation, and then, with mesoscale simulations, explore the large scale structures by long scale dynamics. The thesis is organized as follows:

CHAPTER 1: The aim is to explore explore structural, dynamical, thermodynamical properties of polymer composites by computer simulations. To obtain this, molecular dynamics simulations have been used in all atomistic study as well as in case of mesoscale simulations. The information gained from the all atomistic study is translated into the mesoscale simulations by applying necessary mapping procedure. Model systems are also considered to explore structure, dynamics of composites in a confining matrix. The properties are investigated in details in each case so that useful insights about the polymer composite systems can be obtained.

CHAPTER 2: This chapter presents the basic theoretical background. Brief description about the classical dynamics, force fields is discussed. For, free energy calculations, fundamentals of Umbrella Sampling technique have been discussed. For coarse-grain mesoscale simulations, theoretical aspects of Dissipative Particle Dynamics simulation are described.

CHAPTER 3: We report the structural and dynamical properties of polycarbonate-CNT composites obtained by performing all atomistic molecular dynamics simulations. The necessary force fields for CNT and polycarbonate have been calculated and validated. The detailed study of the interactions between CNT atoms and different polycarbonate moeties has been performed and discussed. The diffusivity of matrix has been studied at different temperatures. The dynamics of CNTs in the polycarbonate matrix is explored. The bundling of CNTs has been observed. The mechanism of bundling is elucidated.

CHAPTER 4: The energetics of the bundling of CNTs has been explored. The Umbrella Sampling simulation technique has been applied to study free energy calculations of the bundling process. Two types of CNT bundling approaches have been consodered: parallel and perpendicular and the respective free energy changes are computed in monomer and trimer of polycarbonate

matrices (both in monomer and trimer).

CHAPTER 5: Mesoscale simulation of polycarbonate-CNT composite is presented. Dissipative Particle Dynamics (DPD) has been performed to explore large scale morphology and dynamics of composite systems. The important target is to map the parameters required for DPD simulations from previously described all-atom simulations. So the Flory-Huggins theory is applied for necessary mapping procedure and interaction parameters for DPD simulation of polycarbonate-CNT composite have been calculated. The long range dynamics of bundles of CNTs is investigated by mean square displacement. The bundling size analysis is performed with different loadings of CNTs in polycarbonate.

CHAPTER 6: Dissipative particle dynamics simulations are performed on model systems of nanorod and diblock copolymer composite to understand the dynamics, structure, and morphology of self-assembled bundles of nanorods in gyroid phase. The nanorods are given preferential enthalpic interaction with minority component of diblock copolymer by increasing repulsion with majority component, so that nanorods tend to self-assemble and settle inside the confined contours of minority component aimimg to explore the relative size and shape of the self-assembled bundles under confining locations within the matrix. Also the structural details of bundles are explored as a function of nanorod flexibility.

List of Publications

1. Souvik Chakraborty, Sudip Roy. “Structural, Dynamical, and Thermodynamical Properties of Carbon Nanotube Polycarbonate Composites: A Molecular Dynamics Study”, The Journal of Physical Chemistry B 03/2012; 116(10):3083-91.

2. Souvik Chakraborty, Chandan Kumar Choudhury, Sudip Roy. “Morphology and Dynamics of Carbon Nanotube in Polycarbonate Carbon Nanotube Composite from Dissipative Particle Dynamics Simulation”, Macromolecules 04/2013; 46(9):3631.

3. Souvik Chakraborty, Sudip Roy. “Structure of Nanorod Assembly in The Gyroid Phase of Diblock Copolymer”, The Journal of Physical Chemistry B 05/2015; 119(22):6803-12

Chapter 1

General introduction and the scope of the thesis

The aim is to explore structural, dynamical, thermodynamical properties of polymer composites by computer simulations. To obtain this, molecular dynamics simulations have been used in all atomistic study as well as in case of mesoscale simulations. The information gained from the all atomistic study is translated into the mesoscale simulations by applying necessary mapping procedure. Model systems are also considered to explore structure, dynamics of composites in a confining matrix. The properties are investigated in details in each case so that useful insights about the polymer composite systems can be obtained.

1.1 Introduction

Computer simulations are beyond doubt emerged as one of the most important research tools in modern science. Powerful calculational capabalities of modern computers enable us to solve complex problems and obtain exact results. Simulations help us by providing the connection between the microscopic details of a model and the macroscopic properties of interest and the results can be comapared with experimental outcomes. So by conducting simulations computers can be used as *virtual laboratories*, where perfect control of the parameters is possible and accurate measurements can be achieved. Computer experiments are now widely applied to almost all fields of science and technology. Our group is involved in exploring and applying different simulation techniques to the various fields *e.g.* polymer composites[1, 2], biological membranes[3, 4], fuel cell membranes[5], gas hydrates[6] *etc.* We often adopt multiscale approach to address and explore different systems under study. The work presented here is a multiscale simulation study conducted on polymer composite systems to explore different properties. To do this, the necessary parameters have been developed to connect different scales. Once the parameters are derived we have applied the multiscale simulation technique for exploring macroscopic properties. The present thesis comprises of the investigations of the structural, dynamical, and thermodynamical properties of polymer composites by multiscale simulation approach aiming to connect all-atomistic and mesoscale levels of descriptions for such systems. Experimentally carbon nanotubes are well known for inducing enhanced mechanical strength and thermal conductivity in polymer when incorporated with small amount. Nanotube-polymer and nanotube-nanotube interactions in composite systems govern the macroscopic bulk properties like strength and stiffness, thermal and electrical conductivity etc. For this, the role of structure, dynamics and energetics of nanofillers in polymer matrix is very important. By all atomistic MD we can elucidate these molecular level interactions which can provide crucial insights about the system and that can be translated into helpful inputs for experiments. By mesoscale simulations we can explore structural, morphological properties like bundling of nanotubes in polymer matrix and that can be compared with experimental outcomes as mesoscale simulations can address larger length scale and longer timescale comparable to experiments. Thus multiscale approach is necessary to acquire proper insights about polymer composite

systems which can eventually help experimental polymer and materials science community to prepare more efficient polymer nanocomposites in future.

Multiscale simulation methods have become crucial in the field of science and engineering because we have to deal with a multitude of materials-related phenomena whose essential role encompasses over many scales in time and space. Multiscale simulation methods are widely used for soft matters such as polymers, bio-membranes, proteins etc. These materials are termed *soft* because their physical state is highly sensitive to very small fluctuations in interaction energies. The interaction in local level i.e. at small length scale often governs large scale conformations and morphologies. Local forces like van der Waals and hydrogen bonding, molecule-surface interactions, aromatic ring stacking etc. are often responsible for large scale structures and conformational changes. The multiscale simulation methods are broadly divided into two schools of thoughts: the continuum method and the particle based method. In continuum method atoms and molecules and their interactions are not directly taken into account. But the particle based methods consider all these interactions. Depending upon the system size and the time scale of the phenomena the particle based method comprises of hierarchy of methods. Ab-initio quantum chemical methods *e.g.* configuration interaction,[7] coupled cluster methods [8] can deal with few atoms (less than 100) and few picoseconds timescale only. These methods are accurate but computationally very expensive. Other quantum chemical methods like density functional theory,[9] semi-empirical methods *etc.* [10] consider larger systems. By integrating quantum chemical and classical simulations in a same simulation box QM MM (quantum chemical and molecular mechanics) or QM MD (quantum chemical and molecular dynamics) multiscale methods are also widely used. [11] However amorphous bulk systems with thousands of atoms can not be treated completely by quantum chemical methods because of the limitations in compuatational power. For such cases, classical molecular dynamics (MD) can be applied proficiently. In classical MD, the atoms are treated as particles interacting via classical potentials and the electrons are completely ignored. The classical potential is derived by performing quantum chemical calculations of much smaller constituent of the systems and adjusted according to the macroscopic bulk properties available from the experiments or other theoretical or simulation results. In case all atomistic MD, we consider atoms as individual particles. For coarse grained MD simulations, collection of atoms is treated as particle. Coarse grained

MD simulation can be performed for few millions of particles for the timescale of few microseconds. Multiscale simulation is vastly system dependent technique. Different multiscale simulation approaches have been developed and applied by different scientific groups. Muller-Plathe's group [12] and Kremer's group [13] used iterative Boltzmann inversion technique to coarse grain high molecular weight polymers to study equilibrium properties. MARTINI [14] coarse grained force field has been derived and implemented for biomolecules and nanoparticles interactions. Voth *et al.* [15] have used force matching multiscale method for different biomolecular phenomena like peptide aggregation, vesicle formation, self-assembly etc. Dissipative particle dynamics (DPD) developed by Hoogerbrugge and Koelman [16] is applied to simulate large polymeric systems to explore mesoscopic structures and dynamics, self-assembly of amphiphilic molecules, phases of block copolymers etc. In DPD, the necessary interaction parameters can be derived from all atomistic MD simulations for the system under study.[17] By applying Flory-Huggins theory of solubility the atomistic details can be mapped into mesoscopic phenomena. We have performed both all atomistic and DPD simulations for our work presented in the thesis and connected the two scales to explore properties. The DPD interaction parameters for nanotube polymer composite systems have been derived from our all atomistic MD simulations.

Polymers are soft materials having long chain with numerous repeating units linked together via covalent bonds. The mechanical strength and stiffness coupled with light-weight property, electrical conductivity, chemical durability make polymers the most desired material in substitution of metals nowadays. Great deal of studies is going on to prepare polymeric materials with even more desired properties to cope up with increasing demand for more effective material. Materials made of pristine polymers seem struggling to achieve the target to fulfill the ongoing demand. So polymer composite materials are gaining importance because of their enhanced and improved properties with respect to the pristine polymers. A small amount of filler can enhance the thermal, mechanical, electrical properties of polymer by manyfold. These fillers are in nanometer length scale with different dimensions and they include nanoparticles, nanotubes, nanorods, nanowires, clays with various chemical building blocks and different shapes. Carbon nanotube (CNT) is an important and widely used filler and when added to polymer by a small amount can improve the

mechanical, thermal, and electrical properties. Due to its anisotropic shape and high aspect ratio, it is used as a potential filler to form percolating network within polymer matrix and thus can enhance electrical, thermal conducting efficiency.

For the past few years carbon nanotube (CNT)-polymer composites have become an important field of study. Polycarbonates are widely used as plastic material. Polycarbonate is a versatile, transparent, and tough plastic material used for many applications in industry. It is a lightweight plastic material with quite admirable strength. This combination gives polycarbonate edge over other polymer materials in terms of applicability. It has been observed that incorporation of CNTs in the polymer matrix can significantly enhance mechanical (strength and stiffness), thermal and electrical properties of polymer and thus CNTs can be used as potential reinforcing agent [18–25]. CNTs in polymer matrix provide large interfacial area and the nature of interactions in this interface region plays crucial role in determining the improvements in mechanical and dynamical properties of nanocomposites.

This thesis addresses some of the important queries regarding polymer composite systems and tries to present insights on those aspects applying multiscale simulation tehnique. Investigation of local interactions between CNT and polymer is crucial to get insight of composite properties. So structure, dynamics of composite, local morphology of CNTs and their formation mechanism are studied with atomistic molecular dynamics (MD) simulations and discussed in the thesis. In experiments [26–32], it is quite common feature of CNTs to agglomerate due to strong cohesive force between CNTs. So study of energetics of bundle formation is important for understanding the bundling efficiency in polymer matrix with different chain lengths. Energetics of bundle formation of SWCNT in the monomeric and oligomeric polycarbonate matrix have been elucidated and discussed in the thesis. On the other hand, it is necessary to explore large scale morphology of nanotubes in polymer matrix also. So mesoscale simulation has been performed on polycarbonate CNT composite to explore large scale morphology and dynamics of nanotubes. The thesis also includes the mesoscale simulation study of Diblock copolymer nanorod composite systems. The detailed study of structural, dynamical properties of block copolymer composite system is also discussed in the thesis.

As nanotubes can enhance physical properties like strength, stiffness of polymer, a lot of experimental and theoretical studies have been pursued and still going on. The nature of structure and morphology attained by nanotubes dispersed in polymer matrix influence the enhancement of performance of polymer composites. The dispersion pattern of CNTs in the matrix, the interaction between polymer-CNT and CNT-CNT drive the extent of improvement of desired properties. At first, the aim was to look at the composite system at atomistic level so that a clear understanding of the local phenomena can be elucidated. So with atomistic MD simulations the effect of different loading of CNT in polycarbonate matrix of different chain lengths at different temperatures on structure and dynamics of polymer and CNT is investgated. The effect of loading on composite stiffness has been studied by investigating diffusivity of polymer. At higher loading bundling morphology is found to be formed by CNTs. During the process of aggregating, the mechanism local ordering of CNTs and different moeties of polycarbonate around CNT has been explored and discussed in the thesis.

After that this thesis addresses the investigation of energetics of bundle formation. For that, free energy of binding has been calculated using Umbrella Sampling simulations. Umbrella sampling simulations are used to calculate the free energy change (ΔG) associated with an event along a reaction coordinate, ξ [33–35]. This technique is usedin determine the binding energies and macromolecular interactions [36–45]. In umbrella sampling, a biasing potential is added to the Hamiltonian of the system to improve the sampling of the conformational space which are not sufficiently sampled. A series of configurations is generated along a reaction coordinate, ξ, between two interacting species one of which is considered as a reference and the other one is subjected to a biasing potential. The species under biasing potential takes up different positions with increasing centre of mass distance from the reference point. With the increasing centre of mass distances, few configurations are extracted which are called "sampling windows". Then for each window, independent simulation is performed to generate an ensemble of structures along the reaction coordinate. From each of this independent simulation, potential of mean force (PMF) is calculated and assembled over all the adjacent windows along the reaction coordinate by weighted histogram analysis method (WHAM) proposed by Kumar *et. al.* [46]. Gibb's free energy, ΔG is calculated from the PMF curve. By umbrella sampling, the binding energies of CNTs in polycarbonate

matrix have been investigated: one with parallel approach of CNT to form bundle, another is the perpendicular approach, and their respective energetics are compared.

Simulations have been used extensively to investigate the properties of polymers. Molecular dynamics (MD) and Monte Carlo (MC) methods are widely used techniques to study structure and dynamics of materials at atomistic level. But atomistic simulations are restricted in terms of length and time-scale [47–50]. Thus atomistic simulations of large polymer chains can not effectively sample the phase space for longer time and length-scale and thus, configurations often tend to confine at a local minimum energy. So observation of large scale change of morphology, phase transformations is difficult. Mesoscale simulation techniques can be used to overcome the length and time-scale restrictions and large number of particles can be simulated for much longer time to study equilibrium morphology and structural properties effectively [49]. Dissipative Particle Dynamics (DPD) has become quite popular recently as a mesoscopic simulation technique which has found large applications in various fields of materials. It has been used to study polymer-CNT composites [51–54], morphology of block co-polymers used in fuel cell [55], micelle formation [56–58], polymer viscosity [59], self-assembly of nanoparticles in polymer [60] etc. To apply DPD in polymer solutions and investigate the thermodynamics of mixing of different polymeric materials Groot and Warren [17] developed correlations between interaction potentials for DPD and Flory-Huggins theory of polymer solutions. Potschke et al.[61] investigated the electrical percolation network formation by multi-walled CNT in polycarbonate melt experimentally. The dispersability of CNTs under different melt processing conditions is studied by them. The agglomeration and network formation by nanotubes were observed and electrical percolation was studied by measuring conductivity using dielectric spectroscopy. They have reported that percolation threshold can be achieved in between 0.5 wt% and 5 wt% filler concentration for different kinds of multi-walled CNT. This experimental study of percolation of CNTs in polycarbonate propelled to investigate percolation network, dynamics and distribution of aggregates of CNTs in polycarbonate matrix theoretically and outcomes of the study are presented in the thesis. Necessary calculations to establish the relationship between Flory-Huggins parameter and repulsion parameter for CNT-polycarbonate composite system have been performed.

Diblock copolymer composites have attracted significant attention due to the potential applications in the field of material science and nanotechnogy.[60, 62–67] Diblock copolymer undergoes microphase separation below order-disorder transition temparature to form lamellar, gyroid, cylindrical, cubic phases depending on the composition and segregation strength between the components. The spatial distribution of nanoparticles and nanorods doped in diblock copolymer matrix can be directed by the microphase separation of block copolymers. Thus, microphase separation of diblock copolymer can be used advantageously to tailor the properties of composite.The doped matrials can be subjected to occupy specific locations of diblock copolymer matrix according to the specific aim to improve properties. The mechanical stability, electrical conductivity, and optical performance of composites are sensitive to the specific location of the 3-D organization of doped materials within the polymer matrix.[62, 68] The doped nanofillers, on the other hand, can influence and alter the morphology of microdomains of block copolymer.[64, 69–73] Most of the studies concerning the nanofillers doped in block copolymer phases discussed before deal with lamellar or cylindrical microdomains formed by the phase separation of block copolymers. Studies on the nanofillers incorporated in gyroid phase of block copolymer is relatively elusive. Recently, Li *et al.* have investigated the spatial arrangements of metal nanoparticles in the gyroid phase formed by triblock terpolymer matrix experimentally. According to them gyroid phase has potential to form next-generation mesoporous network superstructure. By doping gyroid domains with nanofiller, the effective potential applicability in the field of catalysis can be enhanced. [62] Thus, gyroid structure can be used as a *template* for many important applications. Gyroid phase has curved interfacial surface providing confinements throughout the matrix and thus, it can regulate the shape and sizes of self-assmebled nanofillers doped in it. Nanorods can also be of different flexibilities. The morphology of the bundles can be regulated by the relative bending tendency of the nanorods. So it is important to investigate and explore the morphology, structural and dynamical properties of nanorods in gyroid phase of block copolymer as function of different nanorod flexibilities and nanorod-diblock copolymer interactions.

The layout of the thesis is as follows.

In chapter 2, computational techniques are discussed.

In chapter 3, structure and dynamics of polycarbonate CNT composite are discussed.

In chapter 4, energetics of bundle formation by CNTs are presented.

In chapter 5, mesoscopic simulation of polycarbonate CNT composite is described.

In chapter 6, structure and dynamics of nanorods in gyroid phase of diblock copolymer are discussed.

In chapter 7, conclusions from the above studies are presented.

References

[1] Chakraborty, S.; Roy, S. *J. Phys. Chem. B* **2012**, *116*, 3083–3091.

[2] Chakraborty, S.; Choudhury, C. K.; Roy, S. *Macromolecules* **2013**, *46*, 3631–3638.

[3] Choudhury, C. K.; Kumar, A.; Roy, S. *Biomacromolecules* **2013**, *14*, 3759–3768.

[4] Pandey, P. R.; Roy, S. *J. Phys. Chem. B* **2011**, *115*, 3155–3163.

[5] Pahari, S.; Choudhury, S. K.; Pandey, P. R.; More, M.; Arun, V.; Roy, S. *J. Phys. Chem. B* **2012**, *116*, 7357–7366.

[6] Baghel, V. S.; Kumar, R.; Roy, S. *J. Phys. Chem. C* **2013**, *117*, 12172–12182.

[7] Langhoff, S. R.; Davidson, E. R. *Int. J. Quant. Chem.* **1974**, *8*.

[8] Bartlett, R. J. *Ann. Rev. Phys. Chem.* **1981**, *32*.

[9] Kohn, W.; Becke, A. D.; Parr, R. G. *J. Phys. Chem.* **1996**, *100*.

[10] Stewart, J. J. P. *J. Comput. Chem.* **1989**, *10*.

[11] Murphy, R. B.; Philipp, D. M.; Friesner, R. A. *J. Comput. Chem.* **2000**, *21*.

[12] Karimi-Varzaneh, H. A.; Carbone, P.; Muller-Plathe, F. *J. Chem. Phys.* **2008**,

[13] Abrams, C. F.; Delle Site, L.; Kremer, K. *Phys. Rev. E* **2003**,

[14] Marrink, S. J.; Risselada, H. J.; Yefimov, S.; Tieleman, D. P.; de Vries, A. H. *J. Phys. Chem. B* **2007**, *111*.

[15] Izvekov, S.; Parrinello, M.; Burnham, C. J.; Voth, G. A. *J. Chem. Phys.* **2004**, *120*.

[16] Hoogerbrugge, P. J.; Koelman, J. M. V. A. *Europhys. Lett.* **1992**, *19*, 155.

[17] Groot, R. D.; Warren, P. B. *J. Chem. Phys.* **1997**, *107*, 4423–4435.

[18] Potschke, P.; Fornes, T. D.; Paul, D. R. *Polymer* **2002**, *43*, 3247–3255.

[19] Starr, F. W.; Knauert, S. T.; Douglas, J. F. *J. Polym. Sci. Part B: Polym. Phys.* **2007**, *45*, 1882–1897.

[20] Lozano, K.; Bonilla-Rios, J.; Barrera, E. V. *J. Appl. Polym. Sci.* **2001**, *80*, 1162–1172.

[21] Lozano, K.; Barrera, E. V. *J. Appl. Polym. Sci.* **2001**, *79*, 125–133.

[22] Subramoney, S. *Adv. Mater.* **1998**, *10*, 1157–1171.

[23] Dickey, E. C.; Qian, D. *Appl. Phys. Lett.* **2000**, *76*, 2868–2870.

[24] Coleman, J. N.; Gun'ko, Y. K.; Khan, U. *Adv. Mater.* **2006**, *18*, 689–706.

[25] Coleman, J. N.; Cadek, M.; Blake, R.; Nicolosi, V.; Ryan, K. P.; Belton, C.; Fonseca, A.; Nagy, J. B.; Gun'ko, Y. K.; Blau, W. J. *Adv. Funct. Mater.* **2004**, *14*, 791–798.

[26] Potschke, P.; Kasaliwal, G. R.; Pegel, S.; Goldel, A.; Heinrich, G. *Polymer* **2010**, *51*, 2708–2720.

[27] Potschke, P.; Pegel, S.; Petzold, G.; Alig, I.; Dudkin, S. M.; Lellinger, D. *Polymer* **2008**, *49*, 974–984.

[28] Micusik, M.; Omastova, M.; Krupa, I.; Prokes, J.; Pissis, P.; Logakis, E.; Pandis, C.; Potschke, P.; Pionteck, P. *J. Appl. Polym. Sci.* **2009**, *113*, 2536–2551.

[29] Du, F. M.; Scogna, R. C.; Zhou, W.; Brand, S.; Fischer, J. E.; Winey, K. I. *Macromolecules* **2004**, *37*, 9048–9055.

[30] Masuda, J.; Torkelson, J. M. *Macromolecules* **2008**, *41*, 5974–5977.

[31] Baets, J.; Godara, A.; Devaux, J.; Verpoest, I. *Compos Part A-Appl s* **2008**, *39*, 1756–1761.

[32] Potschke, P.; Kasaliwal, G. R.; Goldel, A. *J. Appl. Polym. Sci.* **2009**, *112*, 3494–3509.

[33] Patey, G. N.; Valleau, J. P. *Chem. Phys. Lett.* **1973**, *21*, 297.

[34] Torrie, G. M.; Valleau, J. P. *Chem. Phys. Lett.* **1974**, *28*, 578.

[35] Torrie, G. M.; Valleau, J. P. *J. Comput. Phys.* **1977**, *23*, 187.

[36] Karplus, M.; Bartels, C. *J. Phys. Chem. B* **1998**, *102*, 865–880.

[37] Bevan, D. R.; Lemkul, J. A. *J. Phys. Chem. B* **2010**, *114*, 1652–1660.

[38] Halperin, A.; Ermilov, V.; Lazutin, A. *Macromolecules* **2010**, *43*, 3511–3520.

[39] Gunsteren, W. F.; Beutler, T. C.; Bremi, T.; Ernst, R. R. *J. Phys. Chem.* **1996**, *100*, 2637–2645.

[40] Novak, B. R.; Moldovan, D.; Waldrop, G. L.; de Queiroz, M. S. *J. Phys. Chem. B* **2009**, *113*, 10097–10103.

[41] Maragakis, P.; van der Vaart, A.; Karplus, M. *J. Phys. Chem. B* **2009**, *113*, 4664–4673.

[42] Wolf, M. G.; Jongejan, J. A.; Laman, J. D.; de Leeuw, S. W. *J. Phys. Chem. B* **2008**, *112*, 13493–13498.

[43] Procacci, P.; Marsili, S.; Barducci, A.; Chelli, R.; Schettino, V. *J. Phys. Chem. B* **2006**, *110*, 14011–14013.

[44] Topf, M.; Richards, W. G. *J. Am. Chem. Soc.* **2004**, *126*, 14631–14641.

[45] Brady, J. W.; Schmidt, R. K.; Teo, B. *J. Phys. Chem.* **1995**, *99*, 11339–11343.

[46] Rosenberg, J. M.; Kumar, S.; Bouzida, D.; Swendsen, R. H.; Kollman, P. A. *J. Comput. Chem.* **1992**, *13*, 1011–1021.

[47] Frenkel, D.; Smit, B. *Understanding Molecular Simulation*, 2nd ed.; Academic Press, Inc.: Orlando, FL, USA, 2001.

[48] Allen, M. P.; Tildesley, D. J. *Computer simulation of liquids*; Clarendon Press: New York, NY, USA, 1987.

[49] Müller-Plathe, F. *ChemPhysChem* **2002**, *3*, 754–769.

[50] Nieminen, R. M. *J. Phys.: Condens. Matter.* **2002**, *14*, 2859.

[51] Maiti, A.; Wescott, J.; Kung, P. *Mol. Simulat.* **2005**, *31*, 143–149.

[52] Maiti, A.; Wescott, J.; Goldbeck-Wood, G. *Int. J. Nanotechnology* **2005**, *2*, 198–214.

[53] Wang, Y.-C.; Ju, S.-P.; Cheng, H.-Z.; Lu, J.-M.; Wang, H.-H. *J. Phys. Chem. C* **2010**, *114*, 3376–3384.

[54] Wang, Y.-C.; Ju, S.-P.; Huang, T. J.; Wang, H.-H. *Nanoscale Res. Lett.* **2011**, *6*, 433.

[55] Roy, S.; Markova, D.; Kumar, A.; Klapper, M.; Müller-Plathe, F. *Macromolecules* **2009**, *42*, 841–848.

[56] Cui, Y.; Zhong, C.; Xia, J. *Macromol. Rapid Comm.* **2006**, *27*, 1437–1441.

[57] Fraser, B.; Denniston, C.; Müser, M. H. *J. Chem. Phys.* **2006**, *124*, 104902.

[58] Li, X.; Deng, M.; Liu, Y.; Liang, H. *J. Phys. Chem. B* **2008**, *112*, 14762–14765.

[59] Fedosov, D. A.; Karniadakis, G. E.; Caswell, B. *J. Chem. Phys.* **2010**, *132*, 144103.

[60] Liu, D.; Zhong, C. *Macromol. Rapid Comm.* **2006**, *27*, 458–462.

[61] Pegel, S.; Potschke, P.; Petzold, G.; Alig, I.; Dudkin, S. M.; Lellinger, D. *Polymer* **2008**, *49*, 974 – 984.

[62] Li, Z.; Hur, K.; Sai, H.; Higuchi, T.; Takahara, A.; Jinnai, H.; Gruner, S. M.; Wiesner, U. *Nat. Commun.* **2014**, *5*, 1–10.

[63] He, L.; Pan, Z.; Zhang, L.; Liang, H. *Soft Matter* **2011**, *7*, 1147–1160.

[64] Balazs, A. C.; Emrick, T.; Russell, T. P. *Science* **2006**, *314*, 1107.

[65] Peng, G.; Qiu, F.; Ginzburg, V. V.; Jasnow, D.; Balazs, A. C. *Science* **2000**, *288*, 1802.

[66] Lopes, W. A.; Jaeger, H. M. *Nature* **2001**, *414*, 735.

[67] Leibler, L. *Macromolecules* **1980**, *13*, 1602.

[68] Bockstaller, M. R.; Thomas, E. L. *Phys. Rev. Lett.* **2004**, *93*, 166106–1.

[69] Lee, J. Y.; Thompson, R.; Jasnow, D.; Balazs, A. C. *Macromolecules* **2002**, *35*, 4855.

[70] Kim, B. J.; Chiu, J. J.; Yi, G. R.; Pine, D. J.; Kramer, E. J. *Adv. Mater.* **2005**, *17*, 2618.

[71] Jin, J. Z.; Wu, J. Z.; Frischknecht, A. L. *Macromolecules* **2009**, *42*, 7537–7544.

[72] Sun, Y. S.; Jeng, U. S.; Liang, K. S.; Yeh, S. W.; Wei, K. H. *Polym.* **2006**, *47*, 1101.

[73] Yeh, S. W.; Wei, K. H.; Sun, Y. S.; Jeng, U. S.; Liang, K. S. *Macromolecules* **2005**, *38*, 6559.

Chapter 2

Computational methods

This chapter presents the basic theoretical background. Brief description about the classical dynamics, force fields is discussed. For, free energy calculations, fundamentals of Umbrella Sampling technique have been discussed. For coarse-grain mesoscale simulations, theoretical aspects of Dissipative Particle Dynamics simulation are described.

2.1 Introduction

Computer simulations serve as bridge between theory and experiment. With the help of powerful calculation capabilities of the computer, we can obtain solutions of complex problems with exact results. These results can be compared with experimental measurements. In this way, the comparison of theory and experiment becomes more conclusive. Another important aspect of simulation is that it is a machinery that provides the connection between the microscopic details of a model and the macroscopic properties of interest. Sometimes experiments can become very difficult to perform under extreme conditions like high temperature and high pressure. Then computer simulation can be performed with perfect control over all parameters and accurate measurements can be obtained. Thus, computer can act as a virtual laboratory. In addition to that, computer simulations provide us to explore how microscopic structure is related to bulk properties. By switching on and off the different features of the model and studying the resulting effects separately one can identify the contributing factors that are responsible for the outcomes of collective phenomena. In atomistic scale simulations, complex chemical structures are modelled at the level of individual atoms. The aim is to understand macroscopic properties from the detail knowledge of atomistic level descriptions. But for complex systems like polymers atomistic simulations are computationally expensive. So coarse-grain simulations are performed where unessential atomistic level details are ignored. To study large scale structures one needs to adopt large system size (e.g. polymers are long chain molecules) and long simulation time. Coarse-grained method can be effectively applied to these kind of systems because as the degrees of freedoms of group of atoms are frozen and considered as a bead, it allows much longer time-scale sampling of very large structures and the resulting morphologies can be compared with experimental findings.

In the present thesis, both atomistic and coarse-grain simulation have been performed to study polymer composite systems. For atomistic simulations, all atom classical Molecular Dynamics (MD) method has been adopted. Umbrella Sampling simulations have been performed to explore free energy calculations regarding bundling phenomena of carbon nanotubes in polymer matrices. Then Dissipative Particle Dynamics (DPD) simulations have been adopted as coarse-grain method to explore large scale morphologies of polymer composites. These methods are discussed here.

2.2 Classical Molecular Dynamics

In the present study, all atomistic classical molecular dynamics simulation has been employed in order to achieve the desired microscopic/macroscopic properties of the systems. The term *classical* refers to the use of Newtonian mechanics to define the physical basis of the model. The Newton's equation of motion for N interacting particles is given as below,

$$m_i \frac{\partial^2 r_i}{\partial t^2} = F_i, i = 1..N \tag{2.1}$$

where m_i and r_i represents the mass and the position of a particle and t is the time. The force (F_i) exerted on the particle is expressed as a negative gradient of potential energy from all the interacting particles in the system.

$$F_i = -\frac{\partial V(r_1, r_2, ..., r_N)}{\partial r_i} \tag{2.2}$$

The potential energy (V) between the particles is defined as a function of their positions r_i. m_i is the mass of particle *i*. Force (F_i) on particle *i* is calculated as the negative gradient of the potential energy *V* due to all other particles present in the system. For each timestep of the MD simulation, these equations are solved and the particles are propagated in an appropriate ensemble coupled with thermostats and barostats. MD simulation generates a series of configurations with position and velocity of each particle written to an output file which is referred as trajectory. The trajectory can be used to visualize the evolution of the system as a function of simulation time, calculating the properties to compare with the experiments and also to compute the numbers which are not available experimentally.

MD simulation comprises of three essential inputs such as coordinates, forcefield and simulation parameters. The coordinates are the set of the numbers to determine the position of every atom in a space which are derived from the experimental techniques such as X-ray crystallography or NMR etc. These serve as a starting structures for the simulation. These starting structures are subjected to energy minimization to bring them to the minima at the potential energy surface otherwise the simulation may fail. The initial structure, after solvation, might acquire inappropriate geometry or steric clashes. Therefore it needs to be removed first to relax the structure. Steepest descent and conjugate gradient are the commonly used algorithms for energy minimization.

The *force fields* are the set of paramaters and the potential energy functions that defines the inter-atomic potentials. The parameter sets are empirical and consist of various information about the chemical model such as different types of atoms, chemical bonds, dihedral angles and so on. The force field defines connectivity between the atoms in molecule depending upon the inter-atomic potentials. The inter-atomic potentials are of two types, bonded potentials and non-bonded potentials. Further, the bonded interactions are divided into bond length, bond angle and dihedral angle while non-bonded potentials are taken care by Lennard Jones and Coulomb interactions. The energy functions in MD simulation are expressed as,

$$\begin{aligned} V &= V_{bonded} + V_{nonbonded} \\ V_{bonded} &= \sum_{bonds} \frac{1}{2} K_b (b - b_0)^2 + \sum_{angles} \frac{1}{2} K_\theta (\theta - \theta_0)^2 + \sum_{dihedrals} K_\phi (1 + cos(n\phi - \lambda)) \\ V_{nonbonded} &= \sum_{LJ} 4\epsilon_{ij} \left[\left(\frac{\sigma_{ij}}{r_{ij}} \right)^{12} - \left(\frac{\sigma_{ij}}{r_{ij}} \right)^{6} \right] + \sum_{coulomb} \frac{q_i q_j}{4\pi\epsilon_o r_{ij}} \end{aligned} \tag{2.3}$$

The bonds and angles are commonly treated with the harmonic (Hookean) potentials, however cosine periodic functions are used in case of the dihedral angles. K_b, K_θ and K_ϕ represents the bond, angle and dihedral angle force constants and values b, θ and ϕ are the values at time *t* deviating from equilibrium values b_0, θ_0 and ϕ_0. The dihedral potential function is defined with multiplicity n and phase λ. However, improper dihedrals are used to maintain the coplanarity of the atoms in planar molecules (*e.g.* aromatic rings) or sometimes it is used to avoid the flipping at the chiral centers in a molecule. The nonbonded interactions consist of three terms which include a repulsion, dispersion and a Coulomb term. The repulsion $(-\frac{1}{r^{12}})$ and dispersion $(-\frac{1}{r^6})$ between particle i and j can be taken care with Lennard-Jones potential. The ϵ_{ij} signifies negative well depth and a steep repulsive wall at a distance r $< \sigma_{ij}$. However, charged contributions are computed from the Coulombic term where q_i and q_j are the charges on the corresponding particle separated by distance r_{ij}. Bonded interactions consist of values of bond, angle and dihedral constants, and the corresponding equilibrium values. These parameters are available in a force field, and hence are input to MD simulation. Similarly, for nonbonded interactions such as σ_{ij}, ϵ_{ij}, and partial charges for all the particles are provided as input to MD simulations. All the parameters available in a force field (also called force field parameters), are calculated empirically. The tedious process of force field development involves calculation of these empirical force field parameters. Commonly used

force fields are OPLS [1, 2], AMBER [3], CHARMM [4], and GROMOS [5]. They include force field parameters for different class of complex chemical moieties.

Along with starting structure and force field, a set of instructions or parameters is needed to run the simulation. The MD simulation algorithm involves successive calculation of force at each time-step followed numerically solving Newtons equations of motion. However, for the initiation of the MD simulation position and the velocities are always needed. The initial velocities for every atom are generated from Maxwell-Boltzmann velocity distribution by following equation,

$$p(v_i) = \sqrt{\frac{m_i}{2\pi kT}} exp\bigg(- \frac{m_i v_i^2}{2kT} \bigg) \tag{2.4}$$

where *k* is the Boltzmanns constant. It computes a distribution of velocities generated from random numbers. However, all velocities, thus generated, are scaled so that the total energy corresponds exactly to temperature *T*.

In MD simulation, the forces are used to integrate Newtons equations of motion, and hence propagate the particles in the system. Among many integration algorithms available *leap-frog* algorithm [6] is commonly used. It updates the positions and velocities using the forces at time t according to the following relations

$$\begin{aligned} v(t + \frac{1}{2}\Delta t) &= v(t - \frac{1}{2}\Delta t) + \frac{\Delta t}{m} F(t) \\ r(t + \Delta t) &= rt + \delta t v(t + \frac{1}{2}\Delta t) \\ r(t + \Delta t) &= 2rt - r(t - \Delta t) + \frac{1}{m} F(t)\Delta^2 + O(\Delta t^4) \end{aligned} \tag{2.5}$$

The Δt is the timestep chosen to integrate the Newton's equation of motion. Timestep is generally used as 1 fs, while in some cases, 2 fs is also used to enhance the performance in simulation time by keeping bond vibration constant. Such bond constraints are incorporated in MD simulation using LINCS[7] or SHAKE[8] algorithms.

Calculation of the nonbonded terms is the most time-consuming part of MD simulation. It is pair additive. Hence, in principle, the energy between every pair of atoms is computed so that the number of steps increases as the square of the number of atoms (N^2). Therefore, to speed up the computation, a cut-off radius is defined separately for LJ and Coulombs interactions and the calculation of the non-bonded energies beyond this distance cut-off are ignored. The LJ interactions

are truncated using a shift and switch function which sets the interaction potentials to zero after the cut-off distance. The long range electrostatic interactions are important in terms biomolecular process hence, they must be modeled accurately. However, as we use larger cut-offs to treat a long range Coulombic interactions, the computational cost will dramatically increase. Therefore, such interactions are treated with the reaction field, Ewald sum, or particle mesh Ewald method. In reaction-field, the electrostatics are taken care with a uniform dielectric constant beyond the short-range cutoff value. Ewald sum [6, 9] method computes the long-range interactions in an infinitely periodic systems and summation of interaction energies (long range) is done in Fourier space.The periodicity is taken care of by the periodic boundary conditions. In PME[6], direct summation method of the Ewald summation method is replaced by summation over point particles (particle part of PME). Ewald summation takes advantage and reduces the complexity and scales up to $N^{\frac{3}{2}}$, though impractical while dealing with larger biological systems. PME is a faster algorithm that uses fast Fourier transform to bring down the complexity to NlogN and thus substantially reduces the computational time needed. However, the speed and accuracy depends on the mesh size, interpolation scheme etc. The thermodynamic ensembles are essential in order to obtain the desired properties out of the system. Microcanonical (NVE) ensemble can be used if the total number of atoms N and the volume V(of the unit cell) are kept constant along with the energy (E). However, one can chose the canonical ensemble to maintain the number of atoms (N), volume (V) and temperatute (T) of the system constant. The temperatute of the system is kept constant by coupling of the system with the thermostat. Most commonly used thermostats are V-rescale[6], Berendsen[10] and Nose-Hoover[11]. Isothermal-Isobaric (NPT) ensemble is used to maintain the constant pressure in the system. Berendsen[10] and Parrinello-Rahman[6, 9] barostat are used to maintain the system pressure constant. With these inputs molecular dynamics algorithm integration of the equations of motion for each timestep (given as input) for a desired simulation time (calculated as $\Delta\times$ number of steps) then yields a trajectory that describes the positions, velocities and accelerations of the particles as they vary with time. In the present thesis, all atomistic simulations are performed using GROMACS simulation suit [12, 13]. Analyses were done by using self-written codes as well as GROMACS tools. For elucidating bundling mechanism of nanotubes and their orientation in matrix we have used our own codes. Details of those analyses are provided in corresponding

places in the different chapters.

2.3 Free Energy Calculation

One of the important aspects of molecular dynamics (MD) simulation is that it provides to explore the macroscopic properties of a system through microscopic simulations such as calculation of solvation free energy, binding free energy of a particular drug, or to examine the energetics and mechanisms of conformational change. There are several free energy calculation methods based on MD simulation are available, such as MM-PBSA[14], thermodynamic integration[15], free energy perturbation[16] and umbrella sampling[9, 17] which can calculate the free energy of the system.

The umbrella sampling, a biased MD simulation, is the one of the efficiently used techniques to calculate the free energy of the system evolving from one thermodynamic state to another (e.g. reactant and product) as a function of the reaction coordinate. This method involves simulation of systems with a biasing umbrella potential to reach the conformational phase space which is, otherwise, not possible with the conventional MD simulation.

For polymer composite systems, to determine energetics of bundling of nanotubes embedded in polymer matrix, the energy landscape is expected to have multiple barriers. For such complex energy landscape effective bias potential is necessary to be applied. Furthermore, the phase space sampling of the reaction coordinate i.e. the binding pathway has to be efficient so that correct energetics can be elucidated which can be compared with the experiments. As umbrella sampling technique considers multiple configurations (windows) along the binding pathway, the effective sampling can be achieved by performing sampling simulations on individual windows which, once combined, can provide more realistic energy surface having multiple barriers. The method uses MD simulation to determine the probability for the system under study to be in a given conformation. Then the energy landscape is determined by inverting Boltzmann distribution. In this method, the sampling windows along the reaction coordinate are generated and simulated independently. The sampled distribution of the system along the reaction coordinate are used to calculate the free energy change in each window and then combined together to generate the continuous smooth

energy profile. In the present thesis, umbrella sampling is employed to investigate the bundling energetics of CNTs in Polycarbonate matrix.

The bias potential w_i of window *i* is an additional energy term, which depends only on the reaction coordinate.

$$E^b(r) = E^u(r) + w_i(\xi) \tag{2.6}$$

The term E^b, $E^u(r)$ and $w_i(\xi)$ are the biased, unbiased energy functions and umbrella potential added to the system respectively. The free energy is related to the probability distribution of the system along given reaction coordinate . In umbrella sampling, the distribution of the system along given reaction coordinate is calculated with probability distribution function. Assuming the ergodic system, the probability distribution of biased system along a reaction coordinate P_i^b can be computed as,

$$P_i^b(\xi) = \frac{\int exp[-\beta[E(r) + w_i(\xi'(r))]]\delta[\xi'(r) - \xi]d^N r}{\int exp[-\beta E(r) + w_i(\xi'(r))]d^N r} \tag{2.7}$$

The unbiased free energy $A_i(\xi)$ can be obtained from the unbiased distribution,

$$P_i^u(\xi) = \frac{\int exp[-\beta E(r)]\delta[\xi'(r) - \xi]d^N r}{\int exp[-\beta E(r)]d^N r} \tag{2.8}$$

As the bias potential depends only on ξ and the integration in the numerator is performed over all degrees of freedom but ξ,

$$P_i^b(\xi) = exp[-\beta w_i(\xi)] \times \frac{\int exp[-\beta E(r)]\delta[\xi'(r) - \xi]d^N r}{\int exp[-\beta[E(r) + w_i(\xi'(r))]]d^N r} \tag{2.9}$$

$$\begin{aligned} P_i^u(\xi) &= P_i^b(\xi)\ exp[\beta w_i(\xi)] \times \frac{\int exp[-\beta[E(r) + w_i(\xi(r))]]d^N r}{\int exp[-\beta E(r)]d^N r} \\ &= P_i^b(\xi)\ exp[\beta w_i(\xi)] \times \frac{\int exp[-\beta[E(r)] exp[-\beta w_i[\xi(\overrightarrow{r})]]d^N r}{\int exp[-\beta E(r)]d^N r} \\ &= P_i^b(\xi)\ exp[\beta w_i(\xi)]\ \langle exp[-\beta w_i(\xi)]\rangle \end{aligned} \tag{2.10}$$

Using Eq. (2.10), $A_i(\xi)$ can be evaluated. As $P_i^b(\xi)$ is obtained from an MD simulation of the biased system, $w_i(\xi)$ is given analytically, and F_i =$-\frac{1}{\beta} ln\langle exp[-\beta w_i(\xi)]\rangle$ is independent of ξ which is a constant,

$$A_i(\xi) = -(\frac{1}{\beta}) \ln P_i^b(\xi) - w_i(\xi) + F_i \tag{2.11}$$

Therefore, by this way, the free energy $A_i(\xi)$ for every sampling window is calculated. However,the free-energy curves $A_i(\xi)$ of more windows are needed to be combined together to get one

global $A(\xi)$. Therefore, the F_i are to be calculated as they are associated with the bias potential and connect the free-energy curves $A_i(\xi)$ obtained in the different windows: The F_i can be calculated as,

$$\begin{aligned} exp(-\beta F_i) &= \langle exp(-\beta w_i(\xi)) \rangle \\ &= \int P^u exp[-\beta w_i(\xi)] d\xi \\ &= \int exp[-\beta[A(\xi) + w_i(\xi)]] d\xi \end{aligned} \tag{2.12}$$

with $P^u(\xi)$ being the global unbiased distribution. The F_i cannot directly be obtained from sampling. It can be done with the weighted histogram analysis method.

2.3.1 Weighted histogram analysis method

This method is used to calculate the global distribution by weighted average of distribution obtained from the individual sampling windows. It aims to minimize the statistical error of $P^u(\xi)$.

$$P^u = \sum_{i}^{windows} p_i(\xi) P_i^u(\xi) \tag{2.13}$$

The weights p_i are chosen in order to minimize the statistical error of P^u:

$$\frac{\partial \sigma^2(P^u)}{\partial p_i} = 0 \tag{2.14}$$

under the condition $\sum p_i$ = 1. This leads to

$$p_i = \frac{a_i}{\sum_j a_j}, a_i(\xi) = N_i exp[-\beta w_i(\xi) + \beta F_i] \tag{2.15}$$

where N_i is the total number of steps sampled for window *i*. The F_i are calculated by Eq. (2.12)

$$exp(-\beta F_i) = \int P^u(\xi) exp[-\beta w_i(\xi)] d\xi \tag{2.16}$$

Because P^u enters Eq. (2.16) and F_i enters Eq. (2.13) via Eq. (2.15), these have to be iterated until convergence. For many bins, this convergence can be slow.

2.4 Coarse grain simulation: Dissipative Particle Dynamics

As stated earlier, this thesis aims to connect all atomistic scale to coarse grain mesoscopic scale for polymer-nanotube composite systems. After gaining insights from the all atomistic simulations, it is required to translate informations into coarse-grained scale so that large scale structures and long scale dynamics can be studied which can be compared with experimental findings. To map the atomistic informations with mesoscopic parameters we need the help of Flory-Huggins theory of solubility. We have employed that to derive parameters for coarse grained simulation from the atomistic simulations. Details of that methodology has been discussed in chapter 5. Here we will discuss the general theoretical background of DPD simulation technique and a short description of Flory-Huggins solubility parameter. Dissipative particle dynamics (DPD) is one of the widely used coarse-graining methods in computational materials science field. Dissipative particle dynamics was proposed by Hoogerbrugge and Koelman [18] as an advanced method to simulate hydrodynamic phenomena. It is a particle based method where a dissipative particle represents the centre of mass of a mesoscopic portion of fluid. The particles occupy continuous positions r_i and velocities v_i. The time evolution of the particles is governed by Newton's equations of motion

$$\dot{r_i} = v_i \tag{2.17}$$

$$\dot{v_i} = \frac{f_i}{m_i} \tag{2.18}$$

where particles are labeled by i=1,2,...,N and m_i is the mass of particle i. The force experienced by the particle has three parts and each part is a sum of pair forces

$$f_i = \sum_{j \neq i} (F_{ij}^C + F_{ij}^D + F_{ij}^R) \tag{2.19}$$

The three contributions are a conservative force F_{ij}^C, a dissipative force F_{ij}^D and a random force F_{ij}^R. The conservative force is given by

$$F_{ij}^C = \begin{cases} a_{ij}\left(1 - \frac{r_{ij}}{r_c}\right)\hat{r_{ij}} & (r_{ij} < r_c) \\ 0 & (r_{ij} \geq r_c) \end{cases} \tag{2.20}$$

where a_{ij} is the maximum repulsion between particles i and j. r_c is the cut-off interaction range. The dissipative force is given by

$$F_{ij}^{D} = -\gamma\omega^{D}(r_{ij})(\hat{r_{ij}}.v_{ij})\hat{r_{ij}} \tag{2.21}$$

The random force is given by

$$F_{ij}^{R} = \sigma\omega^{R}(r_{ij})\zeta_{ij}\hat{r_{ij}}/(dt)^{1/2} \tag{2.22}$$

In the above equations r_{ij} = r_i - r_j, v_{ij} = v_i - v_j. γ and σ are the friction and noise strength respectively. ω^{D} (r_{ij}) and ω^{R} (r_{ij}) are weight functions that depict the range of the dissipative and random forces and vanish for $r¿r_c$. The term ζ_{ij} is a Gaussian random number which is symmetric with a zero mean and satisfies the properties

$$\langle\zeta_{ij}(t)\rangle = 0 \tag{2.23}$$

$$\langle\zeta_{ij}(t)\zeta_{i'j'}(t')\rangle = (\delta_{ii'}\delta_{jj'} + \delta_{ij'}\delta_{i'j})\delta(t-t') \tag{2.24}$$

To ensure that a well-defined thermodynamic equilibrium state exists the following relation must hold

$$\omega^{D}(r_{ij}) = [\omega^{R}(r_{ij})]^2 \tag{2.25}$$

This state holds Boltzmann statistics where the temperature is defined in terms of the fluctuation-dissipation relation

$$\sigma^2 = 2\gamma k_B T \tag{2.26}$$

In practice the weight functions are defined through

$$\omega^{D}(r_{ij}) = \begin{cases} \left(1 - \frac{r_{ij}}{r_c}\right)^2 & (r_{ij} < r_c) \\ 0 & (r_{ij} \geq r_c) \end{cases} \tag{2.27}$$

The symmetry of the forces in the indices i,j provides F_{ij}=-F_{ji} (Newton's Third Law) and ensures that the total momentum is conserved. The dissipative force is a frictional force that originates due to the relative velocities of particle. Due to dissipative interaction the particles will eventually slow down until they stop their relative motion. So another force is necessary to kick the particles in motion. This force is the random force which compensates the loss of kinetic energy due to

dissipative force and provides necessary kicks in the radial direction $\hat{r_{ij}}$ to keep the particles in thermal motion. The noise is symmetric with respect to indices i,j and thus, random kicks satisfy Newton's third law and conserve momentum. Both random and dissipative forces maintain the isothermal nature of collisions of the particles.

In DPD, each bead represents a collection of atoms or monomers and their atomic level details are ignored. Beads interact via soft repulsive force governed mainly by the repulsion parameter term a_{ij} in equation 4. Groot and Warren [19] showed that due to the repulsive nature of conservative force in DPD, the simulation of liquid-vapor interfaces is restricted. But liquid-liquid and solid-liquid interfaces can be simulated. So Flory-Huggins theory of polymer solution can be applied in this case. By Flory-Huggins theory the free energy of mixing of a binary solution can be calculated. If each repeating unit of a polymer is considered as a lattice point connected with other lattice points through bonds then Flory-Huggins theory can be applied to binary polymer solution also. The expression for free energy per lattice site for a two component system is given by

$$\frac{F_{AB}}{k_BT} = \left(\frac{\phi_A}{N_A}\right) ln\phi_A + \left(\frac{\phi_B}{N_B}\right) ln\phi_B + \chi\phi_A\phi_B \tag{2.28}$$

where ϕ_A and ϕ_B are the volume fraction for beads of type A and B, respectively. N_A and N_B are the number of segments per A and B molecule. All the lattice points are assumed to be occupied implicitly, and hence satisfy the relation ϕ_A + ϕ_B = 1.

Groot and Warren [19] suggested that the interaction parameter a_{AB} of conservative force can be mapped onto Flory-Huggins χ parameter by linear equation. If number of segments per A and B molecule is same (N_A=N_B) then the expression for Flory-Huggins parameter χ comes out to be

$$\chi = \frac{ln[(1-\phi_A)/\phi_A]}{1-2\phi_A} \tag{2.29}$$

Equation 2.29 is valid if the similar types of beads interact via same interaction parameter i.e. a_{AA}=a_{BB}. The linear relationship between Flory-Huggins χ parameter and Δa (a_{AA}-a_{BB}) as formulated by Groot and Warren [19] for different number densities is given by

$\chi = (0.286 \pm 0.002)\Delta a \ (\rho = 3)$

$\chi = (0.689 \pm 0.002)\Delta a \ (\rho = 5)$

For polymeric system of chain length ranging from 2 to 10, Groot and Warren [19] calculated the

linear relationship between excess repulsion parameter Δa and χ as

$$\chi = (0.306 \pm 0.003)\Delta a \ (\rho = 3) \tag{2.30}$$

Using informations obtained from experiment or atomistic simulations, Flory-Huggins parameter (χ) can be calculated from Hildebrand solubility parameter δ. The relationship between χ and Hildebrand solubility parameter δ has the following form

$$\chi \approx \frac{V_{avg}}{RT}(\delta_A - \delta_B)^2 \tag{2.31}$$

where V_{avg} is the average molar volume of beads A and B. Hildebrand solubility parameter δ can be calculated from experiment or simulations. In absence of experimental information atomistic MD simulations can be performed to calculate cohesive energy density (CED) from molar enthalpy of vaporization (non-bonded energy) and molar volume. The equation to get Hildebrand solubility parameter is given by

$$\delta_A = \left(\frac{\Delta H_A}{V_{m,A}}\right)^{1/2} = (CED_A)^{1/2} \tag{2.32}$$

where ΔH_A and $V_{m,A}$ are the molar enthalpy of vaporization and molar volume of molecule A, respectively. Thus calculating Hildebrand solubility parameter from simulation or experiment one can estimate χ and then building the relationship between χ and Δa by the procedure suggested by Groot and Warren [19] Δa (i.e. a_{ij}-a_{ii}) can be obtained.

To develop the parameters and analyze the results we have used self-written codes/scripts. Analyses such as partial densities, mean square displacement, bundle size analysis, structure factor, shape and size anisotropy, interfacial energies, orientation paramaters have been performed by self-written as well as in-house codes.

References

[1] Jorgensen, W. L.; Tirado-Rives, J. *J. Am. Chem. Soc.* **1988**, *110*, 1657–1666.

[2] Jorgensen, W. L.; Maxwell, D. S.; Tirado-Rives, J. *J. Am. Chem. Soc.* **1996**, *118*, 11225–11236.

[3] Cornell, W. D.; Cieplak, P.; Bayly, C. I.; Gould, I. R.; Merz, K. M.; Ferguson, D. M.; Spellmeyer, D. C.; Fox, T.; Caldwell, J. W.; Kollman, P. A. *J. Am. Chem. Soc.* **1995**, *117*, 5179–5197.

[4] A. D. MacKerell, J. et al. *J. Phys. Chem. B* **1998**, *102*, 3586–3616.

[5] Schuler, L. D.; Daura, X.; van Gunsteren, W. F. *J. Comput. Chem.* **2001**, *22*, 1205–1218.

[6] Allen, M. P.; Tildesley, D. J. *Computer simulation of liquids*; Clarendon Press: New York, NY, USA, 1987.

[7] Hess, B.; Bekker, H.; Berendsen, H. J. C.; Fraaije, J. G. E. M. *J. Comput. Chem.* **1997**, *18*, 1463–1472.

[8] Yoneya, M.; Berendsen, H. J. C.; Hirasawa, K. *Molecular Simulat.* **1994**, *13*, 395–405.

[9] Frenkel, D.; Smit, B. *Understanding Molecular Simulation*, 2nd ed.; Academic Press, Inc.: Orlando, FL, USA, 2001.

[10] Berendsen, H. J. C.; Postma, J. P. M.; Vangunsteren, W. F.; Dinola, A.; Haak, J. R. *J. Chem. Phys.* **1984**, *81*, 3684–3690.

[11] Nos, S. *J. Chem. Phys.* **1984**, *81*.

[12] Van Der Spoel, D.; Lindahl, E.; Hess, B.; Groenhof, G. *J. Comput. Chem.* **2005**, *26*, 1701–1718.

[13] Hess, B.; Kutzner, C.; van der Spoel, D.; Lindahl, E. *J. Chem. Theory Comput.* **2008**, *4*, 435–447.

[14] Kollman, P. A. et al. *Acc. Chem. Res.* **2000**, *33*, 889–897.

[15] Kirkwood, J. G. *J. Chem. Phys.* **1935**, *3*.

[16] Zwanzig, R. W. *J. Chem. Phys.* **1954**, *22*.

[17] Torrie, G. M.; Valleau, J. P. *Chem. Phys. Lett.* **1974**, *28*, 578.

[18] Hoogerbrugge, P. J.; Koelman, J. M. V. A. *Europhys. Lett.* **1992**, *19*, 155.

[19] Groot, R. D.; Warren, P. B. *J. Chem. Phys.* **1997**, *107*, 4423–4435.

Chapter 3

Structure and dynamics of polycarbonate-CNT composite

We report the structural and dynamical properties of polycarbonate-CNT composites obtained by performing all atomistic molecular dynamics simulations. The necessary force fields for CNT and polycarbonate have been calculated and validated. The detailed study of the interactions between CNT atoms and different polycarbonate moeties has been performed and discussed. The diffusivity of matrix has been studied at different temperatures. The dynamics of CNTs in the polycarbonate matrix is explored. The bundling of CNTs has been observed. The mechanism of bundling is elucidated.

3.1 Introduction

For the past few years carbon nanotube (CNT)-polymer composites have become an important field of study due to the improved structural and mechanical properties and the wide scope of applications in material sciences. A great deal of study, experimental as well as theoretical, has been performed and is going on this field to explore and analyze the structure and dynamics of nanocomposites. Polycarbonates are widely used as plastic material and have become very important industrially due to its good thermal and electrical resistivity and transparency. It has been observed that incorporation of CNTs in the polymer matrix can significantly enhance mechanical (strength and stiffness), thermal and electrical properties of polymer and thus CNTs can be used as potential reinforcing agent [1–8]. CNTs in polymer matrix provide large interfacial area and the nature of interactions in this interface region plays crucial role in determining the improvements in mechanical and dynamical properties of nanocomposites.

Polycarbonate nanocomposites were first synthesized by Zhao et al. [9] by solution mixing and were characterized by Raman spectroscopy. Potschke et al. [10] investigated distribution and alignment of CNT in polycarbonate composites by statistical analysis of TEM (transmission electron microscopy). The correlation function was used to measure CNT clustering quantitatively and to derive local orientation factors. The study revealed that CNT clustering can enhance electrical conductivity. Starr et al.[2] have investigated the influence of shape of nanoparticles on the viscosity of polymer-nanoparticle melt mixtures at high temperature and tensile strength in the ideal glass state by coarse-grain MD. Ruoff et al. [11] studied the sheathing of polymer in MWCNT-polycarbonate composites by SEM. They have found out substantial evidence that suggests multiple polymer layers sheath nanotubes giving direct evidence for tube-polymer interaction. Argon et al. [12] performed quasi-static simulation on glassy Bisphenol A polycarbonate with a static atomistic model to investigate the phenylene ring flip, conformational changes associated with the carbonate group and the influence of the cooperative effect on main-chain dynamics. Fan et al. [13] used modified version of Dreiding force field. The validity of this modified force field obtained by optimization of few parameters by $ab\ initio$ calculations was tested on a model polycarbonate compound and matched with crystallographic data. To propose a mechanism for the infrequent phenyl ring π-flips

in polycarbonate was a challenging job. For this, instead of Newton's equation, Whitney and Yaris [14] have used Langevin equation as the equation of motion to simulate phenyl ring flips in glassy polycarbonate. Eilhard, Zirkel and co-workers [15] combined neutron scattering and computer simulations to gain deeper insight into the structure of polycarbonate melt. For simulation they have introduced coarse graining to get a mesoscopic model from atomistic model. Meyer et al. [16] developed two all-atom force fields for Diphenyl Carbonate (DPC) which is the main building block of the polycarbonate. One was derived from Hartree-Fock calculations and other was from DFT calculations. Then they have performed simulation using these force fields separately to evaluate the structure and dynamics of liquid DPC over a wide temperature range and compared the data obtained by these two force fields. Müller-Plathe et al. [17] proposed a new mechanism for diffusion of phenol molecules in bisphenol-A-polycarbonate melt using MD simulation. This mechanism is different from that of smaller gaseous molecules which are known to penetrate the polymer matrix by hopping between pre-existing voids. The analysis revealed a transition from hopping diffusion towards more continuous diffusion at higher temperatures than 500 K. Kremer et al. [18] used coarse-grained MD simulations of polycarbonate to investigate chain dynamics, intramolecular structure, determination of entanglement molecular weight etc.

Polymer nanocomposites are the new materials and getting lot of attention due to its tunable properties by changing the mixing ratios and mixing procedure of nanoparticles in the polymer matrix. Study of structural and dynamical properties of CNT-polycarbonate composite was not done before theoretically. In this thesis we have studied the structure and dynamics of nanocomposites by simulating single wall carbon nanotube SWCNT-dispersed monomers and trimers of polycarbonate by fully atomistic molecular dynamics (MD) simulation. In experiments [19–25], it is quite common feature of CNTs to agglomerate due to strong cohesive force between CNTs. No studies on the mechanism and energetics of bundle formation of SWCNT in the monomeric and oligomeric polycarbonate matrix have been done till now. We have explored the mechanism and energetics (energetics described in the next chapter) of bundling of CNTs in the matrix for the first time to the best of our knowledge.

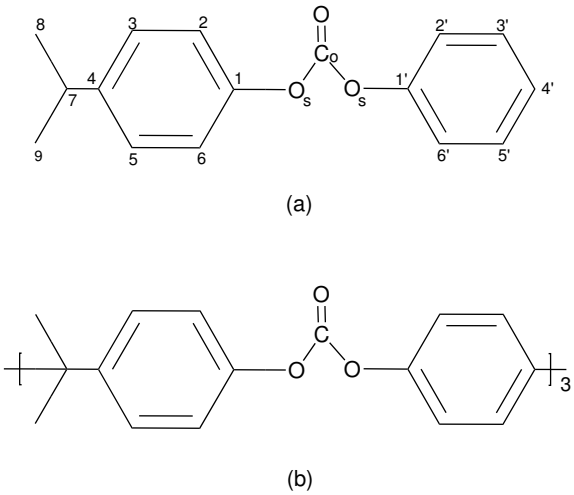

Figure 3.1: (a) Structure of monomer unit with atom numbering as used in the text. Hydrogen atoms carry the label number of carbon atoms they are attached to. (b)Structure of trimer unit.

3.2 Computational Details

Molecular Dynamics (MD) simulations of pure monomer and trimer of amorphous polycarbonate and systems mixed with different molecular weight percentages of SWCNT have been studied with an all atom force field using MD code GROMACS 4.0.7 [26, 27]. The total potential energy we have used is the sum of harmonic bond angle potential, proper dihedral potential with both periodic and Ryckaert-Bellemans [28, 29] forms, improper dihedral potential, non-bonded interactions consisting of Lennard-Jones potential and point-charge electrostatics. As discussed above Meyer et al. [16] and Müller-Plathe et al. [17] studied the properties of Diphenyl Carbonate (DPC) and Bisphenol-A (BPA) respectively. Most of the bonded and non-bonded parameters are taken from these two papers. Meyer et al.[16] developed two sets of partial charges and proper dihedral parameters for diphenyl carbonate (DPC) and studied physical properties using two sets of parameters. We have adopted the second set of the force field parameters (which they have recommended) for that part of our monomer structure (Figure 3.1a) which is similar to the diphenyl carbonate. For the isopropyl part of monomer (fig. 3.1a), we have taken parameters (except partial charges) from Müller-Plathe et al.[17]. For the determination of partial charges for isopropyl group, we have calculated electrostatic potential (ESP) with B3LYP and 6-311G** basis set (same as Meyer et al. has done for DPC) using GAUSSIAN 09 [30]. We have adopted partial charges for the atoms of

isopropyl group and for C_7, C_8, C_9 from this calculation. For the rest of the atoms, we have kept the partial charges intact as reported by Meyer et al. for DPC. Some partial charges are adjusted carefully to maintain overall charge neutrality for monomer and trimer units.

All the force field parameters used for monomer and trimer are given in Table 3.1-3.5. The bond angle and angle constants of $C_4 - C_7 - H_7$ and $C_{8,9} - C_7 - H_7$, the proper dihedral (Ryckaert-Bellemans) parameters are taken from OPLS [31, 32] force field. We have excluded all 1-4 non-bonded interactions and kept bond lengths constant in accordance with Meyer et al. [16] For CNT we have used OPLS [31, 32] force field parameters. Charges on the atoms of nanotube are taken as zero.

We have prepared system of pure monomers at 500 K and gradually cooled down by 20 K to 380 K. Simulated annealing is performed by raising temperature from 500 K to 1000 K and cooling down to 500 K with the steps of 25 K and annealing time of 25 ps. Approximately 2%, 5% and 10% by molecular weight of SWCNT-monomer mixtures are prepared at temperatures 500 K, 480 K and 460 K. 2%, 5% and 10% mixtures contain 5, 10 and 15 SWCNTs respectively. We have taken a zig-zag single walled CNT of diameter 4.69 Å and length 40.7 Å consisting of 240 atoms. We have used Berendsen [33] thermostat with coupling time of 0.2 ps and Berendsen barostat with pressure of 1 bar. Isotropic pressure coupling is used with coupling times of 1.5 ps. Periodic boundary conditions are applied in all three directions for all the systems. Bond lengths are kept constant using LINCS algorithm [34]. Reaction Field electrostatics is used with cut-off length 1.2 nm and dielectric constant, $\epsilon_{RF} = 3.5$. Integration time step is 2 fs. The monomeric systems are pre-equilibrated for 1 ns, equilibrated for 10 ns and final production run is performed for another 10 ns at three different temperatures.

For trimer, we have prepared the pure trimer system at 520 K, 500 K, 490 K, 480 K, 460 K and 440 K. Simulated annealing is performed to sample the phase space properly because of long chains of the oligomers. In simulated annealing the temperature is raised from 500 K to 900 K and cooled down to 500 K with the step of 40 K. The annealing time for each step is 400 ps. Systems are equilibrated for 40 ns and production-runs are performed for additional 50 ns. 2%, 5%, 10% of SWCNT-trimer mixtures are also prepared at 500 K, 480 K and 460 K in the similar way. The

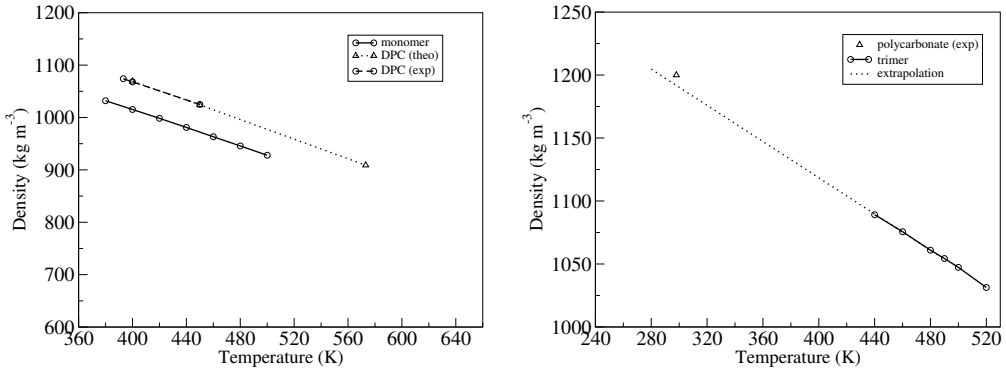

Figure 3.2: (a)Density of pure monomer as function of temperature along with the theoretical and experimental densities of DPC. (b) Density of pure trimer as function of temperature with experimental value of density of polycarbonate.

number of CNTs in three different mixtures are same as in case of CNT-monomer mixtures. These mixed systems are subjected to equilibration run for 30 ns and production run for additional 20 ns. Temperature coupling is used with coupling times of 0.1 ps. All other control parameters for MD are same as in the case of the monomer systems.

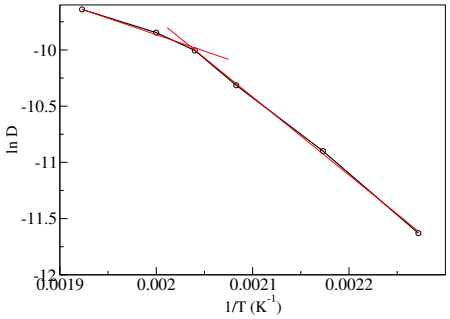

Figure 3.3: Natural logarithm of diffusion coefficients as a function of inverse of temperature for pure trimer.

3.3 Validation of Force Field

To validate the force fields, we focused on two properties to examine, density and glass transition temperature. We have calculated the densities at different temperatures and plotted as a function of temperature for both pure monomer (Figure 3.2a) and trimer (Figure 3.2b) and compared the densities with the densities (both experimental and theoretical) of Diphenyl carbonate (DPC) as

reported by Meyer et al. [16]. From Figure 3.2a, we can see that DPC has higher densities (both experimental and theoretical) than the densities of pure monomer we have calculated theoretically. But in case of pure trimer system, when we have done linear fitting of the density as a function of temperature plot between 490 K and 440 K and extrapolated it (Figure 3.2b), the extrapolated straight line passed very close to the experimental density of polycarbonate [35] at room temperature. To find the glass transition temperature and compare with the experimental value, we have calculated diffusion coefficients at different temperatures for pure trimer system. The experimental glass transition temperature for polycarbonate is 418-432 K [36–38]. To find the diffusion coefficient of trimer, at each temperature mean square displacement (MSD) is plotted for every 10 ns of trajectory starting from 40 ns to 90 ns and then averaged over to get an average MSD reported in Figure 3.4.

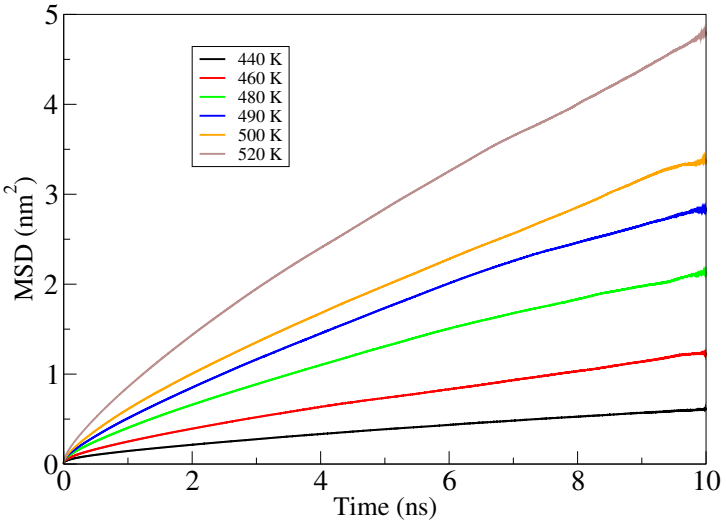

Figure 3.4: Average MSD plots of pure trimer at different temperatures.

Natural logarithm of diffusion coefficients as a function of inverse of temperature has been shown in Figure 3.3 and linear fitting has been done between 520 K and 490 K and another between 490 K and 440 K. In Figure 3.3, it is observed that a steep decrease in diffusion coefficient starts near 490 K which indicates that the glass transition temperature is near to 490 K. In comparison to the experimental glass transition temperature for polycarbonate, the deviation is less than 15%. As we are simulating oligomeric polycarbonate the 15% deviation in glass temperature is acceptable.

Table 3.1: LJ and coulombic potential parameters

atom	σ/nm	ϵ/kJ mol^{-1}	q_i/e
O_s	0.300	0.712	-0.308
C_o	0.340	0.360	0.630
O	0.296	0.880	-0.378
$C_{1,1'}$	0.355	0.294	0.294
$C_{2,2',6,6'}$	0.355	0.294	-0.210
$C_{3,5}$	0.355	0.294	-0.190
$C_{3',5'}$	0.355	0.294	-0.042
C_4	0.355	0.294	-0.096
C'_4	0.355	0.294	-0.133
C_7	0.3207	0.3519	0.234
$C_{8,9}$	0.350	0.336	-0.186
$H_{2,2',6,6'}$	0.242	0.126	0.126
$H_{3,5}$	0.242	0.126	0.125
$H_{3',5'}$	0.242	0.126	0.091
H'_4	0.242	0.126	0.091
H_7	0.257	0.210	-0.012
$H_{8,9}$	0.257	0.210	0.040

* Atom names are used as in Figure 3.1a in the thesis.

Table 3.2: Bond distances

bond constraint	distance/nm
C_o-O	0.118
C_o-O_s	0.132
O_s-C_1	0.139
C_{aro}-C_{aro}	0.139
C_{aro}-H_{aro}	0.108
$C_{aro:4}$-$C_{ali:7}$	0.154
$C_{ali:7}$-$C_{ali:8,9}$	0.154
$C_{ali:8,9}$-$H_{8,9}$	0.110
C_7-H_7	0.110

Table 3.3: Bond angle and angle constants

bond angle	$\theta_0/\circ$	k_θ/kJ mol^{-1}rad^{-2}
O_s-C_o-O_s	108.00	418.80
O_s-C_o-O	126.00	418.80
C_1-O_s-C_o	121.40	418.80
$C_{2,6}$-C_1-O_s	120.00	418.80
C_{aro}-C_{aro}-C_{aro}	120.00	376.60
C_{aro}-C_{aro}-H_{aro}	120.00	418.80
$C_{aro:4}$-C_7-$C_{8,9}$	109.45	376.60
$C_{aro:4}$-C_7-H_7	109.30	292.88
C_8-C_7-C_9	109.45	376.60
$C_{8,9}$-C_7-H_7	110.70	313.80
C_7-C_4-$C_{3,5}$	120.00	376.60
C_7-$C_{8,9}$-$H_{8,9}$	109.45	366.90
$H_{8,9}$-$C_{8,9}$-$H_{8,9}$	109.45	306.40
C_{aro}-C_{ali}-C_{aro}	109.45	376.60

Table 3.4: Proper dihedral parameters

proper dihedrals (Periodic)	ϕ_s/deg	k_ϕ/kJ mol^{-1}	multiplicity
O_s-C_o-O_s-$C_{1'}$	180	11.0	2
C_1-O_s-C_o-O	180	11.0	2
C_o-O_s-C_1-$C_{6'}$	180	0.75	2
C_6-C_1-O_s-C_o	180	0.75	2
C_{aro}-C_{aro}-C_{ali}-C_{aro}	0.0	0.5	4

Table 3.5: proper dihedrals (Ryckaert-Bellemans)

proper dihedrals (Ryckaert-Bellemans)	k(0)	k(1)	k(2)	k(3)	k(4)	k(5)
C_8-C_7-C_4-C_5	0.00	0.00	0.00	0.00	0.00	0.00
C_4-C_7-$C_{8,9}$-$H_{8,9}$	0.9665	2.8995	0.00	-3.86601	0.00	0.00
C_{ali}-C_{ali}-C_{ali}-H_{ali}	0.6276	1.8828	0.00	-2.51040	0.00	0.00

* units are in kJ mol^{-1}

Table 3.6: Improper dihedral parameters

Improper dihedrals	ξ_0/deg	k_ξ/kJ mol^{-1}
C_{aro}-C_{aro}-C_{aro}-C_{aro}	0.00	167.4
C_{aro}-C_{aro}-C_{aro}-C_{ali}	0.00	167.4
C_{aro}-C_{aro}-C_{aro}-H_{aro}	0.00	167.4
C_{aro}-C_{aro}-C_{aro}-O_s	0.00	167.4
C_o-O_s-O_s-O	0.00	167.4

3.4 Results and Discussion

3.4.1 Structural Properties

To investigate the structural environment around CNT in monomer and trimer mixtures, radial distribution function (RDF) is calculated between CNT's carbons and four types of atoms of monomer and trimer: carbonyl oxygen, carbonyl carbon, bridge oxygen and aromatic carbon at 500 K for three different mixtures (2%, 5%, 10%) depicted in Figure 3.5 and Figure 3.6. For 2% mixtures of both monomer and trimer, we see that minima of first peaks for carbonyl oxygen, bridge oxygen, carbonyl carbon and aromatic carbon are approximately at 0.45 nm, 0.65 nm, 0.70 nm and 0.70 nm respectively. For carbonyl oxygen, second minimum is at around 0.66 nm. For carbonyl carbon, second minimum is observed at around 1.05 nm. For 5% and 10% mixtures also, these distances are almost same. The structural environment around CNTs is not changing with CNT content and it remains same if we go from monomer to trimer matrix. The absence of any sharp peak in RDF plots indicates that the interaction between CNT carbons and these four types of atoms of matrix molecules is less attractive in nature. There is almost no wetting of molecules and therefore, CNTs have high tendency to self-assemble which leads to the formation of bundles.

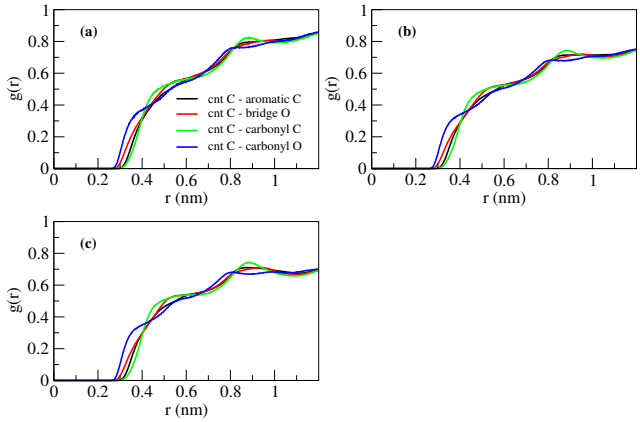

Figure 3.5: RDFs between carbonyl oxygen of monomer and CNT carbons, bridge oxygens of monomer and CNT carbons, carbonyl carbons of monomer and CNT carbons, aromatic carbons of monomer and CNT carbons. (a) 2% mixture, (b) 5% mixture, (c) 10% mixture.

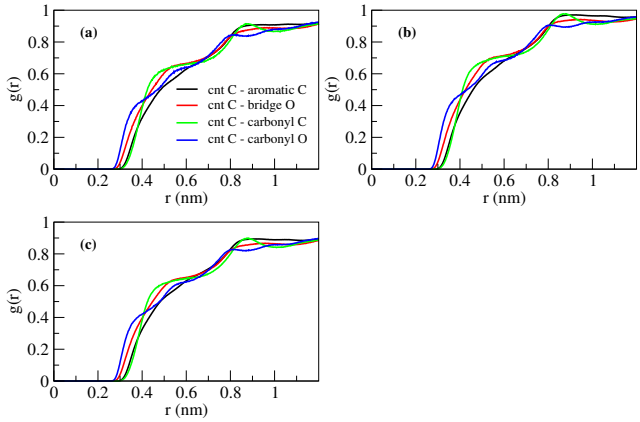

Figure 3.6: RDFs same as figure 4 but for CNT-trimer composite system. (a) 2% mixture, (b) 5% mixture, (c) 10% mixture.

3.4.2 Mean Square Displacement

The dynamical as well as rheological properties of polymers incorporated with nanomaterials have been studied previously experimentally and theoretically[1–3, 39]. Wei et al.[39] studied the diffusion behaviours of pure polyethylene (PE) and CNT-polyethylene composite by molecular dynamics (MD) using united atom force field and found out that diffusion coefficient of polyethylene has increased from pure polymer to CNT-polymer composite at a fixed temperature. They have explained it on the basis of thermal expansion coefficient. Increased thermal expansion of composite enhanced the diffusivity of the polymer above glass transition temperature. Their study also showed that with increase in temperature diffusion coefficient of polymer increases for both pure and mixed systems. Figure 3.7a and 3.7b show the mean square displacement (MSD) of center of mass of monomer and trimer respectively in different mixtures at three different temperatures. The slope of the graph is decreasing with decrease in temperature for a fixed percentage mixture. Due to the decrease in kinetic energy of molecules with the decrease of temperature, diffusivity of molecule gets lowered. The slope of MSD graphs (Figure 3.7a and 3.7b) also decreases with the increase in CNT content in the matrix. Interestingly pure monomer and trimer systems has lower slopes for MSD than 2% CNT-monomer/trimer composites. To compare the self diffusion behaviour of the centres of masses of the monomer and the trimer in pure system and three different mixtures of CNT-monomer and CNT-trimer at three different temperatures, we have calculated diffusion coefficients from the average MSD (Figure 3.7a and 3.7b) calculated from 5 sets of 2 ns trajectories of production run . When we compared the diffusion coefficients of pure monomer and 2% mixture at different temperatures we have observed the increase in the diffusion constant, as reported in Table 3.7. In case of trimer systems (Table 3.8), increase in diffusion coefficients is also observed when we have compared between pure and 2% mixture system. However, with the increase in CNT content i.e. in 5% and 10% systems, the diffusion constant for monomer and trimer decreases. For 5% and 10% mixed systems, glass transition temperature may have increased (glass transition temperature of pure trimer is 490 K) and this may be a reason for the decrease of diffusion coefficient. As it is computationally costly to simulate different mixed systems for wide range of temperatures, the investigation of glass transition temperature for mixed systems has not been

Table 3.7: Diffusion Coefficients of monomer (10^{-5} cm^2/s)

Temperature (K)	Neat monomer	2%	5%	10%
500	2.0914±0.0479	2.2124±0.0545	2.1407±0.0285	1.9543±0.0922
480	1.7273±0.0985	1.8090±0.0646	1.7569±0.0551	1.6047±0.0372
460	1.3153±0.1020	1.4869±0.0299	1.4198±0.0325	1.3647±0.0657

Table 3.8: Diffusion Coefficients of trimer in 10^{-5} cm^2/s

Temperature (K)	Neat trimer	2%	5%	10%
500	0.0737±0.0053	0.0757±0.0030	0.0683±0.0013	0.0581±0.0031
480	0.0473±0.0073	0.0518±0.0015	0.0455±0.0023	0.0368±0.0024
460	0.0247±0.0020	0.0282±0.0011	0.0247±0.0017	0.0182±0.0011

performed presently. In experiments, viscosities of different polymers embedded with nanoparticles or CNTs or nanofibres have been studied [1, 3]. As it is difficult to measure viscosity with accuracy by fully atomistic molecular dynamics, we have not investigated viscous properties here.

To get better statistics of diffusivity of CNTs (as the number of CNT is less) we have plotted MSDs of CNTs at 2 ns intervals for 10 ns of production run and averaged over both in case of monomer (Figure 3.8a) and trimer (Figure 3.8b) matrices. In case of monomer matrices (Figure 3.8a), MSD plots are showing that diffusivity of CNT decreases with increasing CNT percentage at a particular temperature. For 10% mixtures diffusivity is quite low and this fact can be attributed to the high tendency of bundle formation by the CNTs. In case of trimer matrices (Figure 3.8b), the diffusivity of CNT is lower than that in monomer. For initial 100-120 ps the MSD plots are showing parabolic nature. This may be due to the fact that the trimer matrices have acquired some glassy behaviour at these three temperatures and due to repulsive interaction between CNT and polymer, within this very short time period CNTs follow the path like straight line with constant velocity before facing collision with other CNTs. CNTs are also confined in the molecular matrix. Monomer matrix is much liquid-like but the trimer matrix can create lot of confinement due to its long chains. Therefore MSD of only one of the CNTs over 10 ns production runs for each mixture at three different temperatures have been shown in Figure 3.8c and 3.8d for both monomer and trimer systems respectively. The graphs are quite non-linear in pattern and some of them cross

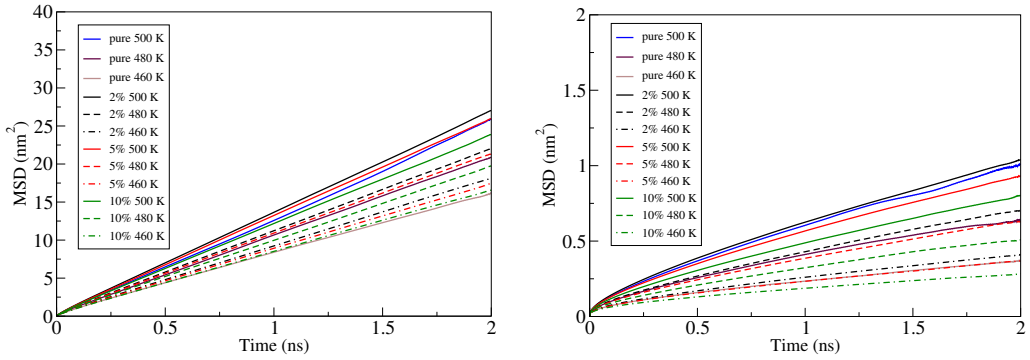

Figure 3.7: MSD plots for pure, 2%, 5%, 10% mixtures for (a) monomer, (b) trimer at 500 K, 480 K, 460 K.

each other. This behaviour of diffusion of CNTs indicates the confined motion of CNTs in the matrices.

Like in monomer matrices, diffusivity of CNTs is decreasing with higher CNT content. The probability of bundle formation increases with higher number of CNTs and therefore, the diffusivity of CNT gets decreased. While investigating the dynamics of CNTs in the matrix for monomer systems we have found out that CNTs are aligned in parallel fashion and agglomerating with each other. In 10% mixture of monomer, we have clearly observed the formation of bundles and alignment of CNTs in parallel fashion. The agglomeration of CNTs in polymer composite is reported experimentally[19–25]. Due to high cohesive energy CNTs tend to agglomerate in polymer melt. This bundle formation phenomena propelled us to investigate the mechanism associated with and the energetics which can explain the alignment and agglomeration of CNTs in composite.

3.4.3 Bundle Formation: Mechanism

To represent the mechanism of bundle formation and the structural changes in the CNT-monomer interface regions while bundle formation is going on (when equilibrating the system), we have examined the structural changes surrounding CNTs. For this we have chosen 1-21 ns trajectory of 10% mixture of monomer-CNT at 500 K as this system consists of maximum number of CNTs. To examine the probability that the centre of masses of CNTs are coming closer with time, the

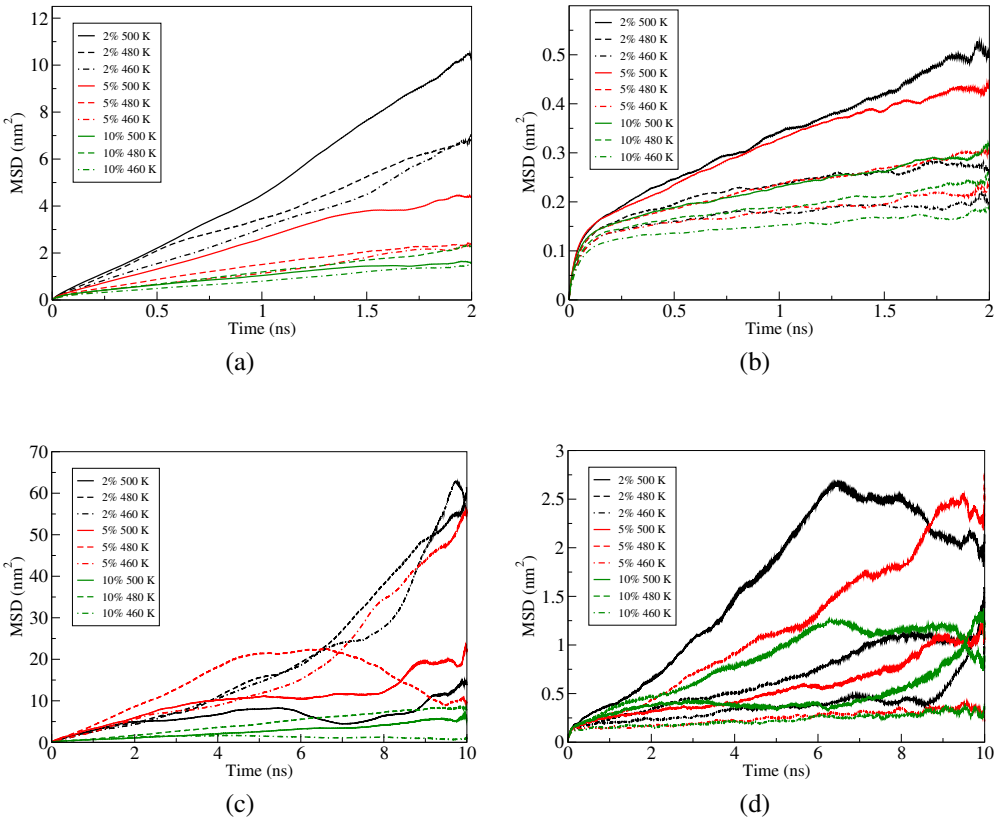

Figure 3.8: MSDs at 500 K, 480 K, 460 K for 2%, 5%, 10% mixtures for (a) all the CNTs in 2 ns intervals averaging over 10 ns in monomer matrix, (b) all the CNTs in 2 ns intervals averaging over 10 ns in trimer matrix, (c) only one of the CNTs in monomer matrix for 10 ns of production run, (d) only one of the CNTs in trimer matrix for 10 ns of production run.

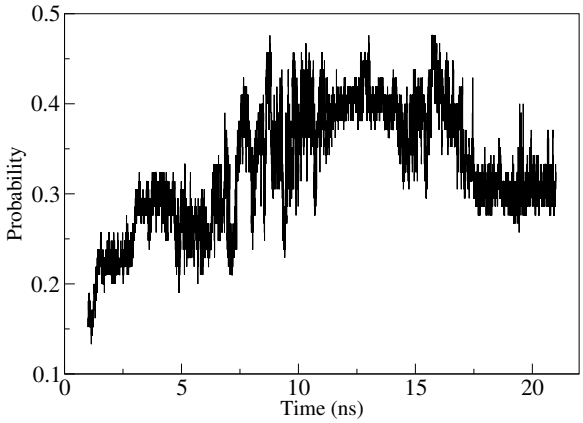

Figure 3.9: Probability of CNT centre of masses coming within the distance of 2 nm as a function of time.

cut-off distance between the centre of masses of CNTs is taken as 2 nm which is a reasonable approximation to explore bundling formation phenomena. At each frame the distances between all the CNTs have been calculated and the number of distances whose value falls below 2 nm were calculated and divided by the total number of probable distances. Figure 3.9 represents how the probability that the centre of masses of CNTs coming closer is changing with time. We can see that the probability is increasing with time which indicates that the CNTs are coming close to each other with time leading to the bundle formation. Figure 3.10 shows the change of average angle between the CNTs with time. For this, each CNT is represented by a vector and angles between the vectors were calculated at each frame only if the centre of mass distance between the corresponding CNTs comes within cut-off distance of 2 nm. It shows that average angle is rapidly decreasing with time and comes close to zero degree after 3-4 ns. Thus, it is clear that CNTs are not only coming close to each other with time, also they are aligning in a definite pattern which is parallel arrangement. Figure 3.11 represents the distribution of angles between the CNTs over 10 ns of production run considering the same cut-off distance between the centre of masses of CNTs. Distinct peak appeared near 2° indicates clearly that the CNTs have high tendency to be aligned parallel while agglomerating. In Figure 3.12, a snapshot of equilibrated CNT-monomer system showing the bundle formation has been depicted.

The structural changes at CNT-monomer interface during bundle formation has been investigated. We have selected four types of atoms of monomer (carbonyl oxygen, bridge oxygen, carbonyl

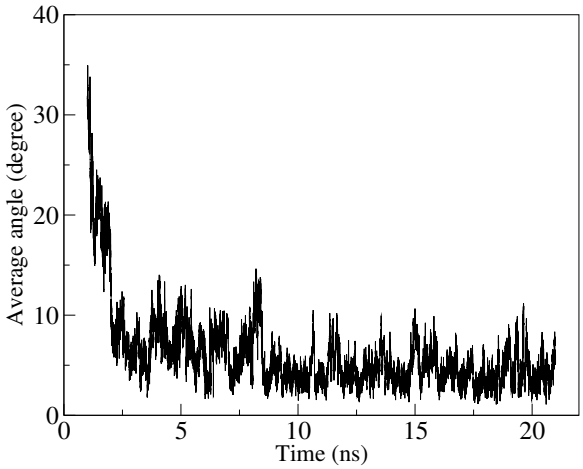

Figure 3.10: Change of average angle between the CNTs with time.

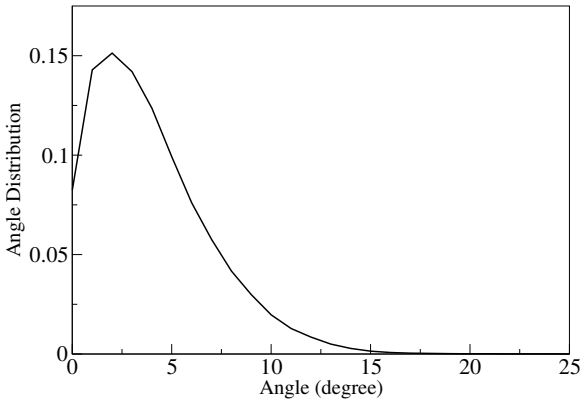

Figure 3.11: Distribution of angles between the CNTs for 10 ns production run of 10% at 500 K.

carbon and aromatic carbon) to see how their spatial proximity with carbon atoms of CNT changes with time. Each carbon atom of CNT is considered as the centre of a sphere with a definite radius within which the change of average number of various atoms of monomer is determined. For carbonyl oxygen, bridge oxygen, carbonyl carbon and aromatic carbon of monomer, graphs of radial distribution function with respect to the CNT carbon have been reported in Figure 3.5 and 3.6. For each type of atoms, the distances at which the minima of first peaks (first solvation shell) have appeared in radial distribution plots are considered as the radius of the corresponding sphere. For a particular type of atom, the distances from each CNT carbons are calculated. Only those atoms are recognized whose distances from CNT carbon fall within the defined radius at each time frame.

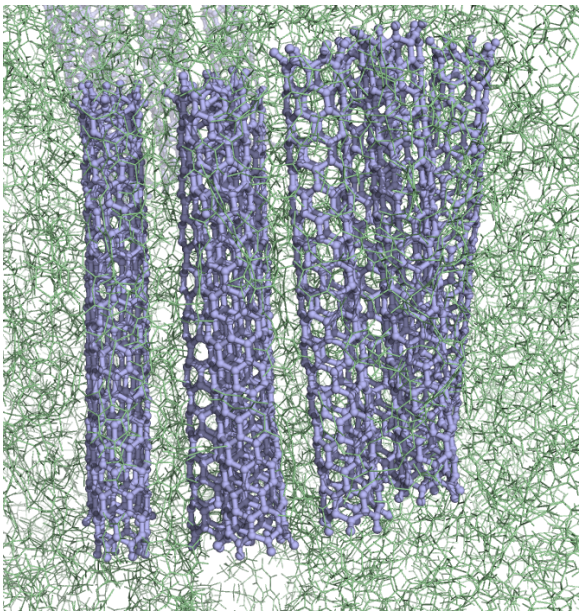

Figure 3.12: Snapshot of bundle of nanotubes in equilibrated 10% monomer matrix at 500 K.

Figure 3.13 shows the change of average number of four types of atoms with time. All the four plots are showing that average number is decreasing with time as CNTs are coming closer to each other to form bundles. In case of carbonyl oxygen (Figure 3.13a), we can see that the average number is quite less than other three types of atoms at initial time and its decrease with time is small compared to other. Due to less attractive interaction between CNT carbons and carbonyl oxygens the number of carbonyl oxygens present in first solvation shell of CNT carbons is very less and hence the decrease of the number of carbonyl oxygens during bundle formation is also insignificant. For bridge oxygen (Figure 3.13b), carbonyl carbon (Figure 3.13c) and aromatic carbon (Figure 3.13d) the decrease in number with time is significant compared to carbonyl oxygen. The number of bridge oxygen atoms show higher decrease than carbonyl oxygens. Carbonyl carbon and aromatic carbon have almost similar trend and they have greater average value than both bridge oxygen and carbonyl oxygen. This comparison gives an idea how these four types of atoms participate in structural changes around CNT carbons in bundle formation process.

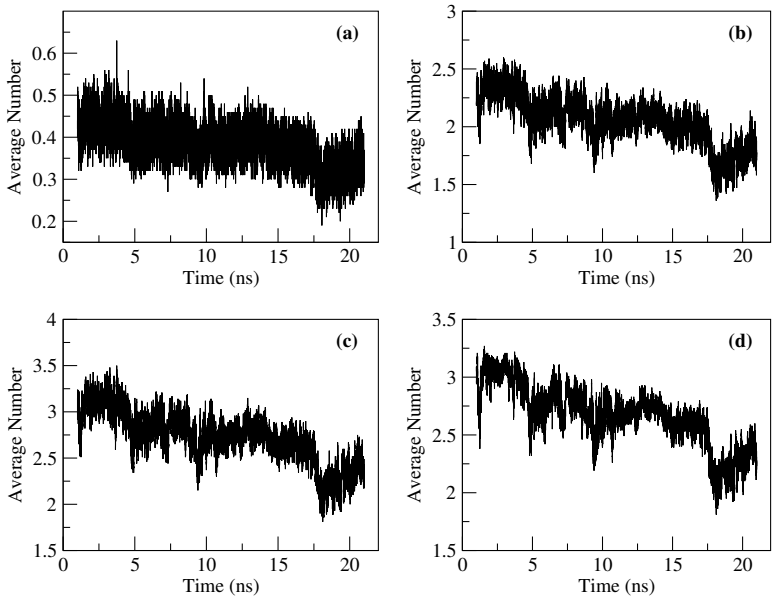

Figure 3.13: Change in average number of (a) carbonyl oxygen, (b) bridge oxygen, (c) carbonyl carbon, (d) aromatic carbon with time during bundle formation in 10% CNT-monomer mixture at 500 K.

3.5 Conclusions

Molecular dynamics simulation has been performed on pure and CNT mixed systems of monomer and trimer of polycarbonate at different temperatures. The structural environment remains intact for both monomer and trimer at three different mixtures of CNTs at three different temperatures (500 K, 480 K, 460 K). RDF plots indicate that less attractive interaction between the carbons of CNT and atoms of matrix molecules predominates in the composite. Investigation of the diffusion behaviour of solvent molecules in different mixtures reveals that with increasing percentage of CNT at a fixed temperature, the diffusivity of solvent molecules decreases. MSD graphs of individual CNTs showed much non-linearity due to their confined motion and bundle formation of CNTs has been observed in monomer matrices prominently in case of 10% mixture. Then we have looked into the details of bundle formation mechanism analysing 10% mixed system at 500 K.

References

[1] Potschke, P.; Fornes, T. D.; Paul, D. R. *Polymer* **2002**, *43*, 3247–3255.

[2] Starr, F. W.; Knauert, S. T.; Douglas, J. F. *J. Polym. Sci. Part B: Polym. Phys.* **2007**, *45*, 1882–1897.

[3] Lozano, K.; Bonilla-Rios, J.; Barrera, E. V. *J. Appl. Polym. Sci.* **2001**, *80*, 1162–1172.

[4] Lozano, K.; Barrera, E. V. *J. Appl. Polym. Sci.* **2001**, *79*, 125–133.

[5] Subramoney, S. *Adv. Mater.* **1998**, *10*, 1157–1171.

[6] Dickey, E. C.; Qian, D. *Appl. Phys. Lett.* **2000**, *76*, 2868–2870.

[7] Coleman, J. N.; Gun'ko, Y. K.; Khan, U. *Adv. Mater.* **2006**, *18*, 689–706.

[8] Coleman, J. N.; Cadek, M.; Blake, R.; Nicolosi, V.; Ryan, K. P.; Belton, C.; Fonseca, A.; Nagy, J. B.; Gun'ko, Y. K.; Blau, W. J. *Adv. Funct. Mater.* **2004**, *14*, 791–798.

[9] Zhao, Q.; Wood, J. R.; Wagner, H. D. *J. Polym. Sci., Part B: Polym. Phys.* **2001**, *39*, 1492–1495.

[10] Potschke, P.; Pegel, S.; Villmow, T.; Stoyan, D.; Heinrich, G. *Polymer* **2009**, *50*, 2123–2132.

[11] Ruoff, R. S.; Ding, W.; Eitan, A.; Fisher, F. T.; Chen, X.; Dikin, D. A.; Andrews, R.; Brinson, L. C.; Schadler, L. S. *Nano Lett.* **2003**, *3*, 1593–1597.

[12] Argon, A. S.; Hutnik, M.; Suter, U. W. *Macromolecules* **1991**, *24*, 5970–5979.

[13] Fan, C. F.; Cagin, T.; Chen, Z. M. *Macromolecules* **1994**, *27*, 2383–2391.

[14] Yaris, R.; Whitney, D. R. *Macromolecules* **1997**, *30*, 1741–1751.

[15] Eilhard, J.; Zirkel, A.; Tschop, W.; Hahn, O.; Kremer, K.; Scharpf, O.; Richter, D.; Buchenau, U. *J. Chem. Phys.* **1999**, *110*, 1819–1830.

[16] Meyer, H.; Hahn, O.; Muller-Plathe, F. *J. Phys. Chem. B* **1999**, *103*, 10591–10598.

[17] Muller-Plathe, F.; Hahn, O.; Mooney, D. A.; Kremer, K. *J. Chem. Phys.* **1999**, *111*, 6061.

[18] Kremer, K.; Delle Site, L.; van der Vegt, N.; Leon, S. *Macromolecules* **2005**, *38*, 8078–8092.

[19] Potschke, P.; Kasaliwal, G. R.; Pegel, S.; Goldel, A.; Heinrich, G. *Polymer* **2010**, *51*, 2708–2720.

[20] Potschke, P.; Pegel, S.; Petzold, G.; Alig, I.; Dudkin, S. M.; Lellinger, D. *Polymer* **2008**, *49*, 974–984.

[21] Micusik, M.; Omastova, M.; Krupa, I.; Prokes, J.; Pissis, P.; Logakis, E.; Pandis, C.; Potschke, P.; Pionteck, P. *J. Appl. Polym. Sci.* **2009**, *113*, 2536–2551.

[22] Du, F. M.; Scogna, R. C.; Zhou, W.; Brand, S.; Fischer, J. E.; Winey, K. I. *Macromolecules* **2004**, *37*, 9048–9055.

[23] Masuda, J.; Torkelson, J. M. *Macromolecules* **2008**, *41*, 5974–5977.

[24] Baets, J.; Godara, A.; Devaux, J.; Verpoest, I. *Compos Part A-Appl s* **2008**, *39*, 1756–1761.

[25] Potschke, P.; Kasaliwal, G. R.; Goldel, A. *J. Appl. Polym. Sci.* **2009**, *112*, 3494–3509.

[26] Van Der Spoel, D.; Lindahl, E.; Hess, B.; Groenhof, G. *J. Comput. Chem.* **2005**, *26*, 1701–1718.

[27] Hess, B.; Kutzner, C.; van der Spoel, D.; Lindahl, E. *J. Chem. Theory Comput.* **2008**, *4*, 435–447.

[28] Ryckaert, J. P.; Bellemans, A. *Chem. Phys. Lett.* **1975**, *30*, 123.

[29] Ryckaert, J. P.; Bellemans, A. *Disc. Farad. Soc.* **1978**, *66*, 95.

[30] Frisch, M. J. et al. Gaussian 09 Revision A.1. 2009; Gaussian Inc. Wallingford CT 2009.

[31] Jorgensen, W. L.; Tirado-Rives, J. *J. Am. Chem. Soc.* **1988**, *110*, 1657–1666.

[32] Jorgensen, W. L.; Maxwell, D. S.; Tirado-Rives, J. *J. Am. Chem. Soc.* **1996**, *118*, 11225–11236.

[33] Berendsen, H. J. C.; Postma, J. P. M.; Vangunsteren, W. F.; Dinola, A.; Haak, J. R. *J. Chem. Phys.* **1984**, *81*, 3684–3690.

[34] Hess, B.; Bekker, H.; Berendsen, H. J. C.; Fraaije, J. G. E. M. *J. Comput. Chem.* **1997**, *18*, 1463–1472.

[35] http://www.par-group.co.uk

[36] Brydson, J. A. *Plastic Materials*; Butterworth: London, 1982.

[37] Henrichs, P. M.; Luss, R. H.; Scaringe, R. P. *Macromolecules* **1989**, *22*, 2731–2742.

[38] Sommer, K. et al. *Adv. Mater.* **1991**, *3*, 590–599.

[39] Wei, C.; Srivastava, D.; Cho, K. *Nano Lett.* **2002**, *2*, 647–650.

Chapter 4

Energetics of CNT bundling

The energetics of the bundling of CNTs has been explored. The Umbrella Sampling simulation technique has been applied to study free energy calculations of the bundling process. Two types of CNT bundling approaches have been consodered: parallel and perpendicular and the respective free energy changes are computed in monomer and trimer of polycarbonate matrices (both in monomer and trimer).

4.1 Introduction

In the last chapter it has been observed that CNTs form bundle when incorporated with high concentration (10%) in polycarbonate matrix. The mechanism of bundling also has been discussed in details. Then, naturally, the next impotant query that obviously comes in is the energetics of the bundling phenomena. Molecular dynamics (MD) provides us robust machinery to explore the energetics associated with a molecular process like self-assembly. To explore bundling energetics umbrella sampling which is one of the widely used techniques is applied to calculate free energy change.

Umbrella sampling simulations are used to determine the free energy change (ΔG) associated with an event along a reaction coordinate, ξ [1–3]. This technique is useful in determining the binding energies and macromolecular interactions [4–13]. By umbrella sampling, a biasing potential is added to the Hamiltonian of the system to improve the sampling of the conformational space which are insufficiently sampled. A series of configurations is generated along a reaction coordinate, ξ, between two interacting species one of which is considered as a reference and the other one is subjected to a biasing potential. The species under biasing potential takes up different positions with increasing centre of mass distance from the reference point. With the increasing centre of mass distances, few configurations are extracted which are called "sampling windows". Then for each window, independent simulation is performed to generate an ensemble of structures along the reaction coordinate. From each of this independent simulation, potential of mean force (PMF) is calculated and assembled over all the adjacent windows along the reaction coordinate by weighted histogram analysis method (WHAM) proposed by Kumar et. al. [14]. Gibb's free energy, ΔG is calculated from the PMF curve.

To find the energetics of the bundle formation, umbrella sampling has been performed on the CNTs in both monomer and trimer matrices. It is also interesting to investigate how binding energy between CNTs changes if we go from monomer to trimer matrix. We have taken two types of arrangements of CNTs in the mixture and prepared two separate sets of rectangular boxes. In one of the boxes, two CNTs are placed parallel to each other and in another one, they are placed in a perpendicular fashion. The centre of mass distance is kept approximately 0.8 nm. The aim

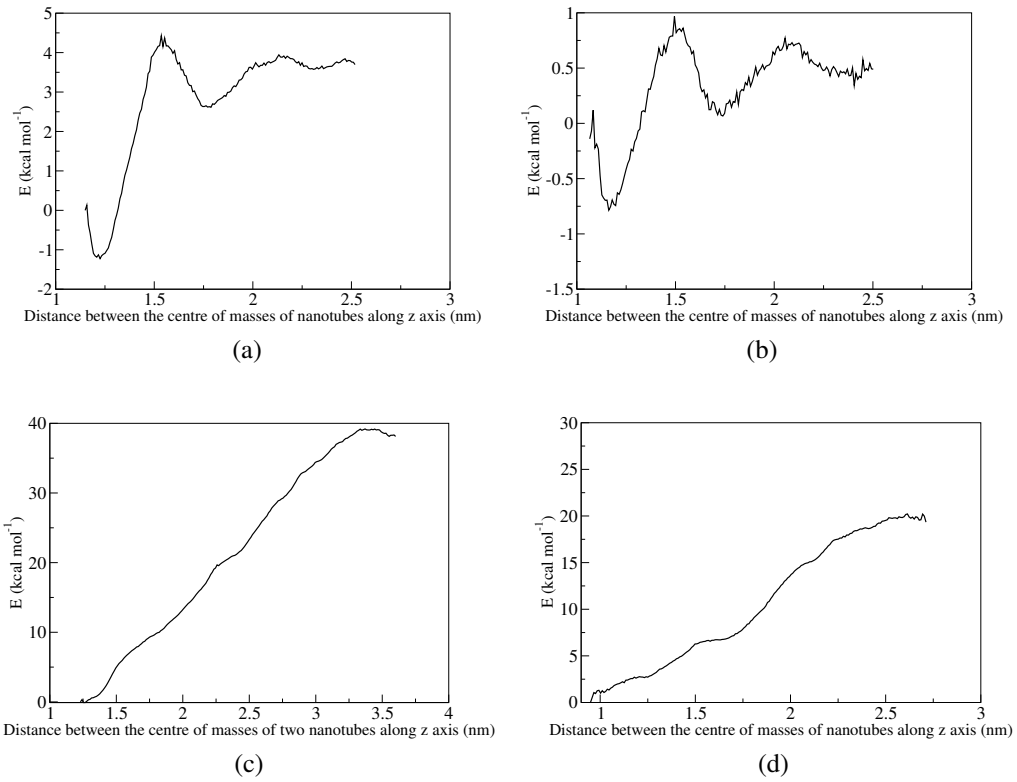

Figure 4.1: Potential of mean force (PMF) curves. (a) when pull is applied along z axis on one of the parallel aligned CNTs in monomer matrix., (b) when pull is applied along z axis on one of the perpendicularly aligned CNTs in monomer matrix., (c) when pull is applied along z axis on one of the parallelly aligned CNTs in trimer matrix., (d) when pull is applied along z axis on one of the perpendicularly aligned CNTs in trimer matrix.

of putting CNTs in two different conformations separately is to compare the corresponding free energy changes associated with two different types of approaches: parallel approach of one CNT to other one and the perpendicular approach of one to another in the composite. Each of the boxes is elongated along z axis as one of the CNTs is pulled along z-axis. Initially we have equilibrated the systems restraining two CNTs at their position for 10 ns for monomer matrix and 20 ns for trimer matrix at constant pressure (NPT) of 1 bar. The temperature is maintained at 500 K using Berendsen thermostat. All other parameters used are same as those used for CNT-monomer and CNT-trimer mixed systems described in simulation details section. The structures generated at the end of the equilibration are used as the starting configurations for pulling simulations.

The pulling simulation for each of the mixed systems (one with two parallel CNTs and another with two perpendicular CNTs) has been performed. One CNT is position-restrained and the other

Table 4.1: Binding free energies of CNTs from umbrella sampling in kcal mol^{-1}

System	Parallel	Perpendicular
monomer	-5.53	-1.72
trimer	-39.27	-20.10

one is pulled along z axis with restraints along x and y axes. For monomer matrices, each of the pulling simulations is carried out with a pull force constant 700 kJ mol^{-1} nm^{-2} and pull rate of 0.01 nm ps^{-1}. For trimer matrices, pull force constant is 600 kJ mol^{-1} nm^{-2} and pull rate is 0.01 nm ps^{-1}. The pull rates and pull force constants are optimized to get the best combination for the systems. For each system, one CNT is pulled away from restraining one along z axis over 0.5 ns. From these trajectories, 250 windows have been extracted. To choose the starting window, change in the centre of mass distances between two tubes along z axis are checked for each system. The starting window is selected from the region of coordinate where the centre of mass distance between the two CNTs has started increasing significantly and if in histogram of the configurations within the sampling windows, there is sufficient overlap between the starting and the immediate adjacent window. The last window for sampling is chosen until the plateau region in the potential of mean force (PMF) curve (Figure 4.1) has been achieved. For parallel tubes in monomer matrix, all the windows between 1.2-2.5 nm centre of mass distance are chosen and for perpendicular tubes, windows are chosen with a gap of approximately 0.1 nm centre of mass distance between 1.2-2.5 nm. In trimer system with parallel and perpendicular tubes, windows are selected between 1.3-3.4 nm and between 1.2-2.5 nm respectively keeping approximately 0.1 nm gap. Each of the windows has been subjected to 5 ns of MD run. Finally weighted histogram method (WHAM) [14] is applied to get the binding energies.

The potential of mean force (PMF) curves (Figure 4.1) are obtained for each of the systems by applying weighted histogram analysis method (WHAM) [14] on sampling windows for last 4.5 ns and free energy change (ΔG) for each system is calculated and summarized in Table 4.1. The difference between the minimum and maximum in PMF curve represents the free energy change for the process under consideration. In Figure 4.1, we have observed all the PMF plots have one maximum and one minimum points. In case of monomer matrices, we can observe there are

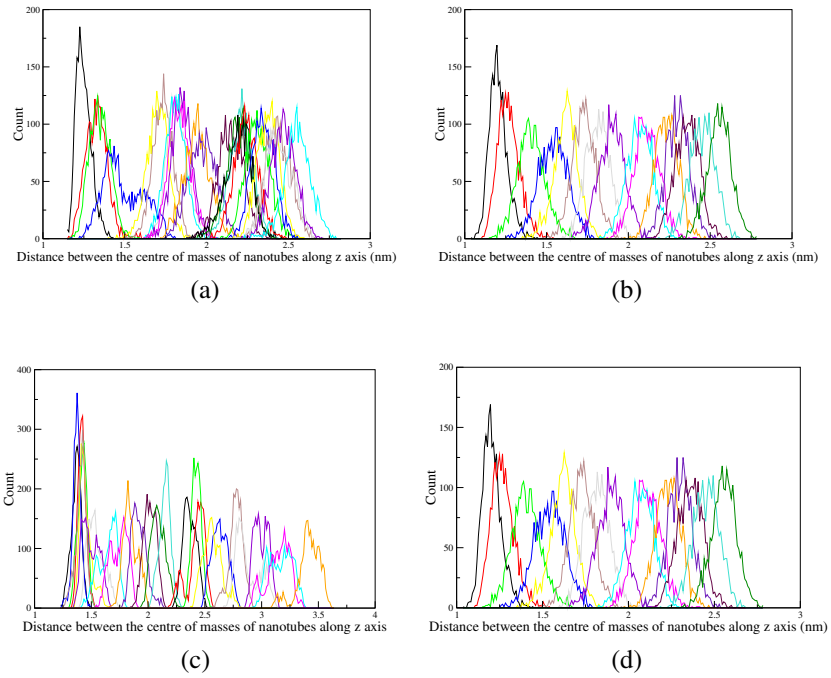

Figure 4.2: (a) Histogram of sampling windows of monomer matrix with parallel nanotubes., (b) Histogram of sampling windows of monomer matrix with perpendicular nanotubes., (c) Histogram of sampling windows of trimer matrix with parallel nanotubes., (d) Histogram of sampling windows of trimer matrix with perpendicular nanotubes.

some local minima exist in the energy landscape (Figure 4.1a, 4.1b). But for trimer matrices these local minima are not observed (Figure 4.1c, 4.1d). Histogram plots (Figure 4.2) show sufficient overlap between the adjacent windows. In monomer matrix, ΔG for parallel tubes (Figure 4.1a) is -5.53 kcal mol^{-1} and for perpendicular tubes (Figure 4.1b) it is -1.72 kcal mol^{-1}. In trimer system binding energy has increased significantly. ΔG for parallel tubes (Figure 4.1c) is -39.27 kcal mol^{-1} and for perpendicular tubes (Figure 4.1d) it is -20.10 kcal mol^{-1}.

From the umbrella sampling, the energetics associated with bundle formation mechanism for CNTs can be interpreted. Binding free energy is less for parallel alignment of nannotubes than perpendicular in both monomer and trimer matrices. Interestingly binding free energy decreased significantly when matrix is changed from monomer to trimer. Interaction between CNTs and matrix plays quite significant role in energetics of bundle formation. More polymeric solvent may enhance the binding energy hence bundle formation.

4.2 Conclusion

To explore the energetics of bundle formation, umbrella sampling technique has been used. Binding energy of CNT placed in parallel to each other is less than that of perpendicular orientation. Binding energies have been decreased from monomer to trimer mixture which indicates that polymerisation has a role to play in enhancement of binding energy. In future we can explore the binding energies for higher oligomeric units and also for different polymers for comparisons. The binding energies can be explored taking more number of CNTs and also for different aspect ratio and chirality. The tendency of CNTs to form bundles leads us to believe that there is a high probability of formation of percolation network between the bundles in the polymer matrix which can be explored with the help of multiscale modeling like coarse-graining which will be discussed in the next chapter.

References

[1] Patey, G. N.; Valleau, J. P. *Chem. Phys. Lett.* **1973**, *21*, 297.

[2] Torrie, G. M.; Valleau, J. P. *Chem. Phys. Lett.* **1974**, *28*, 578.

[3] Torrie, G. M.; Valleau, J. P. *J. Comput. Phys.* **1977**, *23*, 187.

[4] Karplus, M.; Bartels, C. *J. Phys. Chem. B* **1998**, *102*, 865–880.

[5] Bevan, D. R.; Lemkul, J. A. *J. Phys. Chem. B* **2010**, *114*, 1652–1660.

[6] Halperin, A.; Ermilov, V.; Lazutin, A. *Macromolecules* **2010**, *43*, 3511–3520.

[7] Gunsteren, W. F.; Beutler, T. C.; Bremi, T.; Ernst, R. R. *J. Phys. Chem.* **1996**, *100*, 2637–2645.

[8] Novak, B. R.; Moldovan, D.; Waldrop, G. L.; de Queiroz, M. S. *J. Phys. Chem. B* **2009**, *113*, 10097–10103.

[9] Maragakis, P.; van der Vaart, A.; Karplus, M. *J. Phys. Chem. B* **2009**, *113*, 4664–4673.

[10] Wolf, M. G.; Jongejan, J. A.; Laman, J. D.; de Leeuw, S. W. *J. Phys. Chem. B* **2008**, *112*, 13493–13498.

[11] Procacci, P.; Marsili, S.; Barducci, A.; Chelli, R.; Schettino, V. *J. Phys. Chem. B* **2006**, *110*, 14011–14013.

[12] Topf, M.; Richards, W. G. *J. Am. Chem. Soc.* **2004**, *126*, 14631–14641.

[13] Brady, J. W.; Schmidt, R. K.; Teo, B. *J. Phys. Chem.* **1995**, *99*, 11339–11343.

[14] Rosenberg, J. M.; Kumar, S.; Bouzida, D.; Swendsen, R. H.; Kollman, P. A. *J. Comput. Chem.* **1992**, *13*, 1011–1021.

Chapter 5

Mesoscale simulation of polycarbonate-CNT composite

Mesoscale simulation of polycarbonate-CNT composite is presented. Dissipative Particle Dynamics (DPD) has been performed to explore large scale morphology and dynamics of composite systems. The important target is to map the parameters required for DPD simulations from previously described all-atom simulations. So the Flory-Huggins theory is applied for necessary mapping procedure and interaction parameters for DPD simulation of polycarbonate-CNT composite have been calculated. The long range dynamics of bundles of CNTs is investigated by mean square displacement. The bundling size analysis is performed with different loadings of CNTs in polycarbonate.

5.1 Introduction

As already discussed in the 3rd chapter that polycarbonate and CNT-dispersed polycarbonate composites having attracted significant attentions among researchers are subjected to many experimental and theoretical studies [2–10]. The dispersion pattern of CNTs in the matrix, the interaction between polymer-CNT and CNT-CNT drive the extent of improvement of desired properties. Simulations have been used extensively to investigate the properties of polymers. Molecular dynamics (MD) and Monte Carlo (MC) methods are widely used techniques to study structure and dynamics of materials at atomistic level. These techniques can provide crucial insights about the nature of interactions between nanotubes and polymer, and help us to understand the dynamics, structural properties at great extent. But atomistic simulations are restricted in terms of length and time-scale [11–14]. Thus atomistic simulations of large polymer chains can not effectively sample the phase space for longer time and length-scale and thus, configurations often tend to confine at a local minimum energy. So observation of large scale change of morphology, phase transformations is difficult. Mesoscale simulation techniques can be used to overcome the length and time-scale restrictions and large number of particles can be simulated for much longer time to study equilibrium morphology and structural properties effectively [13]. Dissipative Particle Dynamics (DPD) has become quite popular recently as a mesoscopic simulation technique which has found large applications in various fields of materials. It has been used to study polymer-CNT composites [15–18], morphology of block co-polymers used in fuel cell [19], micelle formation [20–22], polymer viscosity [23], self-assembly of nanoparticles in polymer [24] etc. To apply DPD in polymer solutions and investigate the thermodynamics of mixing of different polymeric materials Groot and Warren [25] developed correlations between interaction potentials for DPD and Flory-Huggins theory of polymer solutions.

Polycarbonate is a versatile, transparent, and tough plastic material used for many applications in industry. It is a lightweight plastic material with quite admirable strength. This combination gives polycarbonate edge over other polymer materials in terms of applicability. Its uses include compact disks, eyeglasses, lenses, electronic devices, laptops, mobiles, automobile parts, outdoor fixtures, chemical and medical equipments etc. encompassing almost all manufacturing and engineering

fields. However, due to increasing demand of more efficient properties, pure polycarbonates are gradually becoming less competent to cope up with the challenge of ongoing demand. So CNT-reinforced polycarbonate composites have become more popular due to improved mechanical, thermal, and electrical properties. Pure polycarbonate is a poor electrical conductor. However, incorporation of small amount of CNT can enhance the conductivity by manifold [26–30]. This property of polycarbonate CNT composite has found essential applications in order to dissipate build-up charges in electronic equipments used in aircrafts, computers, cell phones, and various portable electronic devices [1, 31]. Thus it can be used as antistatic coating in the devices for this purpose. Polycarbonate-CNT composite can replace heavy metallic plates used in devices to reduce weight and cost significantly due to improved stiffness [32]. The electrical conductivity of composite depends upon the morphology of CNTs in the matrix [3]. The efficiency of the conduction depends on the extent of percolation network formed by the CNTs or nanofillers [26, 33, 34]. So percolation of CNT plays important role in enhancement of conducting properties of composite systems. Potschke et al.[3] investigated the electrical percolation network formation by multi-walled CNT in polycarbonate melt experimentally. The dispersability of CNTs under different melt processing conditions is studied by them. The agglomeration and network formation by nanotubes was observed and electrical percolation was studied by measuring conductivity using dielectric spectroscopy. They have shown that low pressing speed and high temperature enhance the agglomeration to form conductive percolation network. They have reported that the percolation threshold can be achieved in between 0.5 wt% and 5 wt% filler concentration for different kinds of multi-walled CNT. This experimental study of percolation of CNTs in polycarbonate propelled us to investigate percolation network, dynamics and distribution of aggregates of CNTs in polycarbonate matrix theoretically. Theoretical investigation can help to get deeper insight about the structure and dynamics of CNT in polymer matrix and produce important informations about percolation network.

Previously, as described in chapter 3, all atomistic MD simulation of monomer and trimer of polycarbonate and small length CNT composites was performed to understand the local structuring of monomer, dynamical properties of monomer, trimer and CNTs. Bundle formation phenomena

have been observed from the same atomistic MD simulations and mechanism of bundle formation was investigated. Binding free energy of nanotubes have also been calculated and reported in monomer and trimer matrices (in Chapter 4). In this chapter the mesoscopic simulations of CNT-polycarbonate composite will be discussed. To simulate polycarbonate-CNT composite at mesoscopic scale we have performed DPD simulations taking larger chain lengths of polymer and nanotube. For DPD simulation, interaction parameters have to be calculated for the system under investigation. In this work, we have calculated necessary parameter for our DPD simulation of polycarbonate-CNT composite from atomistic molecular dynamics simulation. The relationship between Flory-Huggins parameter and DPD repulsion parameter for CNT-polycarbonate composite has not been investigated before. So we have performed necessary calculations to establish the relationship between Flory-Huggins parameter and repulsion parameter for CNT-polycarbonate composite system. After parametrization, we have simulated composite systems consisting of large number of particles with different CNT concentrations (2%, 5%, 10%) to investigate dynamics of CNT in polymer matrix and bundle morphology in different concentrations. Mean square displacement of nanotubes is investigated to explore the confined dynamics in the polymer matrix. Then bundling of nanotube is studied at different filler content (2%, 5%, 10% CNT). Effect of bundling on the dynamics of CNTs in polycarbonate matrix is examined in different concentrations. In 10% mixture, percolation network is found to be formed by the nanotubes.

5.2 Computational Procedure

To calculate Flory-Huggins parameter from Hildebrand solubility parameter we have taken last 10 ns trajectory of atomistic simulation of pure monomer of polycarbonate at 500 K described in chapter 3. We have estimated molar volume of monocarbonate by summing up Van der Waals volume of each atom and molar enthalpy of vaporization (31.37 kJ/mol) from nonbonded energy for pure monomer system. Hildebrand solubility parameter (eq. 2.33) for monomer is estimated to be 9.86 $(J/cm^3)^{1/2}$. To calculate the solubility parameter of CNT, we have taken the CNT from atomistic simulation described in chapter 3. The molar enthalpy of vaporization of CNT is estimated by calculating nonbonded energy (16.88 kJ/mol) of CNT in a pure CNT system using GROMACS

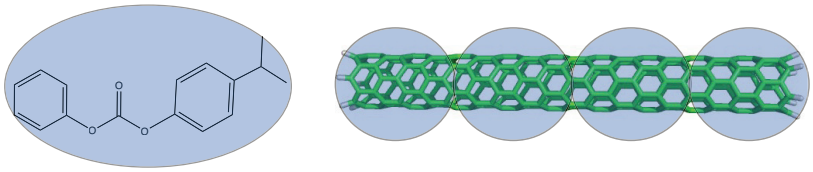

(a) (b)

Figure 5.1: (a) Structure of one monomer representing one mesoscale bead. (b) Structure of one CNT representing four mesoscale beads.

4.0.7 [37, 38]. The molar volume of CNT is calculated from its length and radius by considering it as a cylinder and adding up Van der Waals volume of nanotube atoms. The Hildebrand solubility parameter (eq 2.33) for CNT is found to be 3.58 $(J/cm^3)^{1/2}$ (Table 5.2). Flory-Huggins parameter (χ) is calculated as 7.7 from the solubility parameters obtained for monomer of polycarbonate and CNT according to the eq 2.32.

Maiti et al.[15] investigated the dispersion pattern of CNT (15,15) in PMMA (polymethylmethacrylate) by DPD simulation. For CNT-PMMA mixture, they have calculated Flory-Huggins χ parameter according to the eq 2.32. To compute excess interaction parameters (Δa) they have used the equation 2.31 for ρ=3 proposed by Groot and Warren [25] for monomer-monomer mixture. But we have established the relationship between Flory-Huggins χ parameter and Δa for our specific CNT-polycarbonate composite system. It is necessary because for our DPD simulation, one of the components is rigid (CNT) and the other one is flexible (polymer). This difference in flexibilities between the components can affect the extent of segregation in such composite systems. To get the relationship between the Flory-Huggins χ parameter and excess repulsion parameter (Δa) to be used for our DPD simulation of CNT-polycarbonate composite we have followed the procedure described by Groot and Warren [25]. We have coarse-grained the monomer of polycarbonate (Figure 5.1a) as one DPD bead (B) and the CNT (Figure 5.1b) as four DPD beads (A). It is because of the fact that volume of CNT is roughly four times of that of monomer in our atomistic simulations. Then we have prepared a system consisting of equal number of A and B types of beads (50%-50%). Molecule consisting of twelve beads is mapped for one CNT and the molecule consisting of three beads represents one polycarbonate (oligomer) chain. The box consists of 24000 beads and number density(ρ) is kept as 3. The bond length is taken as 0.5 dpd unit and bond constant (Harmonic

Hookean) as 100 k_BT for both of CNT and polymer. The angle and angle constant (Harmonic) for CNT are taken as 180° and 100 k_BT, respectively to incorporate rigidity in bending of nanotube. Maiti et al. [15] have used harmonic bond and angle potential with bond constant 20 k_BT and angle constant 40 k_BT, respectively to incorporate rigidity to CNT. However, they have mentioned that the values they have taken are 1-2 orders of magnitude smaller than the required values to introduce bending stiffness and Young's modulus of a real nanotube. To incorporate sufficient stiffness to CNT we have taken both bond and angle constant as 100 k_BT which is higher than the values Maiti et al. have used. Cut-off radius r_c is considered as 1.25 dpd unit. Interaction parameter (a_{ii}) for similar type of beads is kept 25 k_BT/r_c. Temperature parameter is taken as k_BT=1. Mass of each bead is 1 dpd unit of mass. The dpd unit of energy is k_BT. The friction constant γ is taken as 6.75 which is used by Groot and Warren [25] for polymer solution. Systems are subjected to mesoscopic simulation with NVT ensemble using DL_MESO 2.5 [36] and force is calculated by integrating with velocity Verlet algorithm. According to Groot and Warren [25], the relationship between Flory-Huggins χ parameter and ϕ_A can be found from the eq 2.30. Groot and Warren [25] also proposed the method to get relation between Flory-Huggins χ parameter and Δa in their paper and we have adopted that protocol. To get the relationship between Flory-Huggins χ parameter and Δa, partial density of A is calculated against the axis of the box along which phase segregation has taken place. To calculate ϕ_A we have simulated the system for differnt Δa values. Repulsion parameter for similar beads (a_{ii}) is taken as 25 k_BT/r_c and a_{ij} is varied to vary Δa. Timestep is chosen to be 0.02τ. The simulations are performed for 2×10^6 steps. Then partial densities of A are estimated for different Δa values. Then we have estimated Flory-Huggins parameter by calculating ϕ_A by averaging over last 32000-40000 τ considering the homogeneous region in density profile of A. The relationship between the Flory-Huggins parameter and Δa is linear as shown in (Figure 5.2). After fitting straight line to it we get the relation

$$\chi = 0.028\,\Delta a\,(r_c/k_BT) + 0.45 \tag{5.1}$$

From this equation we have calculated Δa by computing Flory-Huggins parameter obtained from atomistic simulation. The χ value obtained from atomistic simulation is 7.7. As χ value is quite larger than the intercept value, we have ignored the intercept part. The Δa value is found to be 275 k_BT/r_c.

Table 5.1: System Information

System	Number of beads per chain	2%	5%	10%
Polycarbonate	60	4083 chains	3958 chains	3750 chains
Carbon Nanotube	20	250 chains	625 chains	1250 chains

Table 5.2: Hildebrand Solubility Parameter and Molar Volume for CNT and Monocarbonate from Atomistic Simulation

System	Bead	solubility parameter $(J/cm^3)^{1/2}$	molecular volume ($Å^3$)
CNT	A	3.58	2175.94
Monocarbonate	B	9.86	536.38

Now to simulate systems of 2%, 5% and 10% loading with CNTs of much higher length, a single nanotube is represented by 20 beads. As polymer is generally much longer in length than nanotube, so we have constructed the polymer with 60 beads. Repulsion parameter for similar beads (a_{ii}) is 25 k_BT/r_c and Δa is taken as 275 k_BT/r_c. Systems are simulated (NVT ensemble) for 2×10^6 steps with timestep 0.02τ. All other parameters are kept same as mentioned above. The total system size (total number of beads) in each case (2%, 5%, 10%) is taken as one fourth of a million which is large enough to explore morphology of the components. Detailed information about the systems is given in Table 5.1.

Mesoscale simulation is advantageous over classical MD because it can cross the barrier of length and time-scale restrictions applied to classical MD. It is important to get an idea about the real length and time-scale of DPD simulation. Schemes have been developed to represent DPD length and time units in terms of real length and time units [39, 40]. Taking informations from our atomistic simulation we can convert the DPD unit of length and time to real units of length and time. The cut-off radius r_c is related to the volume of a bead by the relation[15, 39], $r_c = (\rho\ V_b)^{1/3}$ where ρ=3, and V_b=536 $Å^3$ which is the volume of monomer of polycarbonate in our atomistic simulation[35]. This leads to r_c = 1.17 nm. In our DPD simulation, the length of the cubic simulation box is 43.67 in DPD unit. Thus, the real spatial dimension represented by the side of the box is $\sim$ 51 nm. Groot and Rabone [39] proposed a relation between DPD unit of time and real time by comparing diffusion rate of water beads with that of experimental values. The DPD unit of

time τ is given by $\tau \sim 25.7\ N_m^{5/3}$ [40] where N_m is the number of water molecules corresponding to one DPD bead. In our DPD simulation, each bead corresponds to $\sim$18 (N_m) water molecules. This yields $\tau \sim 3177.2$ ps and the time-step 0.02 τ is found to be 63.5 ps in real time. The DPD simulations are performed for 2×10^6 steps. So our total simulation run corresponds to a real time of $\sim 127\ \mu$s.

5.3 Results and Discussion

The bundle formation of CNTs in composite was observed in atomistic simulation study (Chapter 3)[35]. In this chapter we will discuss DPD simulation of polycarbonate-CNT composite with different concentrations of CNT taking much larger chain of polymer and longer nanotubes aiming to study bundling morphology of CNT at meso-scale regime. The morphologies of nanotubes in equilibrated 2%, 5%, and 10% mixtures are depicted in Figure 5.3a, 5.3b, and 5.3c, respectively. In 2% mixture, we can see that nanotubes form many small aggregates which are dispersed in a discrete fashion all over the matrix. Nanotubes are found to form small bundles by aligning in parallel fashion. In 5% mixture, relatively larger aggregates are formed than that in 2% mixture. From snapshot (Figure 5.3b) it can be observed that apart from parallel orientations few nanotubes perpendicularly orient themselves in big aggregates. However, in 10% mixture, the nanotubes are found to aggregate in a very interesting fashion. Figure 5.3c shows that bundles of nanotubes have formed long striped percolation morphology. To explore the dynamics of nanotubes during bundle formation we have studied diffusivity of nanotubes at different time regimes by plotting mean square displacement. Then bundle size of nanotubes in different concentrations is evaluated to understand the relative bundling affinity in different nanotube concentrations.

5.3.1 Mean Square Displacements

In 10% mixture of CNT-monocarbonate solution, bundling formation phenomenon was observed by atomistic MD simulation (described in Chapter 3). Mean square displacement (MSD) of nanotubes was also investigated. MSDs are found to be quite non-linear because of the presence of

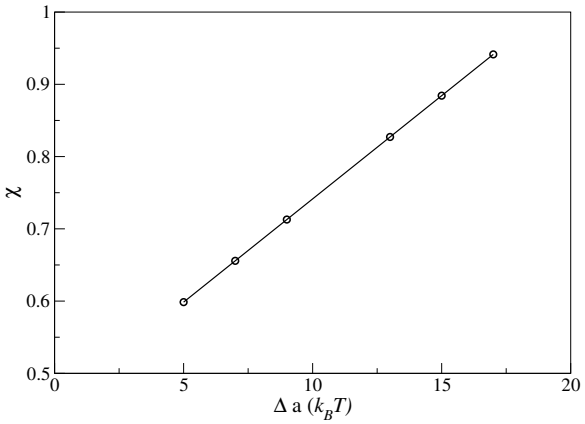

Figure 5.2: Plot of χ vs. Δa.

significant confinement created by polymer chains. Here, in DPD simulation we have taken significantly large nanotube (20 beads) and much bigger polymer chain (60 beads). 2%, 5%, and 10% nanotube-polymer mixture are prepared and equilibrated for 2×10^6 steps. In DPD simulations of all of three types of mixtures, bundle formation of nanotubes is observed (figure 5.3) which indicates high tendency of bundling of nanotubes even in small concentrations. Confined dynamics of nanotubes in highly flexible polymer matrix with whom nanotube interacts repulsively leads to the formation of bundles. As beads in DPD interact via soft interaction potential, entanglement of polymer is not present and has no effect on the dynamics of nanotubes. Once nanotubes form bundles their movement in the matrix is expected to become more restricted and thus diffusivity should decrease. So to investigate how diffusivity get affected gradually as the bundle formation takes place MSDs of nanotubes are plotted at regular intervals. MSDs are plotted at an interval of 4000 τ (τ is time in DPD unit) of the trajectory for three types (2%, 5%, 10%) of mixtures.

Figure 5.4a shows the mean square displacements of nanotubes for 2% mixture at each 4000 τ interval. For first 4000 τ nanotubes are diffusing faster than later time intervals. This means that initially when nanotubes are completely dispersed in the matrix their diffusivity is quite high and as they come closer to due high cohesive energy their diffusivity get lowered as time of simulation increases. Within MSD plot of first time interval we can see diffusion of nanotube is faster at the very beginning of simulation. In the initial 800 τ, MSD is quite steeper (steep slope) and eventually get decreased as the time increases in simulation. In case of 5% mixture (figure 5.4b), slope of the MSD plot for first 4000 dpd time is quite high similar to the case for 2% mixture and after initial

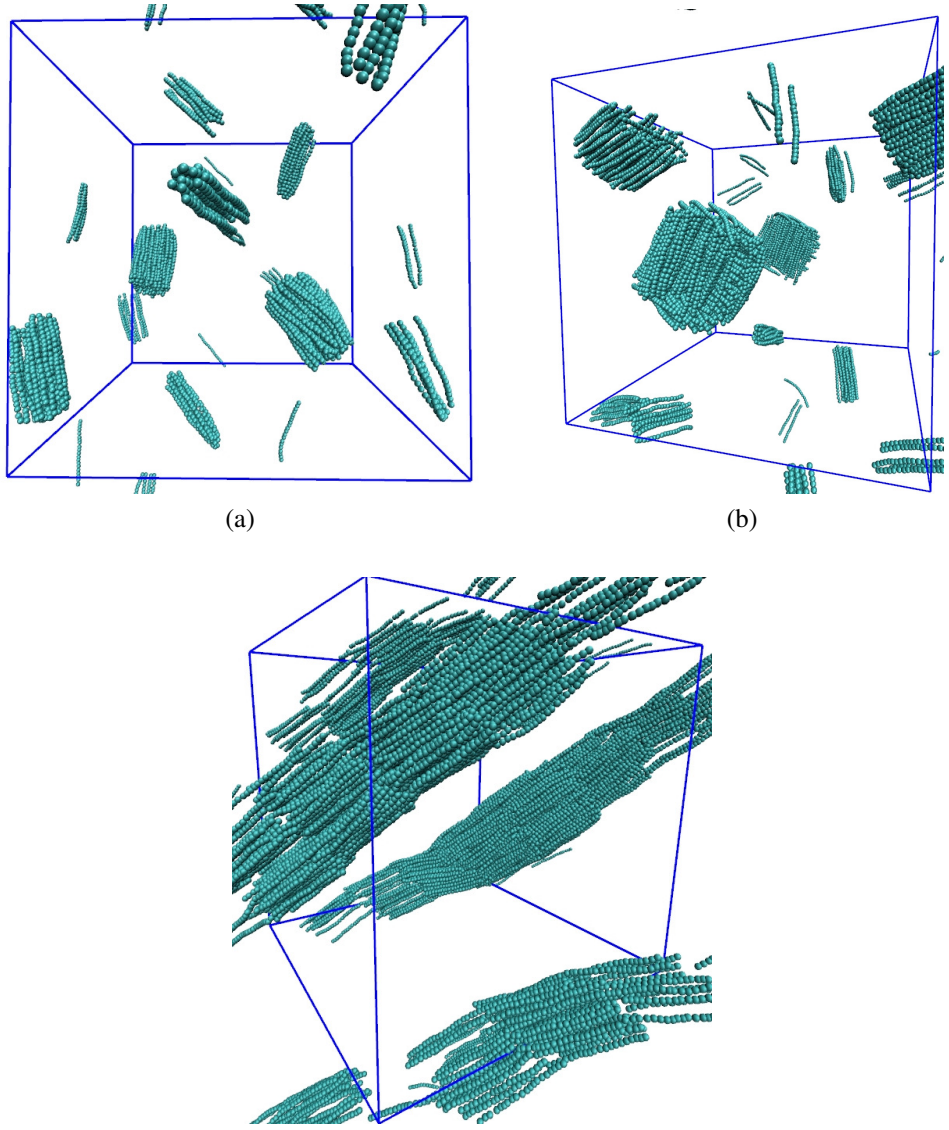

Figure 5.3: (a) Snapshot of a equilibrated 2% mixture showing bundles of nanotubes. (b) Snapshot of a equilibrated 5% mixture. (c) Snapshot of a equilibrated 10% mixture showing percolation network formation by nanotubes. Polymer is not shown for clarity.

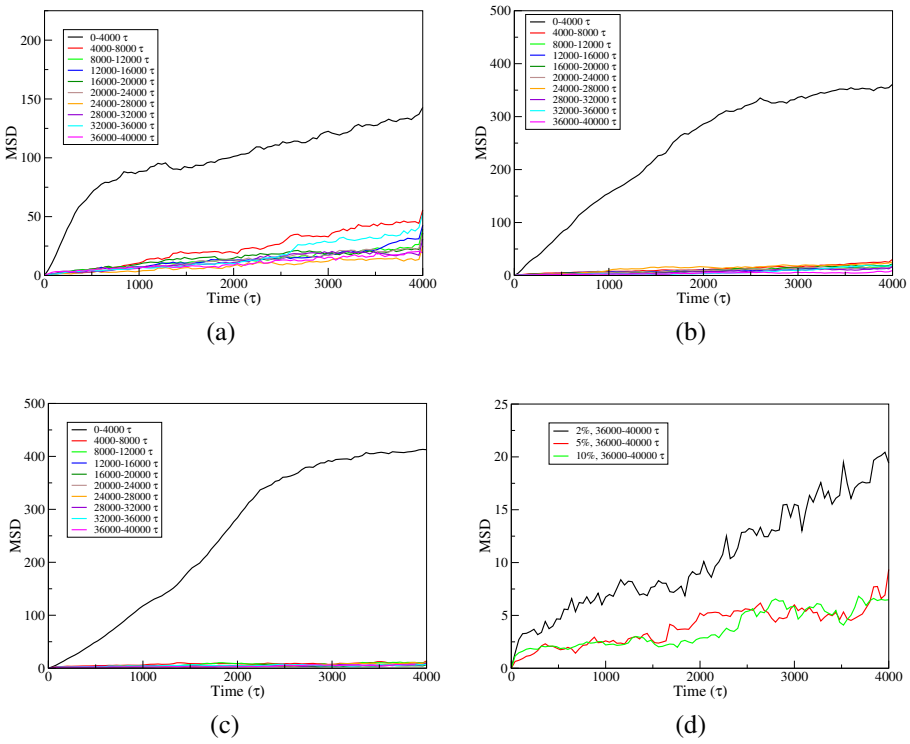

Figure 5.4: (a) MSD plots of nanotube for 2% mixture. (b) MSD plots of nanotube for 5% mixture. (c) MSD plots of nanotube for 10% mixture. (d) MSD plots of nanotube for 2%, 5%, 10% mixture for last 4000 τ.

4000 τ slope of MSD drops to a large extent indicating loss of diffusivity of nanotubes due to bundling. With respect to 2% mixture, the diffusivity at later parts of simulation time intervals is quite low for 5% mixture. For 10% mixture (Figure 5.4c) almost similar trend is observed as for 5% mixture. The slopes of MSDs become almost zero for 10% mixture as the equilibration is achieved. This indicates that once nanotubes get bundled they become almost static with little scope for diffusion.

To get an idea how concentration of nanotube affects the diffusivity we have plotted MSDs for last 4000 τ of trajectory of three different mixtues (Figure 5.4d). It shows that diffusivity of nanotube is relatively higher for small concentration (2%) and as concentration increases diffusivity decreases. For 5% and 10% mixtures, there is no marked difference in the diffusivity of nanotubes once equilibration is achieved and most of the nanotubes get bundled.

5.3.2 Bundle Size Analysis

Nanotubes are found to form bundles in all 2%, 5% and 10% mixtures with different bundle sizes. So investigation of bundle size distribution is important as it can help us to understand the effect of concentration on the extent of bundle formation. To estimate bundle size, the distances among the center of masses of nanotubes is calculated. Then, those nanotubes which are coming within a cut-off distance are considered to form a single bundle. From the distance distribution of center of masses of nanotubes calculated for last 100 frames of trajectory of 10% mixture (as 10% mixture contains maximum number of nanotubes) the minimum of the first peak is obtained at 1.5 dpd unit of length. So the cut-off distance is taken as 1.5 dpd unit of length. The number of occurrences of bundle size is computed and plotted as a function of bundle size. The high probability of formation of a particular bundle size is indicated by the high value of occurrence. Figure 5.5a, 5.5b, and 5.5c show the bundle size distribution in 2%, 5%, and 10% mixtures respectively. To explore the evolution of bundle size as simulation time proceeds, distributions are calculated with an interval of 4000 τ for last 20000 τ from the trajectories.

In case of 2% mixture (Figure 5.5a), the size of bundle varies from 3 to 52 with many highly probable numbers coming between them at different time intervals. Bundles formed with small

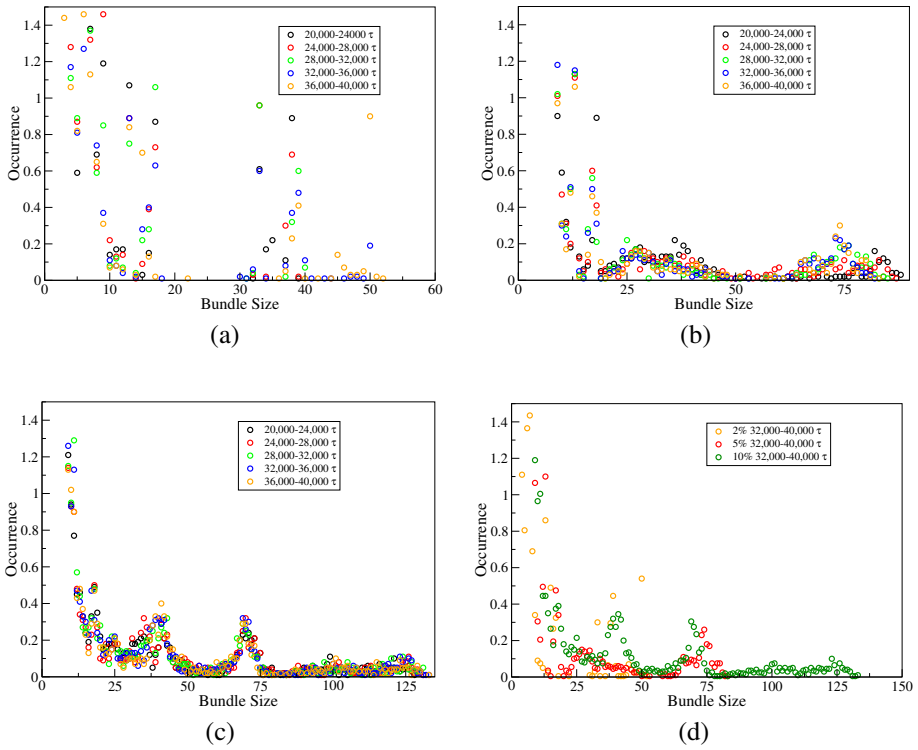

Figure 5.5: (a) Bundle size distributions of nanotubes for 2% mixture at different time intervals. (b) Bundle size distributions of nanotubes for 5% mixture at different time intervals. (c) Bundle size distributions of nanotubes for 10% mixture at different time intervals. (d) Bundle size distributions of nanotubes for 2%, 5%, 10% mixtures calculated for last 8000 τ.

number of nanotubes (less than 20) is highly probable. However, big bundles are found to be abundant with sizes between 30 and 50. Distribution plots for 32000-36000 τ and 36000-40000 τ show significant probability to form bundles with 50 nanotubes. For 5% mixture (Figure 5.5b), probable size of small bundles varies between 8 and 18. Relatively bigger bundles are formed with the sizes varying between 25 to 35. Among larger bundles, the most probable size of bundles is found to be around 74. Thus bundle size is definitely increased from 2% mixture to 5% mixture. With increasing number of nanotubes the tendency of agglomeration gets enhanced as more number of nanotubes interact to create more favorable environment of bundle formation. 10% mixture has the maximum loading of nanotubes among three mixtures and thus, nanotubes are expected to form bigger bundles than both of 2% and 5% mixtures. Figure 5.5a, 5.5b, and 5.5c show that the range of bundle size has indeed increased as concentration of nanotubes get increased from 2% to 10%. For 2% mixture the maximum bundle size is found to be 52. 5% and 10% mixtures have maximum sizes of 87 and 133 respectively. For 10% mixture (Figure 5.5c) small bundles with high probability are formed with 8 to 25 nanotubes, little bigger bundles have 30-40 nanotubes. A high probability of forming bundles is found with the size of 70 and the probability remains almost intact for last 20000 τ. This indicates at high concentration once a maximum bundle size is attained in equilibrated system it tends to remain intact. Thus equilibrium morphology is attained very fast.

For 5% and 10% mixtures small bundles are having almost same range of sizes with highest probability and the maximum number of nanotubes in highly probable bundles is found to be around 70-75. To get a clear idea how bundle size in equilibrated systems varies with nanotube concentration we have plotted bundle distribution (Figure 5.5d) of nanotube for 2%, 5%, and 10% mixtures taking last 8000 τ of trajectory. Peaks in the distribution plots show that for 2%, 5% and 10% mixtures there is a high probability of forming big bundles with a number of nanotubes of 50, 74 and 69 nanotubes respectively. For 10% mixture, another probable bundle size is found to be around 122 and smaller bundles have formed in abundance with size 40. 5% mixture have highly probable big bundles with around 74 nanotubes and smaller bundles contain around 9-30 nanotubes. 2% mixture has high probability at 50 along with 32 to 38.

Figure 5.3a, 5.3b, and 5.3c show equilibrium morphologies of the bundles of nanotube formed

in 2%, 5%, and 10% mixture respectively. These snapshots clearly indicate that the tendency of forming big bundles increases with nanotube concentration. In 2% mixture (Figure 5.3a) the nanotubes are observed to form small bundles by aligning parallely among themselves. The bundles are dispersed all over the matrix. Small bundles can diffuse in the matrix also. And as bundles size grows with concentration the diffusivity of bundles diminishes. That can be reason for decrease in nanotube diffusion when matrix is loaded with higher loading of nanotubes. For 5% mixture (Figure 5.3b) the bundles formed are bigger in size compared to 2% mixture and bundle size calculation also conforms that. In case of 10% mixture (Figure 5.3c), nanotubes are found to assemble parallely and form long stripes like morphology which confirms that the percolating network is formed. The long stripes formed are also found to align parallel to each other. Thus, in 10% mixture nanotubes have acquired suitable environment which led them to form percolation network and it is also above the percolation threshold.

5.4 Conclusions

In this chapter, DPD simulations performed on polycarbonate-CNT composite systems with different nanotube concentrations to investigate the equilibrium morphology of nanotubes and their dynamics in composite matrix are described. From atomistic simulations necessary parameter for DPD simualtion is calculated. 2%, 5%, and 10% mixtures of CNT-polycarbonate are prepared with polymer chain much lengthier than the nanotube. This study investigates the dynamics by plotting mean square displacements at different time intervals for each of the mixtures for comparison. From MSD it can be inferred that diffusivity of nanotubes decreases as bundle formation takes place. Also diffusivity of nanotubes in equilibrated matrices are found to decrease from lower to higher concentration of nanotubes. In all of the three mixtures (2%, 5%, and 10%) bundle formation of nanotubes is observed. However, the size of the bundles in equilibrium systems are found to be dependent upon concentration of nanotubes. Bundle size analysis shows that nanotubes tend to form bigger bundles in higher concentrations. Investigating the morphology in 10% mixture, percolation pathway formed by nanotubes is found out. However, in 2% and 5% mixtures percolation network is not observed. So 10% of nanotube concentration can be assumed to be close

to threshold filler concentration to form percolating pathway in polycarbonate matrix without any external perturbations. The future work will comprise the study of the formation of percolation morphology for varying length of CNT and polymer chains below the mixing ratios of percolation threshold.

References

[1] Potschke, P.; Fornes, T. D.; Paul, D. R. *Polymer* **2002**, *43*, 3247–3255.

[2] Zhao, Q.; Wood, J. R.; Wagner, H. D. *J. Polym. Sci., Part B: Polym. Phys.* **2001**, *39*, 1492–1495.

[3] Pegel, S.; Potschke, P.; Petzold, G.; Alig, I.; Dudkin, S. M.; Lellinger, D. *Polymer* **2008**, *49*, 974 – 984.

[4] Potschke, P.; Pegel, S.; Villmow, T.; Stoyan, D.; Heinrich, G. *Polymer* **2009**, *50*, 2123–2132.

[5] Ruoff, R. S.; Ding, W.; Eitan, A.; Fisher, F. T.; Chen, X.; Dikin, D. A.; Andrews, R.; Brinson, L. C.; Schadler, L. S. *Nano Lett.* **2003**, *3*, 1593–1597.

[6] Argon, A. S.; Hutnik, M.; Suter, U. W. *Macromolecules* **1991**, *24*, 5970–5979.

[7] Meyer, H.; Hahn, O.; Müller-Plathe, F. *J. Phys. Chem. B* **1999**, *103*, 10591–10598.

[8] Müller-Plathe, F.; Hahn, O.; Mooney, D. A.; Kremer, K. *J. Chem. Phys.* **1999**, *111*, 6061.

[9] Kremer, K.; Delle Site, L.; van der Vegt, N.; Leon, S. *Macromolecules* **2005**, *38*, 8078–8092.

[10] Eilhard, J.; Zirkel, A.; Tschop, W.; Hahn, O.; Kremer, K.; Scharpf, O.; Richter, D.; Buchenau, U. *J. Chem. Phys.* **1999**, *110*, 1819–1830.

[11] Frenkel, D.; Smit, B. *Understanding Molecular Simulation*, 2nd ed.; Academic Press, Inc.: Orlando, FL, USA, 2001.

[12] Allen, M. P.; Tildesley, D. J. *Computer simulation of liquids*; Clarendon Press: New York, NY, USA, 1987.

[13] Müller-Plathe, F. *ChemPhysChem* **2002**, *3*, 754–769.

[14] Nieminen, R. M. *J. Phys.: Condens. Matter.* **2002**, *14*, 2859.

[15] Maiti, A.; Wescott, J.; Kung, P. *Mol. Simulat.* **2005**, *31*, 143–149.

[16] Maiti, A.; Wescott, J.; Goldbeck-Wood, G. *Int. J. Nanotechnology* **2005**, *2*, 198–214.

[17] Wang, Y.-C.; Ju, S.-P.; Cheng, H.-Z.; Lu, J.-M.; Wang, H.-H. *J. Phys. Chem. C* **2010**, *114*, 3376–3384.

[18] Wang, Y.-C.; Ju, S.-P.; Huang, T. J.; Wang, H.-H. *Nanoscale Res. Lett.* **2011**, *6*, 433.

[19] Roy, S.; Markova, D.; Kumar, A.; Klapper, M.; Müller-Plathe, F. *Macromolecules* **2009**, *42*, 841–848.

[20] Cui, Y.; Zhong, C.; Xia, J. *Macromol. Rapid Comm.* **2006**, *27*, 1437–1441.

[21] Fraser, B.; Denniston, C.; Müser, M. H. *J. Chem. Phys.* **2006**, *124*, 104902.

[22] Li, X.; Deng, M.; Liu, Y.; Liang, H. *J. Phys. Chem. B* **2008**, *112*, 14762–14765.

[23] Fedosov, D. A.; Karniadakis, G. E.; Caswell, B. *J. Chem. Phys.* **2010**, *132*, 144103.

[24] Liu, D.; Zhong, C. *Macromol. Rapid Comm.* **2006**, *27*, 458–462.

[25] Groot, R. D.; Warren, P. B. *J. Chem. Phys.* **1997**, *107*, 4423–4435.

[26] Potschke, P.; Dudkin, S. M.; Alig, I. *Polymer* **2003**, *44*, 5023 – 5030.

[27] Coleman, J. N.; Curran, S.; Dalton, A. B.; Davey, A. P.; McCarthy, B.; Blau, W.; Barklie, R. C. *Phys. Rev. B* **1998**, *58*, R7492–R7495.

[28] Alig, I.; Skipa, T.; Lellinger, D.; Potschke, P. *Polymer* **2008**, *49*, 3524 – 3532.

[29] Andrews, R.; Jacques, D.; Minot, M.; Rantell, T. *Macromol. Mater. Eng.* **2002**, *287*, 395–403.

[30] Jiang, X.; Bin, Y.; Matsuo, M. *Polymer* **2005**, *46*, 7418 – 7424.

[31] Pisanova, E. *Wiley Encyclopedia of Composites*; John Wiley and Sons, Inc., 2011.

[32] Singh, S.; Pei, Y.; Miller, R.; Sundararajan, P. *Adv. Funct. Mater.* **2003**, *13*, 868–872.

[33] Potschke, P.; Bhattacharyya, A. R.; Janke, A. *Eur. Polym. J.* **2004**, *40*, 137 – 148.

[34] Kumar, S.; Lively, B.; Sun, L.; Li, B.; Zhong, W. *Carbon* **2010**, *48*, 3846 – 3857.

[35] Chakraborty, S.; Roy, S. *J. Phys. Chem. B* **2012**, *116*, 3083–3091.

[36] Seaton, M. A.; Anderson, R. L.; Sebastian, M.; William, S. *Mol. Simulat.* **2013**, *39*, 796–821.

[37] Van Der Spoel, D.; Lindahl, E.; Hess, B.; Groenhof, G. *J. Comput. Chem.* **2005**, *26*, 1701–1718.

[38] Hess, B.; Kutzner, C.; van der Spoel, D.; Lindahl, E. *J. Chem. Theory Comput.* **2008**, *4*, 435–447.

[39] Groot, R.; Rabone, K. *Biophys. J* **2001**, *81*, 725 – 736.

[40] Groot, R. D. *J. Chem. Phys.* **2003**, *118*, 11265–11277.

Chapter 6

Self-assembly of nanorods in diblock copolymer matrix

Dissipative particle dynamics simulations are performed on model systems of nanorod and diblock copolymer composite to understand the dynamics, structure, and morphology of self-assembled bundles of nanorods in gyroid phase. The nanorods are given preferential enthalpic interaction with minority component of diblock copolymer by increasing repulsion with majority component, so that nanorods tend to self-assemble and settle inside the confined contours of minority component aimimg to explore the relative size and shape of the self-assembled bundles under confining locations within the matrix. Also the structural details of bundles are explored as a function of nanorod flexibility.

6.1 Introduction

In the preceding chapter, the bundling of nanotubes in polycarbonate matrices has been discussed. The assembly of nanotubes under confinement can be another interesting aspect of explorations. Instead of taking homopolymer, diblock copolymer can be considered as matrix in which incorporated nanorods can form assemblies under the confinement created by phase separation of diblock copolymer matrix. In this chapter this study is going to be discussed.

Diblock copolymer composites have attracted significant attention due to the potential applications in the field of material science and nanotechnogy.[1–7] Diblock copolymer undergoes microphase separation below order-disorder transition temparature to form lamellar, gyroid, cylindrical, cubic phases depending on the composition and segregation strength between the components. The spatial distribution of nanoparticles and nanorods doped in diblock copolymer matrix can be directed by the microphase separation of block copolymers. Thus, microphase separation of diblock copolymer can be used advantageously to tailor the properties of composite.The doped matrials can be subjected to occupy specific locations of diblock copolymer matrix according to the specific aim to improve properties. The mechanical stability, electrical conductivity, and optical performance of composites are sensitive to the specific location of the 3-D organization of doped materials within the polymer matrix.[1, 8] The doped nanofillers, on the other hand, can influence and alter the morphology of microdomains of block copolymer.[4, 9–13]

Many experimental,[8, 10, 14, 15] theoretical,[9, 16, 17] and computational studies[3, 11, 18–20] on the block copolymer-spherical nanoparticle have been pursued. These studies suggest that the spatial distribution of nanofillers in the block copolymer matrix is dictated by thermodynamics i.e. the complex interplay between enthalpy and entropy in the system. The enthalpy part depends on the chemical nature of nanofillers and block copolymer components, and their relative enthalpic affinities toward each other in the system. The entropy has two major contributing parts: translational entropy (in case of nanoparticles), and configurational entropy of polymer chain. By controlling the shape, size, and chemical nature of nanoparticles this interplay can be tuned and manipulated for desired applications. However, nanorods, due their higher aspect ratio, can be

more effective than spherical nanoparticles in providing superior mechanical, and optical properties for nanocomposite material when incorporated with the same volume fraction of spherical nanoparticles.[3, 21] Buxton *et al.* have investigated the reinforcement eficiency of fillers in increasing mechanical strength of polymer with three different types of filler shapes: spherical, rod-like, and platelet. Their study have shown that platelet and rod shaped fillers induce more stiffness to polymer matrix compared to spherical particles.[21] Another crucial advantage is that nanorods, due to their shape anisotropy, have higher tendency to form percolation network than that of spherical nanoparticles.[22, 23] Recently, the study of block copolymer-nanorod composite has become quite important. Zhang *et al.* have experimentally investigated the behaviours of CdSe nanorods in PS-*b*-PMMA diblock copolymer templates: one is lamellar nanoscopic channels and the other one is cylindrical pores. They have shown that the location and orientation of nanorods can be controlled by manipulating the nanorod dimensions with respect to the channel or pore width.[23] Beneut *et al.* [24] studied the morphology of magnetic iron oxide nanorods doped in lamellar phase of nonionic surfactant. They have found that the orientation of nanorods gets modified under the influence of magnetic field and so is the texture of lamellar phase. Lamellar phase have induced an attractive interaction between the nanorods and aggregates have been found to be formed in more concentrated lamellar phase having more stronger confinement effect. However, similar behaviour was not observed in case of spherical nanoparticles emphasizing the role of the particle shape in the interplay of interaction between doped particle and polymer. He *et al.* have performed Dissipative Particle Dynamics (DPD) simulation to investigate the reorientations and phase transitions of symmetric diblock copolymer-nanorod nanocomposites subjected to steady shear flow. Their study has shown that the final morphology of nanocomposite is highly regulated by the interplay between nanorod and diblock copolymer under shear. The spatial distribution of nanorods can change the phase of the diblock copolymer.[3]

Most of the studies concerning the nanofillers doped in block copolymer phases discussed before deal with lamellar or cylindrical microdomains formed by the phase separation of block copolymers. Studies on the nanofillers incorporated in gyroid phase of block copolymer is relatively elusive. Recently, Li *et al.* have investigated the spatial arrangements of metal nanoparticles in the gyroid phase formed by triblock terpolymer matrix experimentally. According to them gyroid phase

has potential to form next-generation mesoporous network superstructure. By doping gyroid domains with nanofiller, the effective potential applicability in the field of catalysis can be enhanced. [1] Thus, gyroid structure can be used as a *template* for many important applications. Gyroid phase has curved interfacial surface providing confinements throughout the matrix and thus, it can regulate the shape and sizes of self-assmebled nanofillers doped in it. Nanorods can also be of different flexibilities. The morphology of the bundles can be regulated by the relative bending tendency of the nanorods. So it is important to investigate and explore the morphology, structural and dynamical properties of nanorods in gyroid phase of block copolymer as function of different nanorod flexibilities and nanorod-diblock copolymer interactions. Coarse-grain simulation can effectively represent the morphology of self-assembled nanofillers in polymer composites as it considers larger length-scale and longer time-scale compared to the all-atom simulation.[25–27] DPD is a particle based coarse-grained simulation technique that is widely used to study mesoscopic properties of various systems like polymer composites,[26–30] lipid bilayers,[31, 32] vesicle,[33, 34] morphology of block copolymer in fuel cell,[35] micelles[36–38] etc. Previously, we have investigated the stuctural, dynamical, and thermodynamical properties of self-assembly of carbon nanotubes (CNT) in polycarbonate (PC) matrix by all-atom molecular dynamics simulation,[39] and then the morphology and dynamics of CNT bundles in PC with DPD simulation.[27] Here, we have studied the morphology of nanorods of different flexibilities and different affinities toward the components of diblock copolymer by Dissipative Particle Dynamics (DPD) method. For this we have performed simulations on model systems of nanorod-diblock copolymer composite. The flexibility is varied by varying angle constant (k_θ) of nanorods, and relative affinity of nanorods toward blocks of the copolymer is varied by considering different repulsive interaction between them. The nanorods are observed to self-assemble to form bundles of different shapes and sizes depending on the nanorod flexibilities and nanorod-polymer interactions. We have studied the shape anisotropy and radius of gyration of nanorod bundles situated at interfacial confined locations or in confined minority component domains as a function of nanorod flexibility and nanorod-block copolymer miscibility.

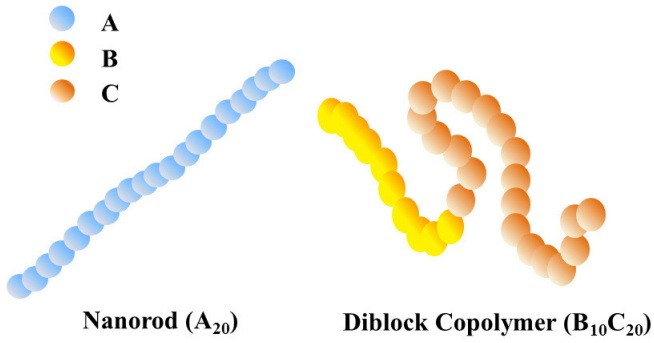

Figure 6.1: Schematic representation of nanorod and diblock copolymer

6.2 Simulation Details

The simulation box consists of approximately 2×10^5 beads, and the number density(ρ) is kept as 3. The equilibrium bond length is taken as 1.0 dpd unit and bond constant (Harmonic Hookean) as 100 k_BT for both of the nanorods and diblock copolymer to impose the connectedness of the adjacent beads in a chain. The bond potential is given by

$$U_r = \frac{k_b}{2}(r - r_0)^2 \tag{6.1}$$

where U_r is the bond potential, k_b is the bond constant, and r_0 is the equilibrium bond length. The bending flexibility depends on the bond angle constant, k_θ of the nanorod. The angle potential used in the study is given by

$$U_\theta = \frac{k_\theta}{2}(\theta - \theta_0)^2 \tag{6.2}$$

where U_θ is the angle potential, k_θ is the angle constant, and θ_0 is the equilibrium bond angle. Higher k_θ means increased bending rigidity. We have noted that in our DPD simulations nanorods show bending flexibility with k_θ=10 k_BT, and sufficient bending rigidity with k_θ=100 k_BT acquiring almost linear morphology. The range of this k_θ values is also in the range of the repulsive interactions (a_{ij}) by which nanorod and diblock copolymer are considered to have been interacting in this study. Thus, the equilibrium bond angle of nanorods is taken as 180° and the angle constant (Hookean), k_θ is taken as 10, 50, and 100 k_BT, respectively to vary rigidity in bending of nanorods. Cut-off radius R_c is considered as 1.0 dpd unit. The repulsion parameter between two dissimilar

type of beads *i* and *j* a_{ij} in eq 6.4 is related to the Flory-Huggins χ parameter by:[40]

$$a_{ii}\rho = 75k_BT \tag{6.3}$$

$$a_{ij} \approx a_{ii} + 3.27\chi_{ij}\ (\rho = 3) \tag{6.4}$$

where a_{ii} represents the repulsion parameter between similar type of beads. Temperature parameter is taken as k_BT=1. Mass of each bead is 1 dpd unit of mass. The dpd unit of energy is k_BT. Timestep is chosen as 0.04 τ, and the total number of timestep is 2×10^6. Thus, the total simulation time is $8 \times 10^4\ \tau$. The whole trajectory is saved in 1000 frames where each frame corresponds to 80 τ. Friction parameter γ is set to 4.5 giving noise strength σ as 3 according to the equation 2.26. Systems are subjected to mesoscopic simulation with NVT ensemble using the package DL_MESO 2.5 [41] and force is calculated by integrating with velocity verlet algorithm. We have simulated systems with 2 wt% loading with nanorods each of which is represented by 20 A beads, and diblock copolymer is represented as $B_{10}C_{20}$ where B and C beads are minority and majority components, respectively (schematically represented in Figure 6.1). Repulsion parameter between same type of beads is kept a_{ii}=25 k_BT, B and C components of diblock copolymer interact via repulsion parameter a_{BC}=40 k_BT.[42] The relative length of the minority B block with respect to the total length of diblock copolymer chain i.e. f=0.33 which is an acceptable value for gyroid phase formation within the Flory-Huggins segregation parameter regime of formation of gyroid morphology in the phase diagram.[43] Nanostructure formed by diblock copolymer by DPD simulation can be studied by structure factor.[44] To confirm that gyroid phase is formed, structure factor *S*(*k*) is calculated for pure $B_{10}C_{20}$ melt with a_{BC}=40 k_BT (Figure 6.4):

$$S(k) = \rho_M(k)\rho_M(-k)/N_M, \tag{6.5}$$

$$\rho_M(k) = \sum_{i=1}^{N} exp(ik \cdot r) \tag{6.6}$$

where N_M and $\rho_M(k)$ represents particle number and particle density for *M* type of beads, respectively in reciprocal space. For systems with nanorod doping, we have kept a_{BC}=40 k_BT fixed to keep the gyroid morphology of diblock copolymer matrix. To vary the repulsive interaction between nanorod and majority component C, a_{AC} is taken as 50, 60, 70, and 100 k_BT, respectively keeping other parameters constant. By this way, the nanorods are made to locate favorably in minority B component domains.

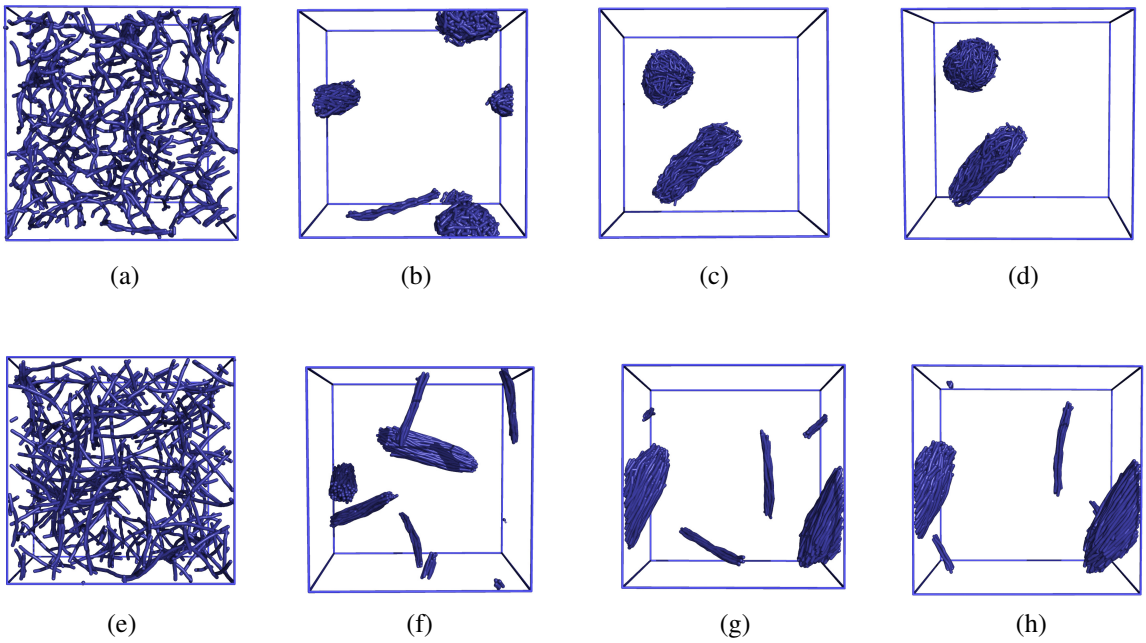

Figure 6.2: a), b), c), d) depict the snapshots of nanorods at 0 τ, 8000 τ, 40000 τ, and 80000 τ, respectively for a_{AC}=50 k_BT and k$_\theta$=10. e), f), g), h) depict the snapshots of nanorods at 0 τ, 8000 τ, 40000 τ, and 80000 τ, respectively for a_{AC}=50 k_BT and k$_\theta$=100.

6.3 Results and Discussion

6.3.1 Self-assembly of nanorods

Figure 6.2 depicts the time evolution of self-assembly of nanorods in the diblock copolymer matrix. Both the nanorods and diblock copolymer start evolving from random structures. The snapshots of nanorod self-assembly are extracted from 0 τ, 8000 τ, 40000 τ, and 80000 τ, respectively for two sets: one with a_{AC}=50, k$_\theta$=10, and the other one with a_{AC}=50, k$_\theta$=100. Nanorods are observed to self-assemble within a short timespan. Initially, nanorods self-assemble to form smaller aggregates (Figure 6.2b, 6.2f) at different locations in the matrix. Then smaller aggregates coalesce to form bigger bundles (Figure 6.2c, 6.2g). The bundles, once formed, remain morphologically intact for the rest of the simulation time. Also, the location of the bundles in the matrix does not change significantly. With the evolution of gyroid phase, the nanorods, which have favorable interaction with minority phase B, tend to self-assemble in the confined spaces occupied by B phase of the matrix

provided by $B_{10}C_{20}$ diblock copolymer. The bundles reside in energetically favorable confined locations and, as the diffusion through majority C component is energetically unfavorable, nanorod bundles avoid to diffuse across C phase. This observation is confirmed by plotting mean square displacement (MSD) of the centre of mass of nanorods from the initial random orientation to the end the trajectory (Figure 6.3) for all simulations under study. In Figure 6.3, MSDs demonstrate that the nanorods are diffusing very fast initially and, once they get self-assembled, the diffusion is almost arrested, and thus, MSD is not changing much with time. The self-assembly of nanorods in gyroid phase is observed to be feasible in short temporal span, and the bundles settled at energetically favorable confined contours provided by gyroid symmetry are dynamically arrested and thus, the merging of different bundles is a highly unlikely phenomenon. The difference in MSD plots has been observed for different a_{AC} values. It may be because of the fact that bundle dynamics is guided by the combined effect of nanorod-diblock copolymer interaction and local confinements created by gyroid symmetry. Nanorod bundles settle at different confining places in gyroid phase which, in turn, affects their dynamics.

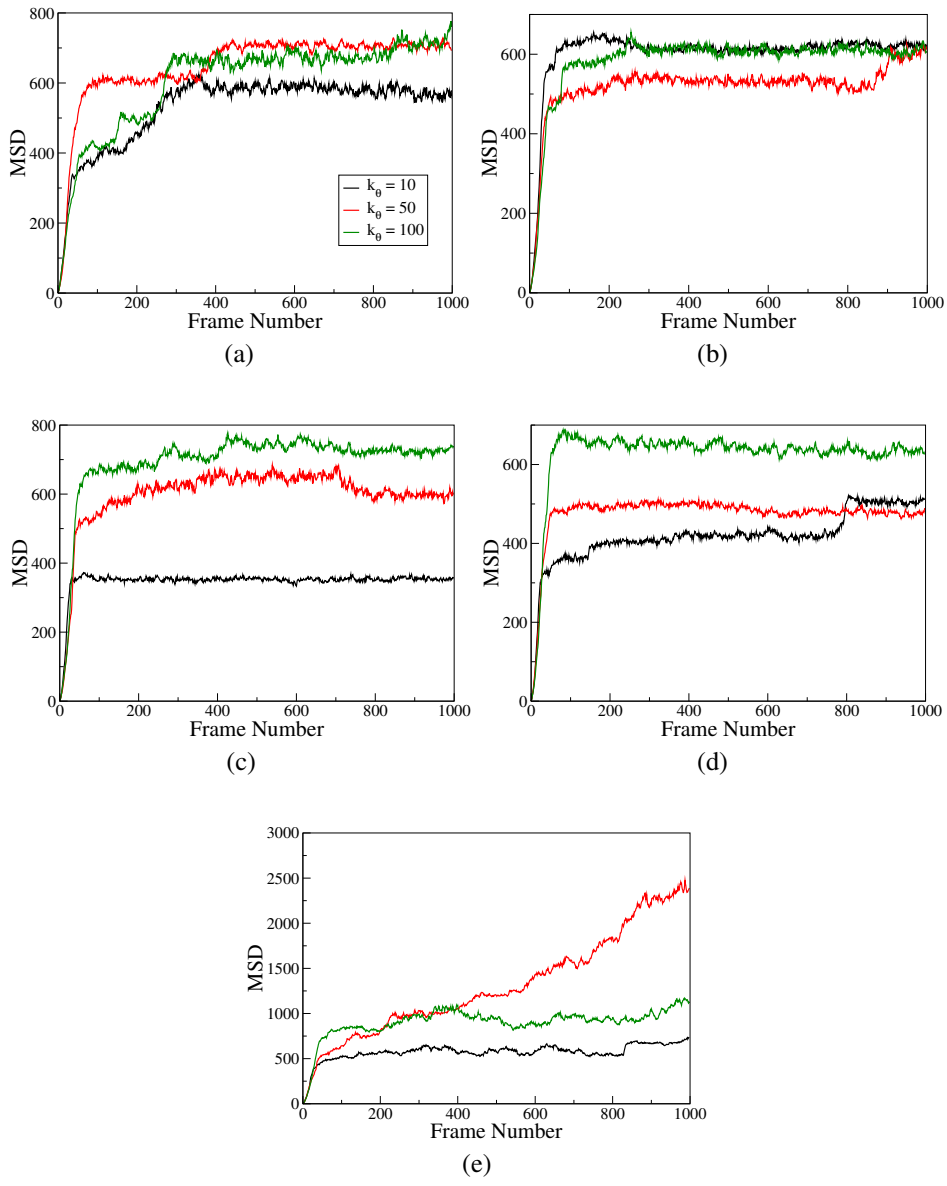

Figure 6.3: Mean square displacement of centre of mass of nanorods (A_{20}) for 0 τ to 80000 τ. a) a_{AC}=50 k_BT, b) a_{AC}=60 k_BT, c) a_{AC}=70 k_BT, d) a_{AC}=100 k_BT, e) nanorods in homopolymer (D_{30}) melt with a_{AD}=40 k_BT.

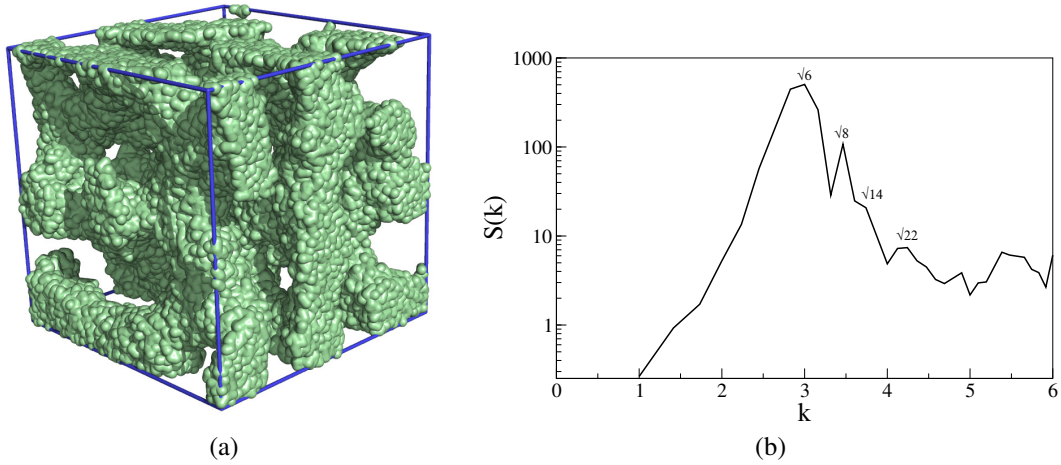

(a) (b)

Figure 6.4: a) Snapshot of gyroid morphology formed by pure $B_{10}C_{20}$ showing only B phase. b) Structure factor $S(k)$ of gyroid phase.

Now, to get an idea whether bundle formation dynamics is assisted by the formation of gyroid phase we have performed DPD simulations with 2 wt% nanorods (A_{20}) in homopolymeric (D_{30}) melt with different nanorod bending flexibilities (k_θ=10, k_θ=50, and k_θ=100). Repulsion parameters are taken as a_{AA}=a_{DD}=25, a_{AD}=40. Homopolymer does not undergo phase separation like block copolymer and thus the phase separation dynamics is absent in homopolymeric matrix doped with nanorods. Nanorods are found to form bundles in homopolymer matrices also. To compare the dynamics of bundle formation with diblock copolymer matrices MSD of centre of masses of nanorods is plotted for whole time-span of the trajectory (Figure 6.3e). Similar to the nanorod diffusion in diblock copolymer matrices, in case of homopolymer matrix also we observed from MSD pattern that the diffusivity of nanorods falls off after 50-70 frames (4000 τ-5600 τ) and this observation suggests that bundle formation dynamics in homopolymeric melt is as fast as in case of initial stages of phase separation of diblock copolymer matrices. The bundle formation happens faster than phase separation of diblock copolymer and apparently, it is not influenced by the initial thermodynamics of phase separation.

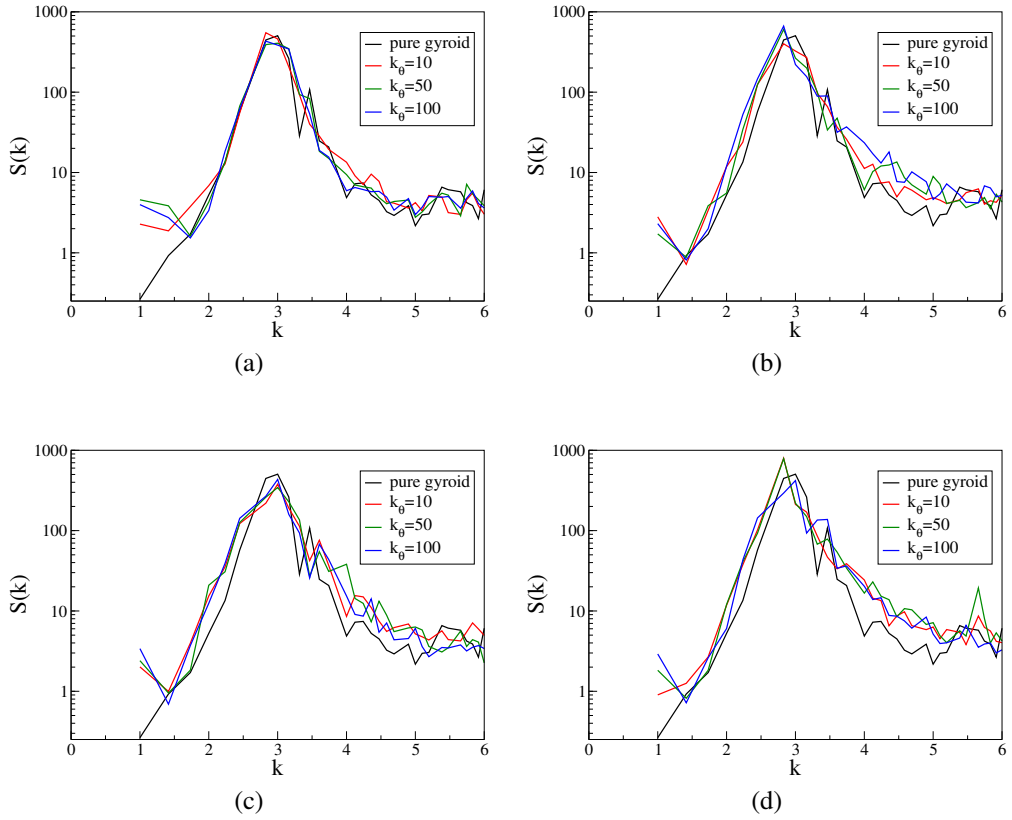

Figure 6.5: Structure factors for gyroid phase with 2 wt% doping with nanorods. a) a_{AC}=50 k_BT, b) a_{AC}=60 k_BT, c) a_{AC}=70 k_BT, d) a_{AC}=100 k_BT.

Table 6.1: Radius of gyration (R_g^2) and relative shape anisotropy (κ^2) of the nanorod bundles

k_θ	a_{AC}	R_g^2(Spherical)	R_g^2(Elongated)	κ^2(Spherical)	κ^2(Elongated)
10	50	25.08±0.18	32.96±0.74	0.010±0.006	0.59±0.01
	60	31.55±0.34	30.80±0.70	0.034±0.012	0.77±0.01
	70	22.79±0.32	33.96±0.99	0.039±0.014	0.54±0.02
	100	23.46±0.34	31.35±1.08, 31.05±0.61	0.048±0.014	0.71±0.01, 0.76±0.02
50	50	-	53.22±0.76	-	0.52±0.010
	60	-	44.33±0.54	-	0.61±0.008
	70	-	48.28±0.56, 35.59±0.36	-	0.58±0.007, 0.82±0.003
	100	-	44.27±0.54, 39.39±0.54	-	0.62±0.007, 0.72±0.006
100	50	-	53.12±0.60	-	0.56±0.007
	60	-	47.11±0.48, 37.88±0.38	-	0.60±0.007, 0.78±0.004
	70	-	54.70±0.61	-	0.54±0.008
	100	-	55.12±0.85	-	0.54±0.010

Table 6.2: Order parameters (S) for nanorods

k_θ	a_{AC}	Spherical	Elongated
10	50	0.003±0.007	0.816±0.055
	60	0.029±0.014	0.939±0.021
	70	0.025±0.015	0.801±0.031
	100	0.032±0.017	0.903±0.035, 0.927±0.026
50	50	-	0.615±0.073
	60	-	0.955±0.004
	70	-	0.950±0.004, 0.974±0.003
	100	-	0.947±0.060, 0.965±0.004
100	50	-	0.602±0.090
	60	-	0.964±0.003, 0.976±0.003
	70	-	0.958±0.002
	100	-	0.956±0.003

6.3.2 Structural properties

When only pure $B_{10}C_{20}$ diblock copolymer is simulated with interaction parameters $a_{BB} = a_{CC}$=25, and a_{BC}=40 it forms gyroid phase (Figure 6.4a). The corresponding structure factor[45] *S*(*k*) is calculated for simulated morphology, and is given in Figure 6.4b. The relative position of the peaks is consistent with the ratios expected for gyroid morphology [43, 46], and matches with experimental SAXS pattern.[47] *S*(*k*) is calculated by averaging over last fifty frames of equilibration trajectory. The doped nanofillers can influence the microphase of block copolymer. [1, 9–13] Yeh *et al.* have observed the transformation of block copolymer structure from hexagonal packed cylinder into a lamellar structure when CdS nanoparticles were doped (7%) in it.[13] The structure also get further altered with higher loading (28%) of CdS nanoparticles. They have shown that peak positions in SAXS curves for pure block copolymer change with the incorporation of CdS nanoparicles. Li *et al.* have also demonstrated that position of SAXS peaks shifted from neat gyroid phase to Au nanoparticle incorporated block copolymer composite.[1] In our study we also observed that when the gyroid phase matrix is doped with 2% by weight with different flexibilities and of different affinities toward one of the diblock copolymer phases the pure gyroid phase *S*(*k*) gets changed due to the perturbation created by nanorods incorporated (Figure 6.5). For all sets of a_{AC} values with doped nanorods, plots of *S*(*k*) are given with *S*(*k*) obtained for pure gyroid phase to observe the extent of perturbation. The pure gyroid morphology does not exist when doped with nanorods. As we have used very low amount of loading (2 wt%) of nanorods in our study, the phase transformation is not prominent as reflected in *S*(*k*) patterns which do not change at large extent from the pure gyroid phase. However, increase in nanorod doping can alter the gyroid phase. To check that, we have performed a simulation with 10 wt% nanorod loading with a_{AC}=50 and k_θ=100. *S*(*k*) plot (Figure 6.8) for this 10 wt% doped system suggests that the gyroid phase is significantly affected.

Nanorods of different flexibilities and affinities for gyroid phases are observed to form bundles of different shapes and sizes. The shape of the bundles is characterized by the shape anisotropy, κ^2, and the relative size of the bundles is depicted by the radius of gyration, R_g^2.[48, 49] For a ideally spherically shaped bundle κ^2=0, whereas for a perfectly linear shape κ^2=1. Radius of gyration increases with the increase in size of the bundles. The shape anisotropy κ^2 and radius of gyration

R_g^2 are obtained by calculating gyration tensor S_{mn}.[50] The m-n component of gyration tensor is given by:

$$S_{mn} = \left(\frac{1}{N}\right) \sum_{l=1}^{N} (S_{ml} - S_m^{CM})(S_{nl} - S_n^{CM}) \tag{6.7}$$

where S_m^{CM} denotes the centre of mass of each bundle in coordinate *m*, and *m* represents *x*, *y*, or *z*. *N* is the total number of beads under consideration in each bundle. After diagonalization of this gyration matrix, the eigenvalues can be obtained as λ_x^2, λ_y^2, and λ_z^2, respectively. The radius of gyration is given by:

$$R_g^2 = \lambda_x^2 + \lambda_y^2 + \lambda_z^2 \tag{6.8}$$

and the relative shape anisotropy κ^2 can be calculated as:[49]

$$\kappa^2 = \left(\frac{3}{2}\right) \frac{\lambda_x^4 + \lambda_y^4 + \lambda_z^4}{(\lambda_x^2 + \lambda_y^2 + \lambda_z^2)^2} - \left(\frac{1}{2}\right) \tag{6.9}$$

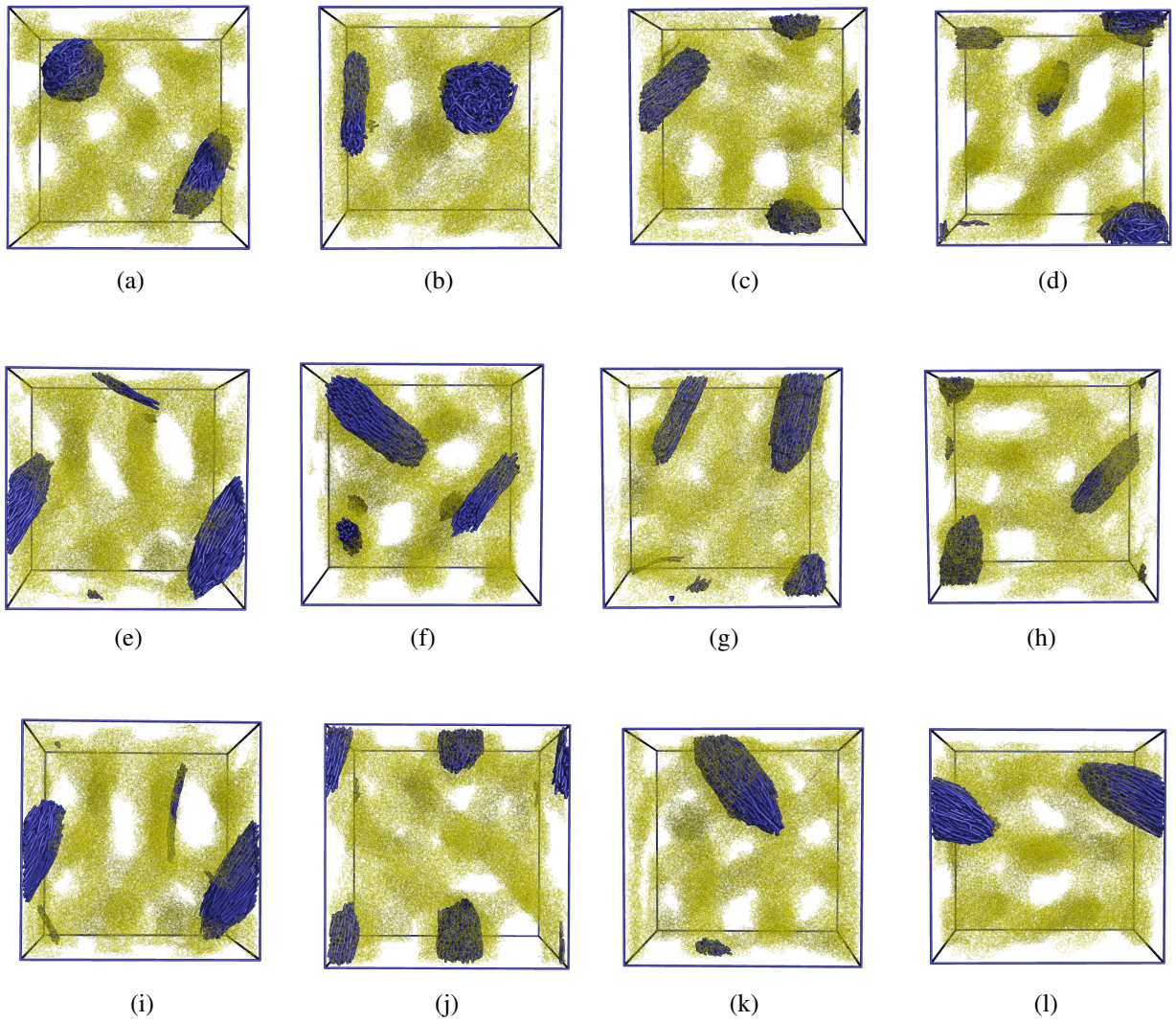

Figure 6.6: Snapshots of final morphologies of nanorod bundles (blue) with B component (yellow) of $B_{10}C_{20}$ copolymer. a), b), c), d) depict the snapshots for k_θ=10 and a_{AC} of 50, 60, 70, and 100 k_BT, respectively. e), f), g), h) depict the snapshots for k_θ=50 and a_{AC} of 50, 60, 70, and 100 k_BT, respectively. i), j), k), l) depict the snapshots for k_θ=100 and a_{AC} of 50, 60, 70, and 100 k_BT, respectively.

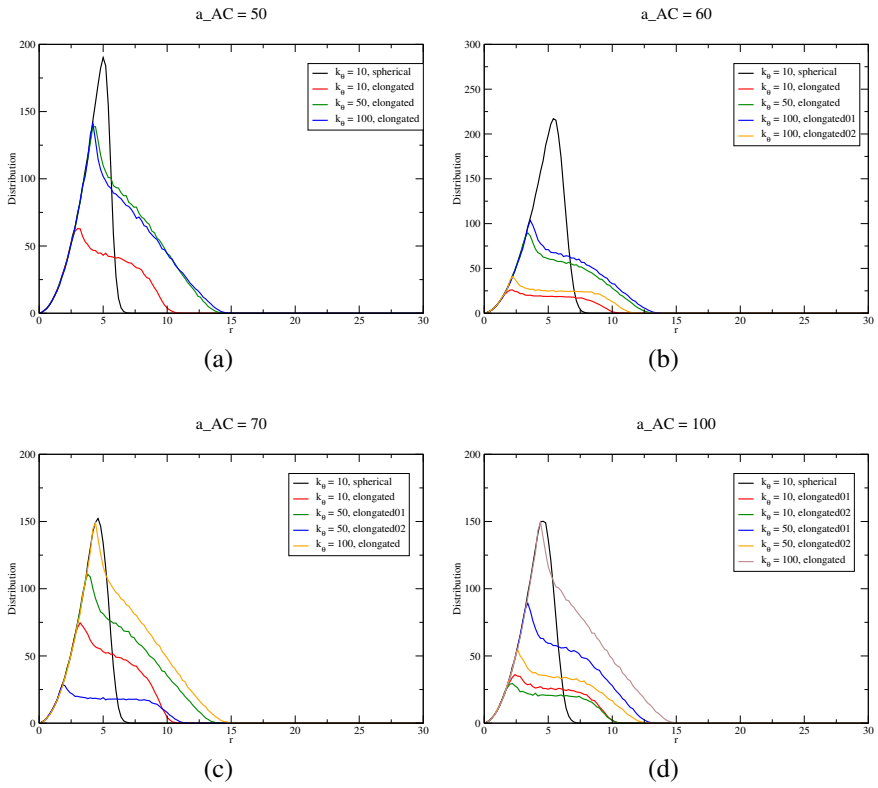

Figure 6.7: Distance distribution between centre of mass of a bundle and the beads corresponding to that bundle for systems with repulsion parameters **(a)** a_{AC} = 50 **(b)** a_{AC} = 60 **(c)** a_{AC} = 70 **(d)** a_{AC} = 100.

To calculate R_g^2 and κ^2 we have considered the centre of mass (COM) of the bundle and the beads in the bundle which are away from the centre of mass beyond a certain cutoff distance. To decide the cutoff for each individual bundle, at first, we plotted the distance distribution between bundle COM and the beads in that particular bundle (Figure 6.7). Then the cutoff is calculated by taking one dpd unit of length less than the value of the position of first peak. By doing this we ignored some core beads near the COM to represent shape anisotropy and radius of gyration of nanorod bundles by calculating gyration tensors. R_g^2 and κ^2 are calculated by averaging over the last 100 frames of equilibrated trajectory. Table 6.1 represents the radius of gyration and shape anisotropy of the bundles for all the systems under study. Also, the degree of ordering of nanorods of different bending flexibilities is studied by calculating order parameter (*S*) defined by:

$$S = \left(\frac{1}{2}\right)\langle 3cos^2\phi - 1\rangle \tag{6.10}$$

where ϕ is the angle between each pair of nanorod end to end vectors. For elongated bundles where nanorods are aligned parallely, the order parameter should be close to 1. For spherical bundles, due to the isotropic directional arrangements of nanorods, order parameter is expected to be close to 0. Order parameters averaged over last 100 frames of equilibration run are given in Table 6.2. All the final equilibrium morphologies of nanorod bundles with minority B phase of diblock copolymer are depicted in Figure 6.6. For very flexible nanorods (k_θ=10) both spherical and elongated bundles are observed to be formed (Figure 6.6a, 6.6b, 6.6c, 6.6d) for a_{AC} of 50,60,70 and 100 k_BT, respectively. The R_g^2 values (in dpd unit of length) for spherical bundles vary between 22.8 and 31.5, and all κ^2 values are close to zero. In this case of flexible nanorods, the size of the spherical bundles are found to be less or comparable with the elongated ones for all a_{AC} values. For a_{AC}=50,a_{AC}=70 and a_{AC}=100, sizes of the spherical bundles are less than elongated bundles as reflected by the R_g^2 values. In case of a_{AC}=60, sizes of the spherical and elongated bundles are comparable. The order parameters for nanorods in case of spherical bundles are close to zero (Table 6.2) which suggests that nanorods are isotropically oriented in spherical bundles. The sizes of the elongated bundles are found to fall between 30.8 and 33.9 in case of flexible nanorods (k_θ=10). The shape anisotropy κ^2 varies between 0.54 and 0.77. The elongated bundles have more ordered nanorods as the order parameter values are in between 0.8 and 0.92. For flexible nanorods, we have observed both spherical and elongated bundles for all cases of a_{AC} values i.e. the relative enthalpic

repulsion of nanorods with C phase. As the nanorods have favorable interaction with minority B phase of diblock copolymer they tend to settle inside confined columnar channels of B phase. As in gyroid phase, minority component provides different extent of confinement (minority phase in gyroid symmetry forms *nodes* and *struts* in its 3D structure[1]), the different shape of the bundles may be the result of that confinement effect within matrix, and regulated by the locations in the minor phase where the bundles reside. When the nanorods are less flexible i.e. k_θ=50, only elongated bundles are observed to form (Figure 6.6e, 6.6f, 6.6g, 6.6h). The size of the bundles are found to be increased, and R_g^2 varies between 44.2 and 53.2 (Table 6.1). κ^2 value ranges from 0.52 to 0.82 for all the a_{AC} values with this bending rigidity. Also, order parameter value ranges from 0.61 to 0.97 for all a_{AC}. This indicates that with more bending rigidity the orderness of nanorod alignment gets increased. In case of highly rigid nanorods (k_θ=100) bundles of elongated shapes are formed (Figure 6.6i, 6.6j, 6.6k, 6.6l). R_g^2 varies between 37.8 and 55.1, and κ^2 is found to fall between 0.54 and 0.78. It is observed that R_g^2 values do not change monotonically with the increase in a_{AC}. It may be due to the effect of the different degree of confinement along with different interfacial interaction present at the location where corresponding bundles reside. The order parameter value ranges from 0.60 to 0.97. The ordering of rigid nanorods is relatively more pronounced for all a_{AC} values. We have observed, in case of relatively rigid nanorods (k_θ=50, 100), no spherical bundles are found to form in the block copolymer matrix irrespective of the nanorod's increasing repulsive interaction with C phase of diblock copolymer. In elongated bundles, *oval* shaped elongated bundles have κ^2 in between 0.5 and 0.6 (this type of bundle shape is predominantly observable). But also *rod-like* bundles (e.g. in case of k_θ=10, and a_{AC}=60, 100 or k_θ=50, and a_{AC}=70, 100) have been found along with spherical or *oval* bundles. These *rod-like* bundles are having κ^2 values in between 0.70 and 0.82 with high degree of ordering. In case of less flexible nanorods it may be the fact that rather than governed by the probable confinement effect created by minority B phase (where nanorods are likely to be settled), the shape of the bundles is decided by the rigidity of the nanorods.

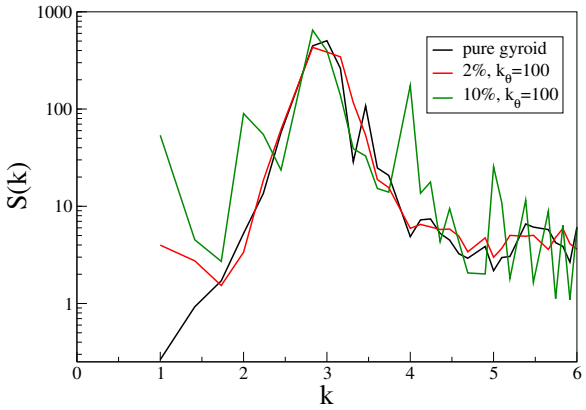

Figure 6.8: Structure factor of pure gyroid, 2% nanorod loading and 10% nanorod loading (a_{AC} = 50, nanorod angle constant k_θ=100) respectively.

6.4 Conclusions

This chapter presents Dissipative particle dynamics simulations performed on model systems of nanorod and diblock copolymer composite to understand the dynamics, structure, and morphology of self-assembled bundles of nanorods in gyroid phase. The nanorods are given preferential enthalpic interaction with minority component B of diblock copolymer by increasing repulsion with majority component C, so that nanorods tend to self-assemble and settle inside the confined contours of minority component B aimimg to explore the relative size and shape of the self-assembled bundles under confining locations within the matrix. The dynamics of self-assembly of nanorods is found to be fast and independent of phase separation of diblock copolymer. We have observed that nanorods self-assemble to form bundles of different sizes and shapes (spherical and elongated) depending upon the relative flexibility of the nanorods and the nanorod-block copolymer interactions. In case of flexible nanorods, both spherical and elongated bundles have been observed to form within matrix. Less flexible nanorods form elongated bundles for all the cases of nanorod-major component repulsive interaction (a_{AC}). The size of the bundles increases from flexible to rigid nanorod. Thus, gyroid phase formed by diblock copolymer can be used as a potential material to prepare *templates* to get nanorod arrays of different size and shapes depending upon the nanorod flexibility and nanorod-copolymer interactions.

References

[1] Li, Z.; Hur, K.; Sai, H.; Higuchi, T.; Takahara, A.; Jinnai, H.; Gruner, S. M.; Wiesner, U. *Nat. Commun.* **2014**, *5*, 1–10.

[2] Liu, D.; Zhong, C. *Macromol. Rapid Comm.* **2006**, *27*, 458–462.

[3] He, L.; Pan, Z.; Zhang, L.; Liang, H. *Soft Matter* **2011**, *7*, 1147–1160.

[4] Balazs, A. C.; Emrick, T.; Russell, T. P. *Science* **2006**, *314*, 1107.

[5] Peng, G.; Qiu, F.; Ginzburg, V. V.; Jasnow, D.; Balazs, A. C. *Science* **2000**, *288*, 1802.

[6] Lopes, W. A.; Jaeger, H. M. *Nature* **2001**, *414*, 735.

[7] Leibler, L. *Macromolecules* **1980**, *13*, 1602.

[8] Bockstaller, M. R.; Thomas, E. L. *Phys. Rev. Lett.* **2004**, *93*, 166106–1.

[9] Lee, J. Y.; Thompson, R.; Jasnow, D.; Balazs, A. C. *Macromolecules* **2002**, *35*, 4855.

[10] Kim, B. J.; Chiu, J. J.; Yi, G. R.; Pine, D. J.; Kramer, E. J. *Adv. Mater.* **2005**, *17*, 2618.

[11] Jin, J. Z.; Wu, J. Z.; Frischknecht, A. L. *Macromolecules* **2009**, *42*, 7537–7544.

[12] Sun, Y. S.; Jeng, U. S.; Liang, K. S.; Yeh, S. W.; Wei, K. H. *Polym.* **2006**, *47*, 1101.

[13] Yeh, S. W.; Wei, K. H.; Sun, Y. S.; Jeng, U. S.; Liang, K. S. *Macromolecules* **2005**, *38*, 6559.

[14] Bockstaller, M. R.; Lapetnikov, Y.; Margel, S.; Thomas, E. L. *J. Am. Chem. Soc.* **2003**, *125*, 5276.

[15] Chiu, J. J.; Kim, B. J.; Kramer, E. J.; Pine, D. J. *J. Am. Chem. Soc.* **2005**, *127*, 5036.

[16] Lee, J. Y.; Thompson, R. B.; Jasnow, D.; Balazs, A. C. *Phys. Rev. Lett.* **2002**, *89*, 155503–1.

[17] Thompson, R. B.; Lee, J. Y.; Jasnow, D.; Balazs, A. C. *Phys. Rev. E* **2002**, *66*, 031801.

[18] Huh, J.; Ginzburg, V. V.; Balazs, A. C. *Macromolecules* **2000**, *33*, 8085.

[19] He, L.; Zhang, L.; Liang, H. *J. Phys. Chem. B* **2008**, *112*, 4194.

[20] Schultz, A. J.; Hall, C. K.; Genzer, J. *Macromolecules* **2005**, *38*, 3007.

[21] Buxton, G. A.; Balazs, A. C. *J. Chem. Phys.* **2002**, *117*, 7649.

[22] Zheng, X.; Forest, M.; Vaia, R.; Arlen, M.; Zhou, R. *Adv. Mater.* **2007**, *19*, 4038–4043.

[23] Zhang, Q. L.; Gupta, S.; Emrick, T.; Russell, T. P. *J. Am. Chem. Soc.* **2006**, *128*, 3898.

[24] Beneut, K.; Constantin, D.; Davidson, P.; Dessombz, A.; Chaneac, C. *Langmuir* **2008**, *24*, 8205.

[25] Ghanbari, A.; Ndoro, T. V. M.; Leroy, F.; Rahimi, M.; Bhm, M. C.; Muller-Plathe, F. *Macromolecules* **2012**, *45*, 572–584.

[26] Maiti, A.; Wescott, J.; Kung, P. *Mol. Simulat.* **2005**, *31*, 143–149.

[27] Chakraborty, S.; Choudhury, C. K.; Roy, S. *Macromolecules* **2013**, *46*, 3631–3638.

[28] Maiti, A.; Wescott, J.; Goldbeck-Wood, G. *Int. J. Nanotechnology* **2005**, *2*, 198–214.

[29] Wang, Y.-C.; Ju, S.-P.; Cheng, H.-Z.; Lu, J.-M.; Wang, H.-H. *J. Phys. Chem. C* **2010**, *114*, 3376–3384.

[30] Wang, Y.-C.; Ju, S.-P.; Huang, T. J.; Wang, H.-H. *Nanoscale Res. Lett.* **2011**, *6*, 433.

[31] Gao, L.; Shillcock, J.; Lipowsky, R. *J. Chem. Phys.* **2007**, *126*, 015101.

[32] Shillcock, J. C.; Lipowsky, R. *J. Chem. Phys.* **2002**, *117*, 5048–5061.

[33] Yamamoto, S.; Maruyama, Y.; Hyodo, S.-a. *J. Chem. Phys.* **2002**, *116*, 5842–5849.

[34] Ortiz, V.; Nielsen, S. O.; Discher, D. E.; Klein, M. L.; Lipowsky, R.; Shillcock, J. *J. Phys. Chem. B* **2005**, *109*, 17708–17714.

[35] Roy, S.; Markova, D.; Kumar, A.; Klapper, M.; Muller-Plathe, F. *Macromolecules* **2009**, *42*, 841–848.

[36] Cui, Y.; Zhong, C.; Xia, J. *Macromol. Rapid Comm.* **2006**, *27*, 1437–1441.

[37] Fraser, B.; Denniston, C.; Muser, M. H. *J. Chem. Phys.* **2006**, *124*, 104902.

[38] Li, X.; Deng, M.; Liu, Y.; Liang, H. *J. Phys. Chem. B* **2008**, *112*, 14762–14765.

[39] Chakraborty, S.; Roy, S. *J. Phys. Chem. B* **2012**, *116*, 3083–3091.

[40] Groot, R. D.; Warren, P. B. *J. Chem. Phys.* **1997**, *107*, 4423–4435.

[41] Seaton, M. A.; Anderson, R. L.; Sebastian, M.; William, S. *Mol. Simulat.* **2013**, *39*, 796–821.

[42] Groot, R. D.; Madden, T. J. *J. Chem. Phys.* **1998**, *108*, 8713–8724.

[43] Veracoechea, F. J. M.; Escobedo, F. A. *J. Chem. Phys.* **2006**, *125*, 104907.

[44] Qian, H.-J.; Chen, L.-J.; Lu, Z.-Y.; Li, Z.-S.; Sun, C.-C. *J. Chem. Phys.* **2006**, *124*, 014903.

[45] Allen, M. P.; Tildesley, D. J. *Computer Simulation of Liquids*, reprint ed.; Oxford science publications; Oxford University Press, USA, 1989.

[46] Hajduk, D. A.; Harper, P. E.; Gruner, S. M. *Macromolecules* **1994**, *27*, 4063.

[47] Lodge, T. P.; Pudll, B.; Hanley, K. J. *Macromolecules* **2002**, *35*, 4707.

[48] Velinova, M.; Sengupta, D.; Tadjer, A. V.; Marrink, S.-J. *Langmuir* **2011**, *27*, 14071.

[49] Theodorou, D. N.; Suter, U. W. *Macromolecules* **1985**, *18*, 1206–1214.

[50] Lee, M.-T.; Vishnyakov, A.; Neimark, A. V. *J. Phys. Chem. B* **2013**, *117*, 10304.

Chapter 7

Summary of the Thesis

The aim of the thesis was to explore structural, dynamical, thermodynamical properties of polymer composites by multiscale computer simulations. Polymer composite systems demand understanding from atomistic to mesoscale level because for such systems, small (atomistic) scale interactions are important as they regulate large scale properties. To do this, molecular dynamics simulations have been used in all atomistic study as well as mesoscale simulations. The information gained from the all atomistic study was translated into the mesoscale simulations by applying necessary mapping procedure. Model systems were also considered to explore structure, dynamics of composites in a confining matrix. The properties were investigated in details in each case so that useful insights about the polymer composite systems can be obtained.

For all atomistic molecular dynamics simulations the necessary force fields for CNT and polycarbonate have been calculated and validated so that outcomes of the study can be compared accurately with realistic systems. Molecular level informations have been explored by studying the

interactions between CNT atoms and different polycarbonate moeties and that has been systematically analyzed and discussed. It was found the nature of the interaction between polycarbonate and CNT is repulsive and this repulsive nature of interaction is responsible for CNTs to make bundles in the matrix. The dynamics of such bundled CNTs is quite slow and locally confined. This also affects the diffusivity of whole composite system which is lower than the neat polymer. This indicates that composite system is mechanically more powerful than neat polycarbonate and higher filler ratio is better for mechanical strength. The mechanism of bundling of CNTs in polycarbonate matrix was elucidated which tells us that nanotubes are prone to form highly ordered structures in aggregations.

Next comes the study of energetics of the bundling of CNTs. The Umbrella Sampling simulation technique has been applied to study free energy calculations of the bundling process. Two types of CNT bundling approaches have been consodered: parallel and perpendicular and the respective free energy changes were computed in monomer and trimer of polycarbonate matrices. It was observed that parallel approach is energetically favorable and bundling tendency is more in trimer matrix than monomer.

Once all atomistic simulations have been performed and details of the interactions have been extracted and understood by thorough analysis our aim was to tranlate those atomistic level informations to mesoscopic level of descriptions of polycarbonate composite. In chapter 5, mesoscale simulation of polycarbonate-CNT composite has been presented. Dissipative Particle Dynamics (DPD) has been performed to explore large scale morphology and dynamics of composite systems. The Flory-Huggins theory was applied for necessary mapping procedure and the interaction parameters for DPD simulation of polycarbonate-CNT composite have been calculated. The long range dynamics of bundles of CNTs was investigated by mean square displacement which indicated the dynamically arrested movement of nanotubes as large percolating morphologies have been formed. This result matches with the experimental findings that CNTs form percolating network when incorporated in polycarbonate matrix over a threshold concentration. In our mesoscale simulation percolation morphology was observed at higher filler loading (10%). The bundling size analysis indicated that with higher loading of CNTs the size of the bundles of CNT increases. With increasing bundle size the dynamics have become more jammed.

Our next study aims to investigate nanofiller morphology and dynamics in highly confined polymer matrix. Block copolymers are excellent agent for providing confinement inherently as they phase separate in different strctures. So DPD simulations were performed on model systems of nanorod and diblock copolymer composite where nanorods are trapped in gyroid phase. The nanorods were given preferential enthalpic interaction with minority component of diblock copolymer by increasing repulsion with majority component, so that nanorods tend to self-assemble and settle inside the confined contours of minority component aimimg to explore the relative size and shape of the self-assembled bundles under confining locations within the matrix. The dynamics of self-assembly of nanorods was found to be fast and independent of phase separation of diblock copolymer. It was observed that nanorods self-assemble to form bundles of different sizes and shapes (spherical and elongated) depending upon the relative flexibility of the nanorods and the nanorod-block copolymer interactions. In case of flexible nanorods, both spherical and elongated bundles have been observed to form within matrix. Less flexible nanorods form elongated bundles for all the cases of nanorod-major component repulsive interaction. The size of the bundles increases from flexible to rigid nanorod. Thus, the essential outcome is that the gyroid phase formed by diblock copolymer can be used as a potential material to prepare *templates* to get nanorod arrays of different size and shapes depending upon the nanorod flexibility and nanorod-copolymer interactions.

Thus multiscale simulation approach to address systems like polymer composites is found to be highly resourceful in terms of understanding structure, dynamics,and energetics of such systems. The crucial insights can be obtained from molecular level interactions and that can be transferred to explain mesoscale phenomena like long scale dynamics, percolation morphology, radius of gyration of nano-assembly, shape anisotropy etc. which can be directly matched and correlated with experimental findings. The same approach can be adopted for other type of polymeric materials taking different industrially important polymers and block copolymers with different type of nanofillers like spherical nanoparticles, nanorods, clays etc. The insight and understanding obtained from multiscale simulations can be helpful for experimentalists to develop strategies for more efficient polymer composites for various useful applications in future.